ADVANCED MANUFACTURING OF SUSTAINABLE MATERIALS

BY

EVAN MICHAEL LLOYD

DISSERTATION

Submitted in partial fulfillment of the requirements
for the degree of Doctor of Philosophy in Chemical Engineering
in the Graduate College of the
University of Illinois at Urbana-Champaign, 2021

Urbana, Illinois

Doctoral Committee:

Professor Charles M. Schroeder, Chair
Professor Jeffrey S. Moore
Professor Nancy R. Sottos
Professor Damien S. Guironnet

ABSTRACT

Since Bakelite and Rayon were first introduced in the early twentieth century, global plastic production has grown to over 300 million metric tons per annum and is expected to double in the next twenty years. Unfortunately, plastics were integrated into our daily lives and virtually every industrial sector without first considering the lifecycle of these materials. Despite their ease of processing, polymeric materials require significant external energy inputs during manufacturing, and subsequently, plastics have an embodied energy that greatly exceeds most material classes. Further, the covalent chemical networks to which plastic materials owe their exceptional performance also prevents their degradation. Polymeric materials are, therefore, accumulating in our landfills and oceans at alarming rates. To prevent further damage to our ecosystem, both the initial manufacture and the end of life of plastic materials must be engineered for sustainability.

We first created a model system capable of cycled polymerization and depolymerization utilizing an engineering thermoplastic with a low ceiling temperature, cyclic poly(phthalaldehyde) (cPPA). cPPA depolymerization proceeded under mild thermal conditions, and quantitative recovery of the monomer was possible. Direct repolymerization of the recovered monomer yielded high quality materials with chemical and mechanical properties equivalent to or greater than the original material. Closed-loop recycling of cPPA was also extended to fiber-reinforced polymer composites. cPPA depolymerization proceeded without damage to the fibers, and both the fiber reinforcements and the composite materials retained 100 % of their mechanical performance through multiple generations.

To improve the performance of cPPA-based materials, we explored the thermal depolymerization mechanism and discovered that single electron transfer (SET) and cleavage of the resulting radical cation served as the primary thermal trigger for cPPA depolymerization. These

findings were extended to other modes of SET triggering, including photoredox catalysis. Incorporation of acridinium salts into cPPA blends yielded photodegradable monolithic solids that rapidly deteriorated in the presence of UV-light. The discovery of an SET triggering mechanism provides a route towards novel environmental triggers including electrochemical oxidation and enzymatic catalysis.

We next sought to address the initial manufacture of polymeric materials, specifically patterned materials. In synthetic systems, patterns are often generated through lengthy multistep processes and access to spatially varying properties is limited. Patterns in natural systems, however, arise through non-deterministic symmetry breaking events. Impressively, natural patterns are replicated throughout species with high fidelity of both function and form. Inspired by natural phenomenon, we leveraged the competition between reaction and thermal transport processes of frontal polymerization to create tunable thermal instabilities and spontaneous breaks from symmetry. The undulations in reaction temperature were harnessed to drive orthogonal chemistries and pattern the morphological, optical, chemical, and mechanical properties of engineering polymers. The complex dynamics of frontal polymerization represent a path towards non-deterministic, developmental manufacturing of synthetic materials.

Finally, the concepts of frontal polymerization and degradable materials were combined by copolymerizing cleavable cyclic olefins during the frontal ring-opening metathesis polymerization (FROMP) of dicyclopentadiene (DCPD). FROMP copolymers possessed material properties that were comparable with native pDCPD, but they were easily degraded into high value fragments by hydrolysis. The degradation fragments, which were rich in hydroxyl functionality, were recycled into polyurethane networks by reaction with commercially available diisocyanates. The recycled materials displayed thermomechanical properties that greatly exceeded those of the original

copolymer, a true embodiment of upcycling. We foresee many opportunities for the energy efficient manufacture of multifunctional materials by frontal copolymerization.

This work is dedicated to the memory of Prof. Scott White. Your passion for science, dedication to your students, and love of life has served as a constant inspiration. I have constantly strived to emulate your example since we first met in February of 2015. You took a chance on me, a kid from a small private university with no experience as an engineer, and gave me endless opportunities. I hope, above all, that I have made you proud and surpassed your expectations for my graduate career. You may be gone, but your memory will live on in the countless lives you have touched and the constant inspiration that you provided to the scientific community.

ACKNOWLEDGMENTS

One thing I learned in graduate school is that your list of acknowledgements is ever increasing. I have so many people that I need to thank for their help along my journey towards a Ph.D., but I would like to start with my advisors: Professors Scott White, Nancy Sottos, and Jeffrey Moore. I cannot thank Professor White enough for welcoming me into the group with truly open arms. From the moment I agreed to join, I became a part of his family. He pushed and inspired me to accomplish things that I would have never dreamed of when I first entered into graduate school. Even though she was not formally my advisor until my third year, Professor Sottos was ever present throughout my Ph.D. She pushed me to always stay focused, always pay attention to the details, and never forget to dream big. As thoroughly as Professor White integrated me into his research family, Professor Sottos took things even farther. She always took an active interest in my personal life, and her true care for her students was always apparent. She pulled our group through some very dark times after Professor White passed and soldiered through her own troubles to make sure we had every bit of support that we needed. She gave me an unprecedented amount of freedom to pursue my passions in the lab, which has truly turned me into the scientist that I am today. She always encouraged my creativity, although she was never a big fan of my "Fire Fridays" where I would try a new experiment late in the afternoon on a Friday, often with terrible outcomes and the occasional small fire. This brings me to the infamous Professor Jeffrey Moore. Every conversation that I had with Jeff throughout my Ph.D. has been more than meaningful. My meetings with him often consisted of a thousand ideas being thrown at me while I furiously jotted them down, or they consisted of a single complex concept that left the wheels spinning for many days and nights. He has taught me to always ask the difficult questions in both science and life and to always break seemingly impossible tasks (yes, the idea of synthetic morphogenesis was

completely ludicrous, and I do not think I will ever forgive you or ever be able to thank you enough for challenging me with it) into digestible pieces. Since the day I joined the lab, Jeff has given me the freedom to explore, fail, and triumph on my own. Despite his *laissez-faire* approach to mentoring, he was always there for a quick conversation or an in-depth meeting whenever I needed it. I am truly thankful for each of my advisors and their support and encouragement on my journey.

I would also like to thank my thesis committee: Professors Charles Schroeder and Damien Guironnet. The very first email that I received from Illinois (aside from the stereotypical application progress updates) was from Charles. It came just two weeks after I had applied to the Chemical and Biomolecular Engineering graduate program, and his offer of acceptance to the program with a Parr fellowship was truly lifechanging. I also had the opportunity to take Charles' Applied Mathematics course, and it is still one of my favorites of graduate school. The homework assignments were brutal, but they challenged me to really master the material. Further, Charles has been an excellent chair for my committee. I took my preliminary exam at a time when Professor White was struggling in his battle with cancer. At the very last minute, Charles found a replacement for Professor White, keeping me from the stress of dealing with the situation. I cannot begin to thank you enough as that was one of the most stressful mornings of my life. During my prelim, Charles pushed me to condense my research efforts and focus on what was truly meaningful. Throughout my Ph.D., Damien has been a champion for my success. He took an active interest in me from the moment I set foot on campus for recruitment. He was also instrumental in navigating the process of pursuing my research interests outside of the department. Finally, Damien allowed me to flourish as an instructor when I served as a teaching assistant for his Polymer Synthesis class. He was more than happy to hand the reigns over to me whenever I wanted to deliver a lecture and provided me with the support and feedback that I needed to continuously improve my skills.

Where do I even begin with the AMS group? I have worked with so many wonderful people that it would take me page after page to thank all of you for help over the last five and a half years. However, I must begin by thanking Hector Lopez Hernandez. Even though we only overlapped for two years, you became one of my best friends. We did practically everything together, spending so much time together that people thought we were together, instead of with our wives. You always reminded me that there were other things outside of the lab and the gym, often ripping me away from my hood at 9 p.m. on a Saturday night. You were also always a sounding board for some of my best and worst ideas. I cannot thank you enough for taking me under your wing and being such an excellent mentor and friend. I would also like to thank Mostafa Yourdkhani for always pushing me to seek more. Even though I did not see it, you knew that I was destined for great things and a career in academia. Thank you for never giving up on me! Next, I would like to thank Elizabeth Feinberg for always being an excellent collaborator and an even better friend. You helped me get through my toughest days in the lab, and we definitely did it in style. Your brilliant ideas, constant support, and friendship were instrumental in the success of our morphogenesis project. You also helped me navigate the process of finding a post doc during the onset of COVID lockdowns and gave me just about the best advice of my Ph.D.: “If everything worked the first time, they would just call it search instead of research”. Next, I would like to thank Jay Sung and Tae Ann Kim for being my night crew buddies in lab 5. No matter what time I was working until, I knew I could count on Jay and Tae Ann for a late-night lab mate. I must also thank Douglas Ivanoff for replacing Jay and Tae Ann on the night crew and the team of engineers doing (or failing at) chemistry. We may not be the best at running columns, but we sure do know how to go through the silica. Doug also joined me as lab manager and graciously took the task of being the mean guy in lab from me. I would also like to thank my longtime collaborator and fellow remodeling teammate Leon Dean

for helping me to get through the insane idea of finding a synthetic mimic for bone remodeling. My thanks also go out to Julian Cooper who has been instrumental in refining my skills as a synthetic chemist during the final year of my Ph.D. Finally, I would like to thank the rest of the AMS group, especially Mayank Garg for embarking on a backpacking trip throughout Europe with me and my computational collaborators Professor Philippe Geubelle, Yuan Gao, and Julie Hemmer for helping me to push the story of synthetic morphogenesis into unprecedented territory.

My thanks also go out to my wonderful group of undergraduate researchers: Edwin Zen, Edgar Mejia, Sydney Butikofer, Haleigh Weszelits, Jason Romero, and Suzanne Peterson. You put up with some of my insane ideas and always tackled them with enthusiasm. You also helped me really hone my skills as a mentor and taught me to always remember that not everyone can tell what I am thinking. Together we were able to accomplish some amazing research, and I cannot thank you enough for your assistance. I truly wish you all the best in your future careers.

I would also like to thank my parents, Mike and Kim, and my sister, Brieann, for their constant love, support, and encouragement. My parents taught me from a very young age to always strive for excellence in everything that I do. They taught me the value of hard work and the importance of family and have been there for me whenever I needed them. I must also thank my mom for the countless pies that she baked for me or the leftovers that she always sent me home with so I would not go hungry. I also give my thanks to Natalie's parents and sister for graciously accepting me into their family when I first started dating Natalie as a freshman at Saint Louis University and treating me like their own son/brother. They have always taken an active interest in my work and cheered me on to do my very best.

Finally, I would like to thank my wonderful wife, Natalie. I have saved the best for last, and she certainly deserves this designation. She has truly been there for me through my good days and

my bad. She has helped me navigate this exceptionally challenging, but rewarding, chapter of my life. She has put up with my long hours, grumpy attitude when things do not go well, and my constant forgetfulness because my mind is buried into designing a new experiment. She has taught me and, at times, forced me to recognize the importance of balance in my life. With this, I have become a much better scientist, a much better husband, and a much better person. Above all, she has loved and supported me unconditionally.

Table of Contents

Chapter 1: Introduction

1.1 Shortcomings of Synthetic Materials

Prior to the widespread use of commodity plastics, everyday essentials were made from natural products such as ivory and tortoiseshell. In the mid 1800s, annual demand for ivory reached over two million pounds, the equivalent of over 40,000 elephant tusks.[1,2] To reduce reliance on ivory, a New York firm put out a prize for $10,000 to anyone that created a suitable substitute.[1] Soon after the call by the firm, John Wesley Hyatt introduced Celluloid, a mixture of cellulose nitrate and camphor which was easily molded into a variety of shapes.[1] By 1870, celluloid began to replace tortoiseshell and ivory in products like toothbrushes, knife handles, and combs. Ironically, the product that formed the foundation of the plastics revolution was believed to be the savior of the tortoise.[1]

The light weight, low cost, chemical and mechanical resilience, and wide range of accessible mechanical properties of plastic materials has contributed to their global proliferation. Plastics are the preferred choice of material for most consumer products, especially for the food and beverage sector. Their excellent barrier properties have improved the health and safety of consumers and reduced food waste[3] by significantly extending the lifetimes of packaged products[4]. Further, the light weight and mechanical performance of fiber-reinforced polymer composites (FRPCs) have ensured widespread adoption of polymeric materials in the energy and transportation sectors. Developments in FRPC technologies have significantly increased the attainable wind turbine blade lengths and improved wind energy production. Early wind turbine designs, which utilized metal blades, were limited to outputs of approximately 200 kilowatts[5]. Modern wind turbines, which utilize FRPCs blades, are now capable of generating over 2 megawatts[6], a two order of magnitude increase in power output. Further, the high specific strength and stiffness of FRPCs has led to

dramatic reductions in the necessary weight of structural materials in vehicles and aircraft, greatly improving fuel efficiency and CO_2 emissions.[7] As a result, the transportation industry is drastically increasing the amount of FRPCs being utilized. The Boeing 787 Dreamliner, for example, contains 80 % composites by volume.[8] With the countless applications for polymeric materials, global production has reached over 300 million metric tons per year and is estimated to double within the next twenty years[4]. By 2050, plastic production is expected to account for twenty percent of the global oil consumption[4,9] and fifteen percent of annual carbon emissions[4].

Mechanical performance, thermal and chemical stability, and a long lifetime are all achieved through the high-strength covalent networks of polymeric materials. However, these covalent networks are exceptionally challenging to break down or recycle – often requiring temperatures in excess of 400 °C, supercritical fluids, or concentrated acids[10–12] – when a material reaches the end of its useful lifespan. Coupled with collection costs, lack of infrastructure, and poor demand for recycled goods, the steep energetic barriers to material degradation make recycling end-of-life materials impractical.[4,9,13] Consequently, more than 100 million metric tons of plastic waste are disposed of in landfills or dumped illegally each year[9,13], creating significant economic losses (projected at $200 billion in raw materials annually[13]) and grave environmental concerns.

Plastics constitute approximately ten percent of the municipal solid waste stream, but, due to their low density, they occupy a disproportionate amount of space in landfills.[9] This conundrum is particularly prevalent as we have reached the 30 year life span of FRPC wind turbine blades that were introduced into large scale solar farms across the states in the 1980s and 1990s. The sheer size of these structures, which often exceed 25 m in length and are increasing in size with technological developments, is overwhelming municipal landfills. A landfill in Casper, Wyoming could only accommodate 870 turbine blades this year, a fraction of the thousands that are being

decommissioned annually.[14] The challenges of disposing large-scale structures will be compounded in the future by the pervasive use of FRPCs in civil infrastructure[15], vehicles[16], and aircraft[7,8].

Due to the durability and light weight of plastics, two features for which they are highly prized, plastic waste often infiltrates marine environments. A staggering 5.25 trillion plastic pieces[17] weighing approximately 275 million metric tons[18] are floating in the world's oceans. The MacArthur foundation predicts that the amount of plastic afloat at sea will outweigh the fish in the ocean by 2050.[19] The macro- and micro-plastics floating in oceans pose both immediate and long-term hazards to aquatic and terrestrial life.[20] Animals often become entangled in larger plastic pieces, while smaller plastic pieces are mistaken for food.[9] Ingestion can cause tears and blockages in the gastrointestinal tract, leading to loss of appetite, severe weight loss, and sometimes death. While the immediate dangers of plastic waste to aquatic life (choking, entanglement, etc.) are apparent, the long-term effects remain unknown to the general public. Plastics are typically viewed as chemically inert, but they contain residual monomers, plasticizers, fire retardants, and a host of other additives, many of which are known endocrine disruptors[21]. Several studies have shown that the microplastics ingested by aquatic life can be transferred to higher trophic levels[22], along with the small molecule additives within the plastics, a grave concern for both marine and terrestrial life.

The issues with polymeric materials are not limited to their disposal or recycling. Their initial manufacture is exceptionally energy intensive and also presents a significant environmental challenge. Both thermoplastic and thermoset polymers are processed at high temperature and often under high external pressure. Thermoplastics are melt processed into their final morphology via injection or compression molding, thermoforming, or extrusion, consuming an estimated 10^5

Joules per kilogram of polymer.[23] Thermosets, which do not display melt transitions, must be cured from a reactive resin into the final crosslinked polymer. Cure cycles can take several hours and require ovens or heated molds operated in excess of 150 °C, consuming between 10^6 and 10^8 Joules per kilogram of polymer produced.[24,25] Between the energy for feedstock preparation and processing energy, polymeric materials are estimated to have an embodied energy of 60 to 100 megajoules per kilogram, which is substantially higher than paper, wood, glass, and most metals[4]. In either case, the energetic requirements and the size of the needed equipment scales with the size of the desired part.[7,23] This caveat is especially problematic as the number of large scale, polymeric structures employed in civil infrastructure and the energy and transportation sectors is steadily increasing[7,8,15,16]. For example, the autoclave utilized to cure the FRPC in a section of the Boeing 787 fuselage reaches over 9 meters in diameter and 30 meters in length. This massive piece of equipment consumes over 350 gigajoules of energy and produces over 80 tons of carbon dioxide during a single cure cycle[7], the energetic equivalent of powering nine American households[26] and the emissions equivalent of operating sixteen passenger vehicles[27] for an entire year.

The impact of the plastics industry will be felt by generation after generation and will forever be recorded in geologic history. In 2016, the International Commission of Stratigraphy searched for an event which would mark the end of the *Holocene* Epoch and the beginning of the *Anthropocene* Epoch.[9] One of their primary candidates was the global proliferation of polymeric materials following the Second World War.[28] Other candidates were increases in greenhouse gas emissions from fossil fuels and spikes in radiocarbon levels from atomic bomb tests[28]. To bring an end to this global crisis and provide a brighter future for our children and grandchildren, we must design the next generation of polymeric materials sustainably. They must be manufactured with minimal external energy inputs and incorporate end-of-life strategies. The present work achieves

a sustainable materials design by employing two systems: transient polymers and frontal polymerization.

1.2 Transient Polymers

Transient polymers are those capable of disintegrating on demand following the application of a designed stimulus.[29] Stimuli are typically mild in nature and, ideally, orthogonal to the conditions of the intended material application. The concept of triggered degradation is not new, but the recent surge in interest in stimuli-responsive materials has contributed to a myriad of novel polymer designs[29–35]. Each of these designs differ in mechanical performance, rates of degradations, and, of particular importance, the degradation products. In most cases, degradation products differ from the starting materials of the polymer, making synthesis of the original material challenging. However, one class of materials, low ceiling temperature polymers, reverts selectively to the monomeric components upon triggering.[33] This key feature enables closed-loop utilization of resources.

The ceiling temperature phenomenon was first reported in 1943 when Snow and Frey observed that the copolymerization of sulfur dioxide and olefins could be stopped or started at will by simply raising or lowering the temperature just a few degrees, respectively.[36] They attributed the ceiling temperature effect to the formation of a short-lived inhibitor at higher reaction temperatures. Five years later, Dainton and Ivin correctly assigned this puzzling temperature dependence to polymer thermodynamics.[37] Based on the work of Mesrobian and Tobolsky[38], Dainton and Ivin suggested that polymerizations have both a forward and a reverse reaction. Coupled with the fact that, in almost all cases, polymerization reactions proceed with a release of heat ($\Delta H < 0$) and a decrease in entropy ($\Delta S < 0$), they concluded that there must be a temperature, the ceiling temperature, where thermodynamic equilibrium is reached and propagation is halted. Below the ceiling

temperature, the forward reaction is favored, and propagation continues. However, if the temperature exceeds the ceiling temperature, the reverse reaction is favored, and the polymer chain unzips.[33]

It is important to note that the ceiling temperature phenomenon was not encountered until the 1940s[33], despite several decades of polymer research. Most olefin polymerization reactions are highly exothermic, yielding 10 – 20 kcal mol^{-1},[37] and the enthalpic release heavily outweighs entropic losses. Subsequently, poly(olefin)s typically have extremely high ceiling temperatures (> 300 °C) and experience degradation prior to reaching their ceiling temperature.[33] The reduced enthalpy of olefin and sulfur dioxide copolymerizations[36,37] significantly reduced the ceiling temperature of poly(olefin sulfone)s and enabled researchers to observe depolymerization at elevated temperatures rather than polymer degradation. This fundamental finding formed the foundation of low ceiling temperature polymer research.

As their name suggests, low ceiling temperature (T_c) polymers are thermodynamically unstable and readily depolymerize near ambient temperature, limiting their application in materials research. However, by trapping the growing polymer chain in a local energy minimum, these polymers can be isolated well above their ceiling temperatures as metastable polymers. Capping of the polymer chain end below the ceiling temperature provides a sufficient energy barrier to prevent unwanted depolymerization above T_c. A number of "capping" strategies have been developed, including intramolecular cyclization[39], copolymerization with monomers that yield high T_c blocks[40], and the introduction of a stable end cap[41]. Cleavage of either the end cap or the low T_c polymer backbone reveals reactive chain ends which are capable of depolymerization. Depending on the introduced end cap or the nature of the polymer backbone, low T_c polymers can be tuned to be sensitive to a variety of environmental stimuli. Low T_c polymers have, therefore,

become wildly popular as stimuli-responsive materials. Applications such as lithography[42], signal amplification[43,44], triggered release[45,46], and transient electronics[47,48] have all been explored with low T_c polymers. Importantly, the clean depolymerization of low T_c polymers has been exploited for facile recycling of polymeric materials[49–52], which will be discussed further in chapter 2.

1.3 Frontal Polymerization

Frontal polymerization (FP) is a curing strategy that harnesses latent chemical energy stored within the monomer to drive materials synthesis. Similar to combustion, a small energetic input initiates a cascade of chemical reactions which rapidly transforms the starting materials into the final product. During combustion, a small spark ignites the fuel (gasoline, wood, etc.), and the chemical potential of the fuel is released as light and heat as the fuel burns. The heat released in one region ignites the fuel in another region, and the flames propagate until all of the fuel is consumed or the fire is extinguished. During frontal polymerization, a local stimulus activates a thermally latent initiator that mediates the conversion of monomer to polymer, releasing the latent chemical energy stored within the monomer.[53] Transport of the released heat activates initiator in neighboring locations and drives the propagating wave of polymerization. The autocatalysis present in both combustion and FP translates localized stimuli into global changes.[54] Where a fire destroys the fuel, FP transforms its monomeric fuel into structural polymeric networks.

FP has been employed in polymer synthesis for almost 50 years. Chechilo and coworkers made the first report on FP when they studied the frontal free radical polymerization of methyl acrylate with a benzoyl peroxide (BPO) initiator in a high-pressure reactor in 1972.[55] Since the initial introduction of FP, a large body of literature with more than 300 publications has amassed. The library of FP resin systems has grown to include a variety of acrylates[55–61], epoxies[62–66], and cyclic olefins[67–70], and front velocities of up to 30 cm min^{-1} have been reported[59].

To be employed sensibly in materials manufacturing, FP systems must meet several criteria. The FP chemistry must possess sufficient energy density to sustain fronts in the presence of various boundary conditions and high loadings of inactive fillers such as fiber reinforcements. Second, the FP resin must have sufficient latency to permit materials preparation and handling (e.g. infusion of fabric with resin during composite preparation) with minimal background polymerization at room temperature. Finally, the resultant mechanical properties must be suitable for the intended application.

Acrylates, which have been featured in a significant portion of FP literature, possess exceptionally high energy densities. Enthalpies of polymerization in excess of 40 kcal mol^{-1} have been reported.[71] Additionally, the high activation barriers for the cleavage of the O–O or C–N bond in a radical initiator (approximately 35 kcal mol^{-1})[72] limits any background polymerization at room temperature and provides for very long pot lives. Unfortunately, the energy density of acrylate resins can generate excessively high front temperatures (> 300 °C)[73], leading to deleterious effects such as void formation or charring in the final products. Further, the mechanical performance of poly(acrylate)s are typically insufficient for structural applications[74]. Epoxy based systems, on the other hand, yield high performance materials. However, the low energy density of the epoxide structure[63,64] and the activity of the amine hardener at room temperature[64], limit both the achievable front velocities and pot lives.

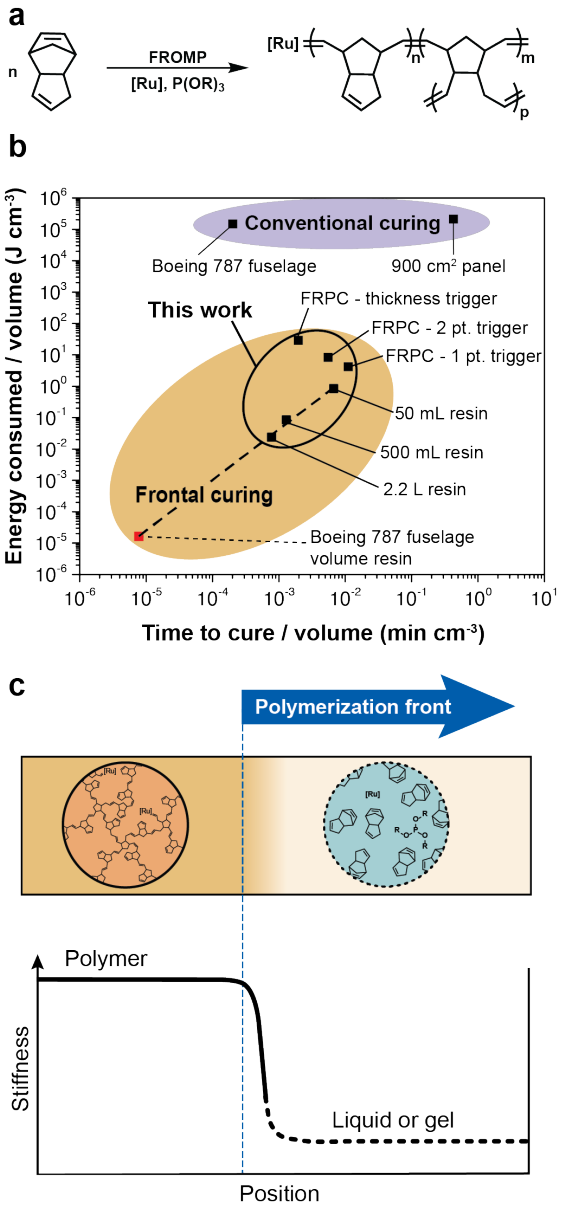

Figure 1.1. Overview of the frontal-polymerization concept | a, Scheme for the frontal ring-opening metathesis polymerization (FROMP) of dicyclopentadiene (DCPD) using a ruthenium catalyst (Ru) and an alkyl phosphite inhibitor ($P(OR)_3$). b, Comparison of the energy required for curing versus the time taken for curing via frontal polymerization and conventional curing. We calculated that the curing of a section of the Boeing 787 fuselage by FROMP (red square) reduces the energy consumption by ten orders of magnitude compared with conventional techniques. c, In the technique used here, the FROMP solution is triggered to polymerize in its liquid state rapidly transforming the liquid into a durable thermoset polymer. Adapted from Robertson et al.[74]

Strained cyclic olefins which readily undergo ring-opening metathesis polymerization are known to generate thermoplastics[75] and thermosets[76] with robust mechanical, thermal, and chemical properties. FP of these systems, especially the frontal ring-opening metathesis

polymerization (FROMP) of dicyclopentadiene (DCPD), have been shown to support frontal velocities greater than 10 cm min^{-1}, but with more modest front temperatures (ca. 200 °C) than acrylate systems.[77] However, the high catalytic activity of the ruthenium catalysts employed in FROMP of DCPD led to extremely short pot lives, on the order of several minutes.[68,77] In 2017, Robertson and coworkers introduced alkyl phosphite inhibitors into FROMP resins and realized unprecedented pot lives of up to 30 hours.[78] This fundamental contribution to the FP community enabled the fabrication of high performance composite materials by frontal polymerization (**Figure 1.1**).[74] Importantly, well-controlled FP offers substantial savings in manufacturing energy, a reduction of up ten orders of magnitude, and effectively eliminates the need for costly infrastructure.

1.4 Summary

Both low ceiling temperature polymers and frontal polymerization show great potential in improving the sustainability of polymeric materials. The majority of low T_c polymer investigations has highlighted triggered transience, but little emphasis has been placed on recycling. The mild depolymerization triggers and clean unzipping to monomer are two features that remain underexploited. They also represent a potential solution to the harsh conditions associated with composite recycling, which is the focus of chapter 2. Further, while FP addresses the energetics of manufacturing, disposal of end-of-life materials remains an issue. Incorporation of cleavable units into FROMP resins, the topic of chapter 4, enables triggered transience while retaining the manufacturing benefits of FP. Finally, the surplus of heat generated during FP has not been utilized to drive additional chemical or physical transformations. We envision this wasted resource as a route to multifunctional materials. Chapters 5 and 6 will center on exploiting the surplus of heat to

autonomously pattern materials. We are in the midst of a global crisis, but with careful design, the next generation of materials will contribute to a more sustainable future.

1.5 References

1. Seymour, R. B.; Kauffman, G. B. The Rise and Fall of Celluloid. *J. Chem. Educ.* **1992**, 69, 311-314.
2. Basson, M.; Beddington, J. R.; May, R. M. An Assessment of the Maximum Sustainable Yield of Ivory from African Elephant Populations. *Math. Biosci.***1991**, 104, 73-95.
3. Andrady, A. L.; Neal, M. A. Applications and Societal Benefits of Plastics. *Philos. Trans. R. Soc., B* **2009**, 364, 1977-1984.
4. Lebreton, L.; Andrady, A. Future Scenarios of Global Plastic Waste Generation and Disposal. *Palgrave Commun.* **2019**, 5, 6.
5. Mishnaevsky, L. Branner, K.; Peterson, H. N.; Beauson, J.; McGugan, M.; Sørensen, B. F. Materials for Wind Turbine Blades: An Overview. *Materials* **2017**, 10, 1285.
6. Brønsted, P.; Lilholt, H.; Lystrup, A. Composite Materials for Wind Power Turbine Blades. *Annu. Rev. Mater. Res.* **2005**, 35, 505-538.
7. Timmis, A. J.; Hodzic, A.; Koh, L.; Bonner, M.; Soutis, C.; Schäfer, A. W.; Dray, L. Environmental Impact Assessment of Aviation Emission Reduction through the Implementation of Composite Materials. *Int. J. Life Cycle Assess.* **2014**, 20, 233-243.
8. Giurgiutiu, V. *Structural Health Monitoring of Aerospace Composites*; Academic Press: London, UK, 2016.
9. Schneiderman, D. K.; Hillmyer, M. A. 50th Anniversary Perspective: There Is a Great Future in Sustainable Polymers. *Macromolecules* **2017**, 50, 3733-3749.
10. Pickering, S. J. Recycling Technologies for Thermoset Composite Materials – Current Status. *Composites, Part A* **2006**, 37, 1206-1215.
11. Al-Salem, S. M.; Lettieri, P.; Baeyens, J. Recycling and Recovery Route of Plastic Solid Waste (PSW): A Review. *Waste Manage.* **2009**, 29, 2625-2643.
12. George, N.; Kurian, T. Recent Developments in the Chemical Recycling of Postconsumer Poly(ethylene terephthalate) Waste. *Ind. Eng. Chem. Res.* **2014**, 53, 14185-14198.
13. Garcia, J. M.; Robertson, M. L. The Future of Plastics Recycling. *Science* **2017**, 358, 870–872.
14. Martin, C. Wind Turbine Blades Can't Be Recycled, So They're Piling Up in Landfills; 2020; Retrieved from: https://www.bloomberg.com/news.
15. Karbhari, V. M.; Seible, F. Fiber Reinforced Composites – Advanced Materials for the Renewal of Civil Infrastructure. *Appl. Compos. Mater.* **2000**, 7, 95-124.
16. Friedrich, K.; Almajid, A. A. Manufacturing Aspects of Advanced Polymer Composites for Automotive Applications. *Appl. Compos. Mater.* **2013**, 20, 107-128.
17. Eriksen, M.; Lebreton, L. C. M.; Carson, H. S.; Thiel, M.; Moore, C. J. Borerro, J. C.; Galgani, F.; Ryan, P. G.; Reisser, J. Plastic Pollution in the World's Oceans: More than 5 Trillion Plastic Pieces Weighing over 250,000 Tons Afloat at Sea. *PLoS One* **2014**, 9, e111913.
18. Jambeck, J. R.; Geyer, R.; Wilcox, C.; Siegler, T. R.; Perryman, M.; Andrady, A.; Narayan, R.; Law, K. L. Plastic Waste Inputs from Land into the Ocean. *Science* **2015**, 347, 768-771.
19. World Economic Forum, Ellen MacArthur Foundation and McKinsey Company, The New Plastics Economy Rethinking the Future of Plastics; 2016; Retrieved from: https://www.ellenmacarthurfoundation.org/publications.
20. Haward, M. Plastic Pollution of the World's Seas and Oceans as a Contemporary Challenge in Ocean Governance. *Nat. Commun.* **2018**, 9, 667.
21. Meeker, J. D.; Sathyanarayana, S.; Swan, S. H. Phthalates and Other Additives in Plastics: Human Exposure and Associated Health Outcomes. *Philos. Trans. R. Soc. B* **2009**, 364, 2097-2113.
22. Farrell, P.; Nelson, K. Trophic Level Transfer of Microplastic: *Mytilus Edulis* (L.) to *Carcinus Maenas* (L.). *Environ. Pollut.* **2013**, 177, 1-3.
23. Abeykoon, C.; Kelly, A. L.; Brown, E. C.; Vera-Sorroche, J.; Coates, P. D.; Harkin-Jones, E.; Howell, K. B.; Deng, J.; Li, K.; Price, M. Investigation of the Process Energy Demand in Polymer Extrusion: A Brief Review and an Experimental Study. *Appl. Energ.* **2014**, 136, 726-737.
24. Abliz, D.; Duan, Y.; Steuernagel, L.; Xie, L.; Li, D.; Ziegmann, G. Curing Methods for Advanced Polymer Composites – A Review. *Polym. Polym. Compos.* **2013**, 21, 341-348.

25. Boluk, M. Y.; Aktik, M.; Bilgen, E. Energy Requirements and Cost in Polymer Curing Processes. *Energy* **1990**, 15, 811-820.
26. U.S. Energy Information Administration, How Much Energy Does and American Home Use?; 2020; Retrieved from: https://www.eia.gov/tools/faqs.
27. United States Environmental Protection Agency, Greenhouse Gas Emissions from a Typical Passenger Vehicle; 2018; Retrieved from: https://www.epa.gov/greenvehicles.
28. Zalasiewicz, J.; Waters, C. N.; Ivar do Sul J. A.; Corcoran, P. L.; Barnosky, A. D.; Cearreta, A.; Edgeworth, M.; Galuszka, A.; Jeandel, C.; Leinfelder, R.; McNeill, J. R.; Steffen, W.; Summerhayes, C.; Wagreich, M.; Williams, M.; Wolfe, A. P.; Yonan, Y. The Geological Cycle of Plastics and Their Use as a Stratigraphic Indicator of the Anthropocene. *Anthropocene* **2016**, 13, 4-17.
29. Fu, J.; Wang, Z.; Dai, J.; Carter, M.; Hu, L. Transient Electronics: Materials and Devices. *Chem. Mater.* **2016**, 28, 3527-3539.
30. Peterson, G. I.; Larsen, M. B.; Boydston, A. J. Controlled Depolymerization: Stimuli-Responsive Self-Immolative Polymers. *Macromolecules* **2012**, 45, 7317-7328.
31. Sagi, A.; Weinstain, R.; Karton, N.; Shabat, D. Self-Immolative Polymers. *J. Am. Chem. Soc.* **2008**, 130, 5434-5435.
32. Yardley, R. E.; Kenaree, A. R.; Gillies, E. R. Triggering Depolymerization: Progress and Opportunities for Self-Immolative Polymers. *Macromolecules* **2019**, 52, 6342-6360.
33. Kaitz, J. A.; Lee, O. P.; Moore, J. S. Depolymerizable Polymers: Preparation, Applications, and Future Outlook. *MRS Commun.* **2015**, 5, 191-204.
34. Shieh, P.; Zhang, W.; Husted, K. E. L.; Kristufek, S. L.; Xiong, B.; Lundberg, D. J.; Lem, J.; Veysset, D.; Sun, Y.; Nelson, K. A.; Plata, D. L.; Johnson, J. A. Cleavable Comonomers Enable Degradable, Recyclable Thermoset Plastics. *Nature* **2020**, 583, 542-547.
35. Hong, M.; Chen, E. Y.-X. Completely Recyclable Biopolymers with Linear and Cyclic Topologies via Ring-Opening Polymerization of γ-Butyrolactone. *Nat. Chem.* **2016**, 8, 42-49.
36. Snow, R. D.; Frey, F. E. The Reaction of Sulfur Dioxide with Olefins: The Ceiling Temperature Phenomenon. *J. Am. Chem. Soc.* **1943**, 65, 2417-2418.
37. Dainton, F. S.; Ivin, K. J. Reversibility of the Propagation Reaction in Polymerizations Processes and Its Manifestation in the Phenomenon of a 'Ceiling Temperature'. *Nature* **1948**, 162, 705-707.
38. Mesrobian, R.; Tobolsky, A. Simultaneous Polymerization and Degradation in Polymer Systems: Styrene in Toluene Solution. *J. Am. Chem. Soc.* **1945**, 67, 785-787.
39. Kaitz, J. A.; Diesendruck, C. E.; Moore, J. S. End Group Characterization of Poly(phthalaldehyde): Surprising Discovery of a Reversible, Cationic Macrocyclization Mechanism. *J. Am. Chem. Soc.* **2013**, 135, 12755-12761.
40. Masamoto, J. Modern Polyacetals. *Prog. Polym. Sci.* **1993**, 18, 1-84.
41. Schweitzer, C. E.; Macdonald, R. N.; Punderson, J. O. Thermally Stable High Molecular Weight Polyoxymethylenes. *J. Appl. Polym. Sci.* **1959**, 1, 158-163.
42. Bowden, M. J.; Thompson, L. F. Electron Irradiation of Poly(Olefin Sulfones). Application to Electron Beam Resists. *J. Appl. Polym. Sci.* **1973**, 17, 3211-3221.
43. Lewis, G. G.; Robbins, J. S.; Phillips, S. T. Phase-Switching Depolymerizable Poly(carbamate) Oligomers for Signal Amplification in Quantitative Time-Based Assays. *Macromolecules* **2013**, 46, 5177-5183.
44. Phillips, S. T.; Robbins, J. S.; DiLauro, A. M.; Olah, M. G. Amplified Responses in Materials Using Linear Polymers That Depolymerize from End-to-End When Exposed to Specific Stimuli. *J. Appl. Polym. Sci.* **2014**, 131, 40992-41004.
45. Esser-Kahn, A. P.; Odom, S. A.; Sottos, N. R.; White, S. R.; Moore, J. S. Triggered Release from Polymer Capsules. *Macromolecules* **2011**, 44, 5539-5553.
46. Tang, S.; Yourdkhani, M.; Casey, C. M. P.; Sottos, N. R.; White, S. R.; Moore, J. S. Low Ceiling Temperature Polymer Microcapsules with Hydrophobic Payloads via Rapid Emulsion-Solvent Evaporation. *ACS Appl. Mater. Inter.* **2017**, 9, 20115-20123.
47. Lopez Hernandez, H.; Kang, S.-K.; Lee, O. P.; Hwang, S.-W.; Kaitz, J. A.; Inci, B.; Park, C. W.; Chung, S.; Sottos, N. R.; Moore, J. S.; Rogers, J. A.; White, S. R. Triggered Transience of Metastable Poly(phthalaldehyde) for Transient Electronics. *Adv. Mater.* **2014**, 26, 7637-7642.
48. Park, C. W.; Kang, S.-K.; Lopez Hernandez, H.; Kaitz, J. A.; Wie, D. S.; Shin, J.; Lee, O. P.; Sottos, N. R.; Moore, J. S.; Rogers, J. A.; White, S. R. Thermally Triggered Degradation of Transient Electronic Devices. *Adv. Mater.* **2015**, 27, 3783-3788.

49. Diesendruck, C. E.; Peterson, G. I.; Kulik, H. J.; Kaitz, J. A.; Mar, B. D.; May, P. A.; White, S. R.; Martínez, T. J.; Boydston, A. J.; Moore, J. S. Mechanically Triggered Heterolytic Unzipping of a Low-Ceiling-Temperature Polymer. *Nat. Chem.* **2014**, 6, 623-628.
50. Baker, M. S.; Kim, H.; Olah, M. G.; Lewis, G. G.; Phillips, S. T. Depolymerizable Poly(benzyl ether)-Based Materials for Selective Room Temperature Recycling. *Green Chem.* **2015**, 17, 4541-4545.
51. Fan, B.; Trant, J. F.; Yardley, R. E.; Pickering, A. J.; Lagugné-Labarthet, F.; Gillies, E. R. Photocontrolled Degradation of Stimuli-Responsive Poly(ethyl glyoxylate): Differentiating Features and Traceless Ambient Depolymerization. *Macromolecules* **2016**, 49, 7196-7203.
52. Lloyd, E. M.; Lopez Hernandez, H.; Feinberg, E. C.; Yourdkhani, M.; Zen, E. K.; Mejia, E. B.; Sottos, N. R.; Moore, J. S.; White, S. R. Fully Recyclable Metastable Polymers and Composites. *Chem. Mater.* **2018**, 31, 398-406.
53. Pojman, J. A. in *Polymer Science: A Comprehensive Reference* Vol. 4 (eds. Matyjaszewski, K. & Möller, M.) Elsevier: Amsterdam, 2012; pp. 957-980.
54. Bissette, A. J.; Fletcher, S. P. Mechanisms of Autocatalysis. *Angew. Chem., Int. Ed.* **2013**, 52, 12800.
55. Chechilo, N. M. Khvilivitsky, R. Y.; Enikolopyan, N. S. On the Phenomenon of Polymerization Reaction Spreading. *Dokl. Akad. Nauk SSSR* **1972**, 204, 1180-1181.
56. Pojman, J. A. Traveling Fronts of Methacrylic Acid Polymerization. *J. Am. Chem. Soc.* **1991**, 113, 6284-6286.
57. Nason, C.; Roper, T.; Hoyle, C.; Pojman, J. A. UV-Induced Frontal Polymerization of Multifunctional (Meth)Acrylates. *Macromolecules* **2005**, 38, 5506-5512.
58. Masere, J.; Stewart, F.; Meehan, T.; Pojman, J. A. Period-Doubling Behavior in Frontal Polymerization of Multifunctional Acrylates. *Chaos* **1999**, 9, 315-322.
59. Mariani, A.; Fiori, S.; Bidali, S.; Alzari, V.; Malucelli, G. Frontal Polymerization of Diurethane Diacrylates. *J. Polym. Sci., Part A: Polym. Chem.* **2008**, 46, 3344-3352.
60. Morales, A.; Pojman, J. A. A Study of the Effects of Thiols on the Frontal Polymerization and Pot Life of Multifunctional Acrylate Systems with Cumene Hydroperoxide. *J. Polym. Sci., Part A: Polym. Chem.* **2013**, 51, 3850-3855.
61. Holt, J.; Fazende, K.; Jee, E.; Wu. Q.; Pojman, J. A. Cure-on-Demand Wood Adhesive Based on the Frontal Polymerization of Acrylates. *J. Appl. Polym. Sci.* **2016**, 133, 44064.
62. Arutiunian, K. A.; Davtyan, S. P.; Rozenberg, B. A.; Enikolopyan, N. S. Curing of Epoxy Resins of Bis-Phenol A by Amines under Conditions of Reaction Front Propagation. *Dokl. Akad. Nauk SSSR* **195**, 223, 657-660.
63. White, S. R.; Kim, C. A. Simultaneous Lay-Up and in situ Cure Process for Thick Composites. *J. Reinf. Plast. Comp.* **1993**, 12, 520-535.
64. Chekanov, Y.; Arrington, D.; Brust, G.; Pojman, J. A. Frontal Curing of Epoxy Resins: Comparison of Mechanical and Thermal Properties to Batch-Cured Materials. *J. Appl. Polym. Sci.* **1997**, 66, 1209-1216.
65. Chen, S.; Tian, Y.; Chen, L.; Hu, T. Epoxy Resin/Polyurethane Hybrid Networks Synthesized by Frontal Polymerization. *Chem. Mater.* **2006**, 18, 2159-2163.
66. Scognamillo, S.; Bounds, C.; Luger, M.; Mariani, A.; Pojman, J. A. Frontal Cationic Curing of Epoxy Resins. *J. Polym. Sci., Part A: Polym. Chem.* **2010**, 48, 2000-2005.
67. Mariani, A. Fiori, S.; Chekanov, Y.; Pojman, J. A. Frontal Ring-Opening Metathesis Polymerization of Dicyclopentadiene. *Macromolecules* **2001**, 34, 6539-6541.
68. Robertson, I. D.; Pruitt, E. L.; Moore, J. S. Frontal Ring-Opening Metathesis Polymerization of Exo-Dicyclopentadiene for Low Catalyst Loadings. *ACS Macro Lett.* **2016**, 5, 593-596.
69. Dean, L. M.; Wu, Q.; Alshangiti, O.; Moore, J. S.; Sottos, N. R. Rapid Synthesis of Elastomers and Thermosets with Tunable Thermomechanical Properties. *ACS Macro Lett.* **2020**, 819-824.
70. Ivanoff, D. G.; Sung, J.; Butikofer, S. M.; Moore, J. S.; Sottos, N. R.; Cross-Linking Agents for Enhanced Performance of Thermosets Prepared via Frontal Ring-Opening Metathesis Polymerization. *Macromolecules* **2020**, 53, 8360-8366.
71. Lee, H.; Colby, C. Heat of Polymerization of Nine Mono-, Di-, and Trimethacrylate Esters Tested Neat and with Low Levels of Peroxide by Dynamic Differential Scanning Calorimetry. *Dent. Mater.* **1986**, 2, 175-178.
72. Iizuka, Y.; Surianarayanan, M. Comprehensive Kinetic Model for Adiabatic Decomposition of Di-*tert*-Butyl Peroxide Using BatchCad. *Ind. Eng. Chem. Res.* **2003**, 42, 2987-2995.
73. Robertson, I. D.; Lopez Hernandez, H.; White, S. R.; Moore, J. S. Rapid Stiffening of a Microfluidic Endoskeleton via Frontal Polymerization. *ACS Appl. Mater. Inter.* **2014**, 6, 18469-18474.
74. Robertson, I. D.; Yourdkhani, M.; Centellas, P. J.; Aw, J. E.; Ivanoff, D. G.; Goli, E.; Lloyd, E. M.; Dean, L. M.; Sottos, N. R.; Geubelle, P. H.; Moore, J. S.; White, S. R. Rapid Energy-Efficient Manufacturing of Polymers and Composites via Frontal Polymerization. *Nature* **2018**, 557, 223-227.

75. Galperin, I.; Carter, J. H.; Hein, P. R. Poly(norbornene): Tensile and Dynamic-Mechanical Properties. *J. Appl. Polym. Sci.* **1968**, 12, 1751-1754.
76. Vallons, K. A. M.; Drozdzak, R.; Charret, M.; Lomov, S. V.; Verpoest, I. Assessment of the Mechanical Behaviour of Glass Fibre Composites with a Tough Polydicyclopentadiene (PDCPD) Matrix. *Composites, Part A* **2015**, 78, 191-200.
77. Fuiu, A.; Sanna, D.; Alzari, V.; Nuvoli, D.; Mariani, A. Advances in the Frontal Ring Opening Metathesis Polymerization of Dicyclopentadiene. *J. Polym. Sci., Part A: Polym. Chem.* **2014**, 52, 2776-2780.
78. Robertson, I. D.; Dean, L. M.; Rudebusch, G. E.; Sottos, N. R.; White, S. R.; Moore, J. S. Alkyl Phosphite Inhibitors for Frontal Ring-Opening Metathesis Polymerization Greatly Increase Pot Life. *ACS Macro Lett.* **2017**, 6, 609-612.

Chapter 2: Fully Recyclable Metastable Polymers and Composites

2.1 Introduction

Traditional polymeric materials rely on high-strength covalent bonds to achieve exceptional mechanical properties and maintain stability throughout their lifespans. However, covalent chemical networks are difficult to repair, and when reaching end of life, exceptionally challenging to recover/recycle. The conditions and energy required to break down these networks (e.g. T > 400 °C, supercritical fluids, or concentrated acids)[1–3] make recycling end-of-life materials impractical.[4,5] Consequently, 150 million tons of end-of-life polymers are disposed of in landfills or dumped illegally each year.[4,5] Discarded plastics represent both immediate (e.g. choking and entanglement hazards) and long term (e.g. release and concentration of persistent organic pollutants) environmental concerns, as well as significant economic losses (estimated at $200 billion in raw materials annually).[4–6]

In contrast to synthetic polymeric materials, biological materials take a much different approach to ensure stable, long term performance coupled with ease of recycling. Bone tissue, for example, undergoes cycles of degradation and formation in response to changes in mechanical stress, a process known as remodeling.[7] Through these cycles, bone tissue not only heals in response to damage, but also recycles end-of-life tissue.[8] We envisage a synthetic mimic to bone remodeling using a polymer capable of undergoing an indefinite number of degradation (depolymerization) and formation (polymerization) cycles in response to a desired stimulus. We also seek to develop materials capable of recycling under relatively mild conditions through volatile and low-viscosity monomers, allowing facile reclamation of any incorporated secondary species (e.g. fillers or fiber reinforcements) in pristine condition, a feat which remains challenging when recycling conventional fiber-reinforced polymer composites (FRPCs).[1,9–12]

Low ceiling temperature (T_c) polymers that rapidly and selectively depolymerize in response to a stimulus[13] are promising mimics to bone remodeling. These polymers have been demonstrated to depolymerize in the presence of a variety of environmental stimuli,[14–29] allowing material selection to be tailored to various processing conditions and applications. Low T_c polymers have found utility in lithographic resists,[30,31] transient electronics,[28,32,33] signal amplification,[34–36] triggered release,[37,38] block copolymers,[39,40] and smart packaging[41]. Recycling stimuli-responsive low T_c polymers has only been reported for poly(benzyl ether)s,[21] cyclic poly(phthalaldehyde) (cPPA),[22] and poly(ethyl glyoxylate)s[17]. However, these processes were limited by low yields and the inability to produce materials with properties equivalent to the pristine material. Baker and coworkers were only able to recover benzyl ether monomers in 26% yield, and the recycled poly(benzyl ether) suffered from a 22% reduction in number average molecular weight (M_n).[21] Diesendruck and coworkers reported ca. 67% recovery of *o*-phthalaldehyde, but they resynthesized linear poly(phthalaldehyde) instead of cPPA.[22] Fan and coworkers reported a 12% repolymerization yield of poly(ethyl glyoxylate) with a 95% decrease in M_n.[17] Routes to chemically recyclable polymers have also been explored with the ring-opening polymerization of γ-butyrolactone derivatives.[42,43] Zhu and coworkers reported quantitative recovery of the monomer upon heating at 180 °C for 3-5 h in the presence of $ZnCl_2$ (2 mol %), and direct repolymerization was possible with addition of a metal catalyst to the recovered monomer.[43]

Here we report on the thermally-mediated recycling of cPPA and carbon fiber-reinforced cPPA composites. At temperatures near 100 °C, the acetal backbone of cPPA was cleaved, yielding a thermodynamically unstable polymer chain (T_c = -42 °C)[27,29,44–46]. The low T_c of the reactive polymer chain favored rapid depolymerization to the monomer *o*-phthalaldehyde (*o*PA), which is volatile at the conditions required to initiate depolymerization (*o*PA b.p. = 83 °C at 0.8 torr). The

gaseous *o*PA was recovered in a cold trap and subsequently repolymerized to complete one cycle. Chemical and mechanical properties of original and recycled polymer were compared with gel permeation chromatography, NMR spectroscopy, dynamic mechanical analysis, and quasi-static tension. Additionally, cPPA composites with either continuous carbon fiber or carbon nanofiber reinforcements were produced via solvent casting and thermally recycled. We report cPPA as a first-in-class example and model polymer system for the development of fully recyclable plastics and polymer composites.

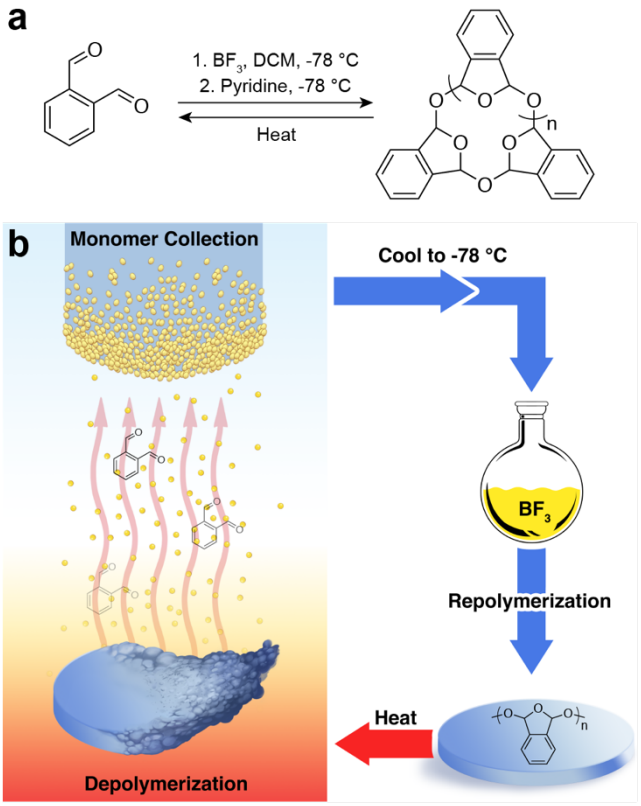

Figure 2.1. a, Thermally-mediated polymerization and depolymerization of cPPA. b, Illustration of cPPA depolymerization, monomer transport and collection, and repolymerization processes inherent to the envisaged recycling protocol (artwork was created by Jose Luiz Vasquez, Imaging Technology Group, Beckman Institute for Advanced Science and Technology, University of Illinois at Urbana-Champaign).

Our approach to thermally-mediated recycling is summarized in **Figure 2.1**. cPPA films were generated via drop casting cPPA/chloroform solutions (100 mg cPPA/mL chloroform) into polytetrafluoroethylene-lined petri dishes.[32] Film thickness was tailored to meet the demands of

various tests by adjusting the initial amount of solution cast onto the substrates. Films retained mechanical integrity under ambient conditions until exposed to high temperatures (ca. 100 °C), which led to cPPA depolymerization with concomitant evaporation of the monomer, *o*PA. The volatile monomer was condensed as a solid on a cold-finger. Recovered monomer was repolymerized by cooling to -78 °C in dichloromethane, treating with BF_3, quenching with pyridine, and precipitating from methanol, to complete one cycle or generation. Three full cycles (i.e. four generations of material) have been characterized, and it is expected that this process is indefinitely repeatable.

2.2 Thermal Depolymerization of Cyclic Poly(Phthalaldehyde)

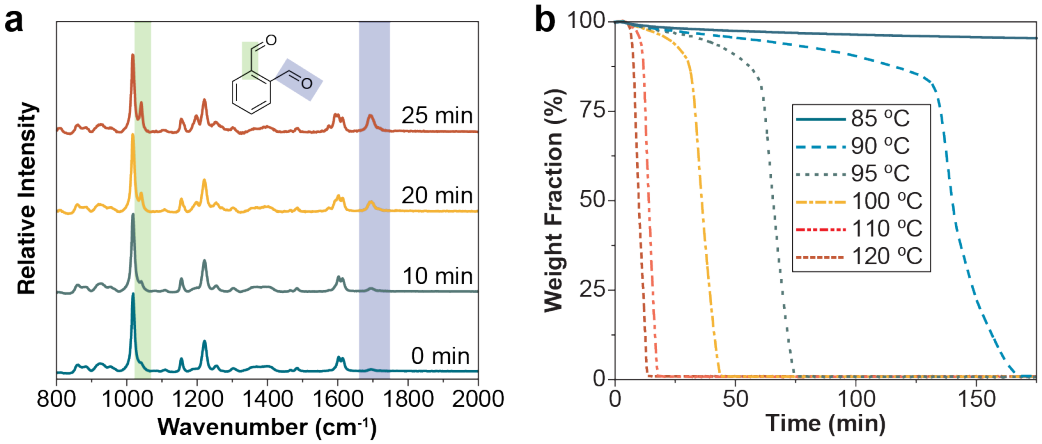

Figure 2.2. Chemical characterization of thermally-initiated cPPA depolymerization | a, Raman spectra collected in real time of a cPPA film heated at 100 °C. b, Isothermal TGA traces of cPPA films.

Thermal depolymerization of cPPA was analyzed chemically by Raman spectroscopy (**Figure 2.2a**). cPPA films (40 µm thickness) were placed on a heated stage maintained at 100 °C and spectra were obtained in real time. Depolymerization was marked by a decrease in the characteristic –COC– peak (1020 cm^{-1}) of the acetal backbone. Simultaneous appearance and growth of peaks corresponding to the –C-CHO– (1040 cm^{-1}) and carbonyl (1680 cm^{-1}) of *o*PA suggested clean unzipping of cPPA to *o*PA. After their initial growth, the intensity of peaks at

1040 cm^{-1} and 1680 cm^{-1} began to decrease, indicating evaporation of the monomer. Eventually, Raman signal was lost, marking complete depolymerization and monomer evaporation.

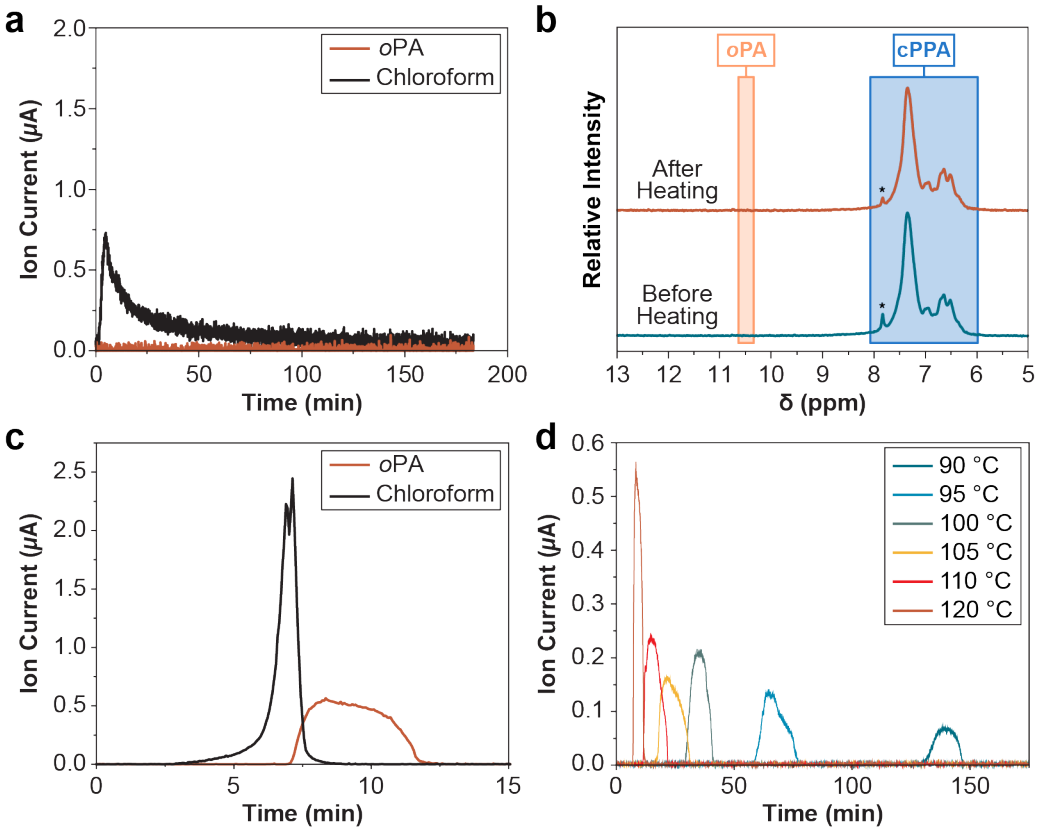

Figure 2.3. Spectroscopic characterization of cPPA thermal depolymerization | a, MS detection of chloroform (*m/z* 83) and *o*PA (*m/z* 134) evolved during TGA isotherm of 40 µm thick cPPA film at 85 °C. b, ^{1}H NMR spectra (60 MHz, THF-d_8) of the cPPA before and after the TGA isotherm at 85 °C (*residual chloroform). c, MS detection of chloroform (*m/z* 83) and *o*PA (*m/z* 134) evolved during TGA isotherm of 40 µm thick cPPA film at 120 °C. d, MS detection of *o*PA (*m/z* 134) evolved during TGA isotherms of 40 µm thick cPPA films at the specified temperatures.

Thermal gravimetric analysis was employed to monitor the depolymerization and monomer evaporation phenomena in 40 µm thick cPPA films and determine the optimal recycling conditions (**Figure 2.2b**). Minimal mass loss (4.6 wt%) was observed during a 3-hour isotherm at 85 °C. MS analysis of the gases evolved during the isotherm showed that the mass loss was attributable to residual chloroform (base peak: *m/z* 83) from solvent casting instead of *o*PA formation (**Figure 2.3a**). The ^{1}H NMR spectrum of the film remaining in the TGA pan was characteristic of cPPA and free of any *o*PA signatures, suggesting minimal cPPA depolymerization (**Figure 2.3b**). There

was a small shift in the GPC trace after the 3-hour isotherm, and the polymer exhibited only a minor (6.4 %) decrease in molecular weight. These findings indicate that cPPA is stable for extended periods of time at temperatures as high as 85 °C, providing a large temperature window for material applications.

Complete mass loss (< 1 wt% residue) was observed during 3-hour isotherms at temperatures ≥ 90 °C (**Figure 2.2b**). In each TGA trace above 85 °C, a plateau region prior to the onset of rapid mass loss was observed. The gases evolved during the plateau region were confirmed to be residual chloroform (**Figure 2.3c**). Modest increases in temperature significantly decreased the duration of the plateau region. Onset time, determined via the intersection of tangents to the plateau region and the linear region of rapid mass loss, decreased from 130.5 ± 2.9 min to 59.2 ± 0.9 min by increasing the temperature from 90 °C to 95 °C. Further increasing the temperature to 120 °C reduced the onset time to 7.0 ± 0.3 min. The onset of rapid mass loss coincided with the appearance of *o*PA signals (molecular ion peak: *m/z* 134) in MS analyses of the gases evolved during TGA traces (**Figure 2.3d**).

After the onset of degradation, weight fraction decayed linearly. Assuming zero-order kinetics, rate constants were obtained by applying a linear fit to the region of rapid mass loss. Depolymerization with concomitant monomer evaporation accelerated with temperature according to Arrhenius kinetics (**Figure 2.4**). A linear fit of the Arrhenius relationship provided an apparent activation barrier of 13.4 kcal/mol for the coupled process. The relatively small activation barrier for cPPA depolymerization and subsequent *o*PA evaporation is in great contrast to the thermal degradation of traditional thermoplastics. Polyolefins such as polypropylene, polystyrene, and high density polyethylene have pyrolysis activation barriers of 43,[47] 47,[48] and 57 kcal/mol,[47]

respectively. These high activation barriers lead to thermal degradation onsets in excess of 300 °C[47,48] and a marked increase in the energy required for recycling.

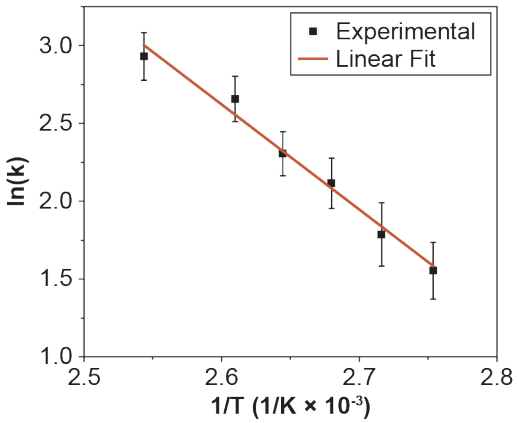

Figure 2.4. Arrhenius fit of zero-order rate constants obtained from isothermal TGA experiments (n = 3).

Aside from the steep energetic barriers, recycling traditional thermoplastics remains challenging due to the formation of complex small molecule mixtures during polymer degradation.[4] The desired monomer must be separated from the mixture in pure form to obtain high quality materials upon repolymerization. While the advent of low T_c polymers has enabled mild depolymerization conditions, recycling attempts were limited by an inability to recover the monomer in sufficient purity. For example, depolymerization of poly(benzyl ether)s with 1,8-diazabicyclo[5.4.0]undec-7-ene necessitated purification of the monomer with hot hexanes.[21] Repolymerization was possible, but optimization is required to recover the monomer in high yield and purity. The evolution of volatile monomers during depolymerization of poly(ethyl glyoxylate)s simplified monomer collection, but the air sensitivity of ethyl glyoxylate prevented synthesis of high molecular weight recycled polymer.[17] The authors have suggested distillation (performed at 130 °C)[26] of the depolymerization product as a means to improve the quality of the recycled polymer, but this represents an additional recycling step and energetic input. The thermal depolymerization of cPPA, which proceeds under mild conditions and produces volatile monomers

that are stable under ambient conditions for extended periods, addresses the challenges presented above.

2.3 Thermally Mediated Recycling of cPPA

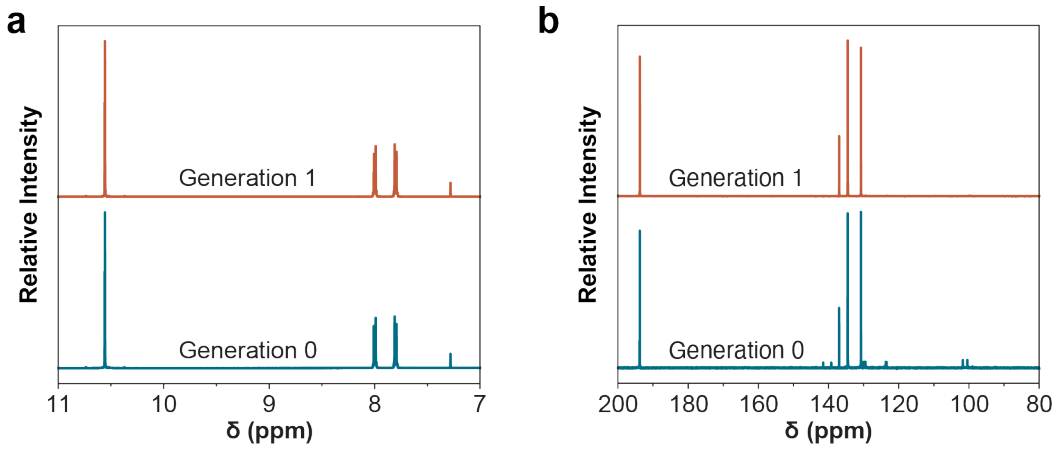

Figure 2.5. Chemical characterization of recovered *o*PA | a, ^{1}H (500 MHz, $CDCl_3$) and b, ^{13}C (500 MHz, DMSO-d_6) NMR spectra of virgin (generation 0) *o*PA and *o*PA recovered during cPPA thermal depolymerization (generation 1).

During the depolymerization of cPPA in a sublimation apparatus under moderate vacuum (0.1 torr), the white, fibrous polymer rapidly transformed into a yellow liquid that boiled as it was formed. Facile condensation of the volatile product as a solid was possible with a cold-finger maintained at 20 °C. The yellow crystalline solid was confirmed to be *o*PA by ^{1}H NMR. Comparison of ^{1}H (**Figure 2.5a**) and ^{13}C (**Figure 2.5b**) NMR spectra of the recovered (generation 1) *o*PA with that of *o*PA recrystallized directly after purchase (generation 0) suggested that generation 1 *o*PA was of sufficient quality to permit direct repolymerization. Interestingly, the purity of recycled *o*PA was greater than generation 0 *o*PA. Trace impurities were detected by ^{13}C NMR in generation 0 *o*PA, and polymerization of this monomer generated 70 kDa polymer. Synthesis of higher molecular weight generation 0 cPPA (as high as 201 kDa) was possible when the monomer was recrystallized an additional time. In contrast, no impurities were detected by ^{13}C NMR in generation 1 *o*PA, and polymerization of recycled monomer yielded recycled polymer

with comparable or even higher molecular weight than generation 0 cPPA. Recycled cPPA exhibited number average molecular weights as high as 270 kDa.

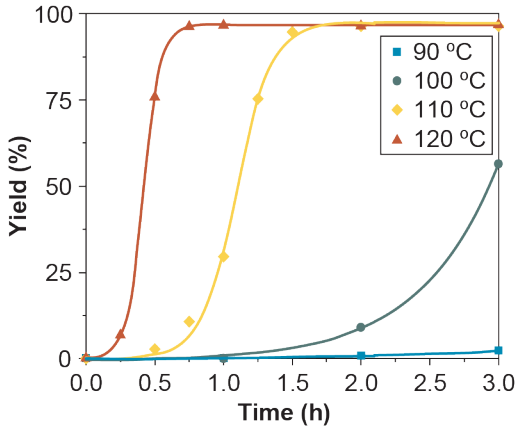

Figure 2.6. Time-dependent *o*PA yields during depolymerization of cPPA in a sublimator maintained at 0.1 torr and the specified temperatures. Presented values were corrected to account for residual solvents in the starting polymer. Solid lines represent sigmoidal fits of the obtained experimental data.

Recovery of the monomer at varied depolymerization temperatures is demonstrated in **Figure 2.6**. Consistent with observations during TGA experiments, an initial dwell time was followed by the rapid and complete depolymerization of the polymer and evaporation of the monomer. It was found that *o*PA was recovered quantitatively, within experimental limits, on the cold-finger of the sublimator (97% yield). Quantitative recovery of *o*PA was possible within 0.75 h at 120 °C and 1.5 h at 110 °C (**Figure 2.6**). Depolymerization times were extended to 20 h to achieve quantitative monomer recovery at 90 °C, a significant increase in time given the relatively small change in temperature. The time-temperature relationship shown here demonstrates the feasibility of tailored recovery processes.

The molecular weight of recycled cPPA was found to be independent of the temperatures used to depolymerize virgin polymer in this study (**Figure 2.7a**). To ensure sufficient monomer recovery, we performed all depolymerizations at the given temperatures until no polymer remained in the bottom vessel of the sublimation apparatus (between 0.75 and 20 h). Depolymerizations conducted at 90 °C and 120 °C allowed for the synthesis of recycled polymer with $M_n = 248 \pm 21$

kDa and 228 ± 10 kDa, respectively. For all utilized depolymerization temperatures, any differences in recycled polymer molecular weight were negligible at the 95% confidence level.

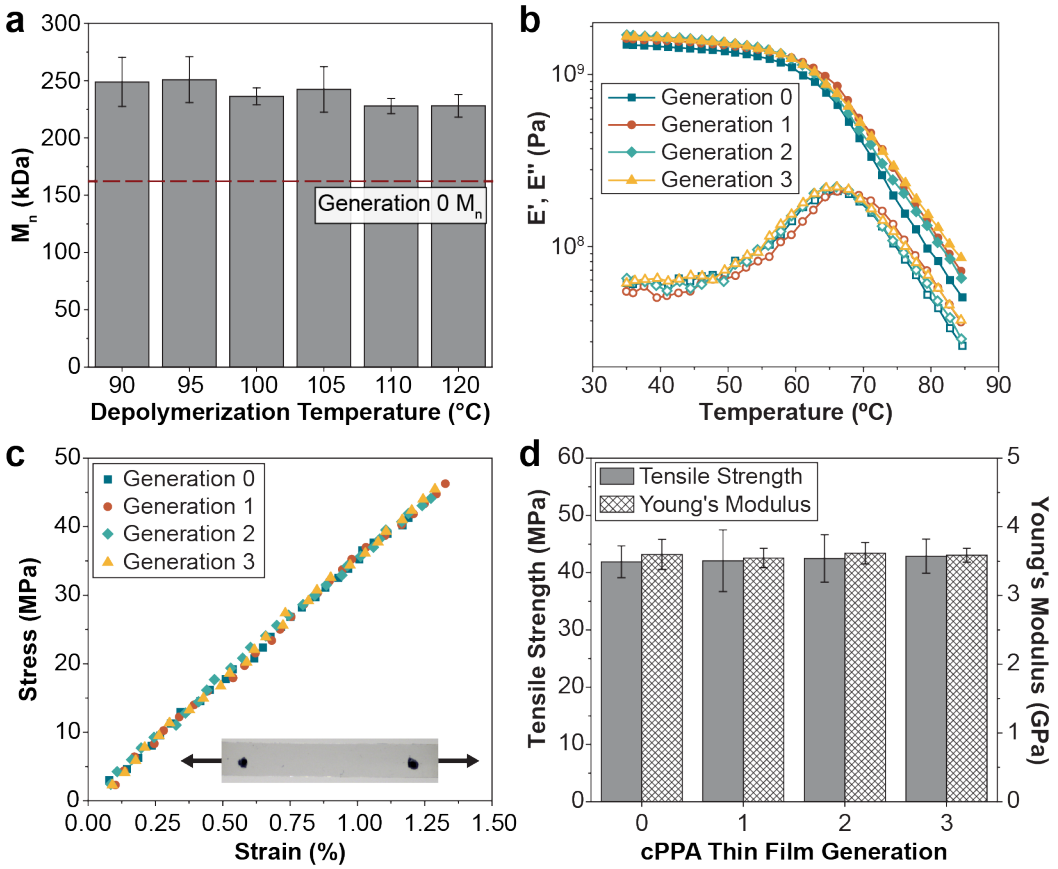

Figure 2.7. Evaluation of the chemical and mechanical properties of virgin and recycled materials | a, Number average molecular weight (M_n) of generation 1 cPPA created following the depolymerization of generation 0 cPPA at the specified temperature. Polydispersity indices are provided in Table S3. Reported values and error bars represent the average and one standard deviation, respectively (n = 3). Red dashed line represents generation 0 cPPA molecular weight. Polydispersity index values are provided in Table S3. b, Representative thermomechanical responses of virgin and recycled cPPA films determined via dynamic mechanical analysis. Storage modulus represented by solid symbols, and loss modulus represented by open symbols. c, Representative stress-strain curves for cPPA thin films under quasi-static tensile loading (Inset represents an example cPPA thin film with points applied for the virtual extensometer. Distance between virtual extensometer points was maintained at 25 mm. Arrows indicate the loading direction). d, Mechanical properties of virgin and recycled cPPA thin films. Reported values and error bars represent the average and one standard deviation, respectively (n = 5).

Given that materials typically suffer a reduction in properties during traditional recycling processes,[49–51] the mechanical properties of virgin and recycled cPPA were assessed with dynamic mechanical analysis (DMA, **Figure 2.7b**) and quasi-static tension (**Figure 2.7c,d**). cPPA thin films (120 μm thickness) were prepared for DMA by drop casting in a chloroform-saturated

environment, which slowed the solvent evaporation rate, ensuring uniform thickness and defect-free films. The films were dried undisturbed in the saturated environment for 18 h, dried *in vacuo* (0.1 torr) for 24 h at room temperature, and subsequently annealed at 70 °C for 30 minutes to remove any residual stress from solvent casting. The thin films were subjected to dynamic temperature sweeps under oscillatory load until a maximum temperature of 85 °C. The films showed no signs of depolymerization during DMA experiments. The tested films were recycled by heating to 120 °C for 1 h *in vacuo*, polymerizing the collected monomer, and solvent casting the resulting polymer. This process was repeated until three generations of recycled films were prepared and tested. **Figure 2.7b** demonstrates the similarities in viscoelastic properties of virgin and recycled cPPA films. All four generations of polymer films exhibited experimentally identical storage moduli at 35 °C (1.6 ± 0.1 GPa). The films remained in glassy regimes until transition temperatures of ca. 65 °C were reached – the glass transition temperatures for each generation were identical at the 95% confidence level.

To obtain specimens of the fidelity required for thin film tensile testing, we utilized a tape casting method in lieu of drop casting. cPPA/chloroform (125 mg cPPA/mL chloroform) solutions were poured onto an ultra-high-molecular-weight polyethylene substrate, and the thickness of the film was set with a high precision film applicator. As in the drop casting procedure, films were then dried undisturbed for 18 h in a chloroform saturated environment, dried *in vacuo* (0.1 torr) at room temperature for 24 h, and annealed at 70 °C. Films were tested under quasi-static tensile loading until failure and then recycled. The similarities in the stress-strain response and bulk properties of generation 0-3 cPPA films is evident in **Figure 2.7c,d**. All tested cPPA films deformed elastically under tensile loading until brittle failure at approximately 1.2% strain. Impressively, generation 0 cPPA demonstrated a modulus (3.6 GPa) and tensile strength (41.9

MPa) comparable to industry standard thermoplastics such as polystyrene,[52] polyethylene terephthalate,[53] and high-density polyethylene[54]. Virgin and recycled films possessed experimentally identical Young's moduli (3.6 ± 0.1 GPa), and the films retained at least 100% of the original tensile strength through three depolymerization and repolymerization cycles. Any differences in properties among generations were negligible at the 95% confidence level. Thermally-mediated cPPA recycling represents the first approach to low T_c polymer recycling which retains both chemical and mechanical properties of the polymer.

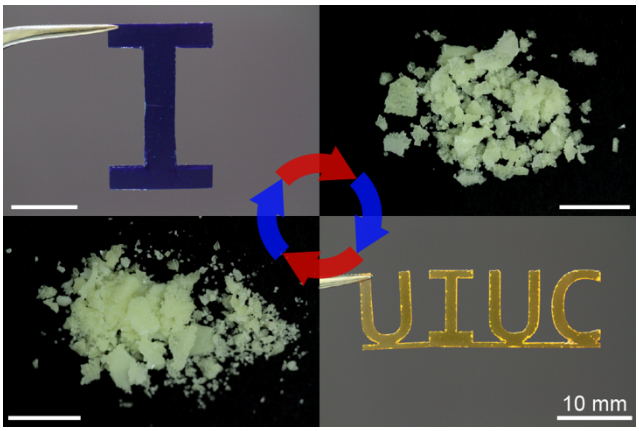

Figure 2.8. Photographs of solvent cast cPPA films (dyed with methylene blue or Astrazon Orange R during the casting process and laser cut into specified shapes for visualization) and the monomer (*o*PA) collected following depolymerization of the dyed films. The dyed films are held by metal tweezers. Blue arrows represent polymerization and film casting, and red arrows represent depolymerization and monomer collection.

The presence of dyes and other additives in plastics poses an additional challenge during recycling. Traditional polymers must be separated from other plastics and additives prior to recycling.[5,50] Impurities in the recycling stream often result in mechanical defects, discoloration, or undesirable odors which diminish the value of the recycled product. In contrast, cPPA processed with various dyes was successfully recycled without first removing the dye (**Figure 2.8**). A blue cPPA film was generated by adding 2.5 wt% (vs. cPPA) methylene blue into a cPPA/chloroform solution prior to solvent casting. The resulting film was laser cut into an I as shown in **Figure 2.8** (top left) and subsequently depolymerized at 120 °C. *o*PA (top right) was collected (97% yield)

without any trace of methylene blue as confirmed by ^{1}H NMR spectroscopy (**Figure 2.9a**), and methylene blue remained at the bottom of the sublimation apparatus. Polymerization of the recovered *o*PA yielded 241 kDa polymer. The resulting cPPA was solvent cast with 2.5 wt% Astrazon Orange R, and the orange film was laser cut into the UIUC logo shown in **Figure 2.8** (bottom right). Depolymerization of the orange film generated *o*PA (bottom left) that was free of Astrazon Orange R (**Figure 2.9b**), and polymerization of this monomer produced 238 kDa cPPA. We anticipate that cPPA will be recyclable in the presence of a variety of additives (dyes, plastics, fillers, etc.), and the simplicity of direct repolymerization will be maintained provided that the additives do not produce volatile products at cPPA depolymerization temperatures. This feature offers a solution to a key problem in FRPC recycling: removal of the polymer matrix without damaging the fiber reinforcement.

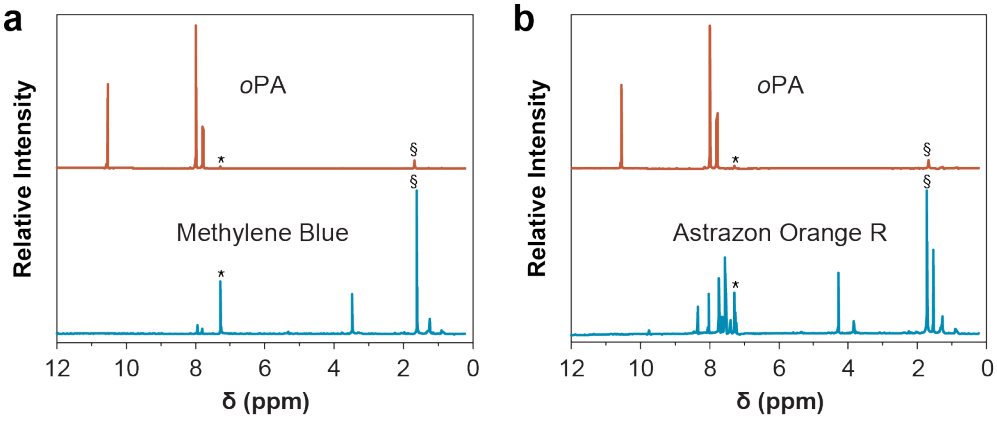

Figure 2.9. a, ^{1}H NMR (500 MHz, $CDCl_3$) of methylene blue (bottom) and *o*PA obtained during depolymerization of film dyed with methylene blue (top). b, ^{1}H NMR (500 MHz, $CDCl_3$) of Astrazon Orange R (bottom) and *o*PA obtained during depolymerization of film dyed with Astrazon Orange R (top) ($^{*}CHCl_3$, §water).

2.4 Recycling of cPPA Composites

When utilizing conventional FRPC recycling strategies such as pyrolysis or solvolysis, the polymer matrix is fully oxidized or decomposed to secondary value chemicals at temperatures in excess of 200 °C, enabling reclamation of the fibers.[1,9] However, due to the stability of the polymer

matrix and severity of degradation conditions, the fibers are typically recovered in a damaged state. Mild degradation conditions (i.e. low pyrolysis temperatures) do not allow for complete removal of the matrix. Reclaimed fibers are typically encased in a large amount of residual resin, limiting the possibility of successful re-impregnation with matrix resin.[10] Harsh degradation conditions, on the other hand, result in fibers that suffer from severe pitting and surface defects which cause significant decreases in fiber strength.[10] In either case, the value of the reclaimed fibers is significantly diminished. The ability to completely depolymerize cPPA and volatilize *o*PA under mild conditions (temperatures as low as 90 °C) allows for both complete matrix removal and fiber property retention when recycling.

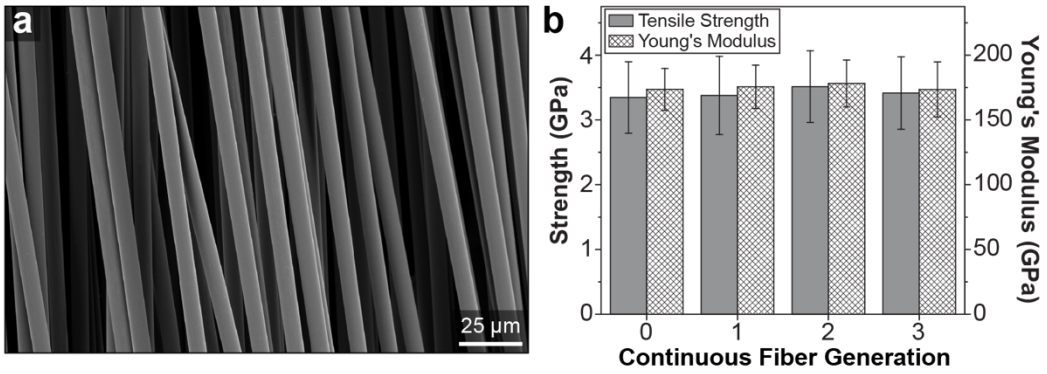

Figure 2.10. Characterization of continuous carbon fibers reclaimed from cPPA | a, Representative SEM image of continuous carbon fibers recovered after depolymerizing the cPPA matrix at 120 °C and 0.1 torr for 1 h. b, Mechanical properties of virgin and recycled continuous carbon fibers determined via single fiber tension. Reported values and error bars represent the Weibull mean and variance, respectively ($n \geq 50$).

The properties of carbon fibers reclaimed after depolymerization of cPPA matrices were evaluated by SEM (**Figure 2.10a**) and single fiber tension (**Figure 2.10b**). For ease of analysis, continuous carbon fibers were considered. Composites were prepared by solvent casting cPPA in the presence of a single tow of continuous fibers. The resulting films were heated *in vacuo* at 120 °C for 1 h to depolymerize the matrix and recover the fibers. Casting and depolymerization were repeated until generation 3 samples were acquired. A qualitative evaluation of the fiber

morphology and the amount of residual matrix was obtained with SEM, shown in **Figure 2.10a**. Fibers were reclaimed nearly free of residue. TGA analysis confirms less than 0.6% of the mass of starting polymer in a film remains on the fibers after depolymerization at 120 °C for 1 h. We anticipate that any residues, which are likely small molecules, are easily removable with organic solvents. Additionally, reclaimed fibers showed no evidence of surface defects or pitting, a result of the mild depolymerization conditions. The mechanical integrity of the reclaimed fibers was determined via single fiber tensile tests (**Figure 2.10b**). All reclaimed fibers were found to retain their original strength and stiffness, and any deviations were negligible at the 95% confidence level. The excellent property retention and minimal amounts of matrix residue suggest that these reclaimed fibers will exhibit exceptional performance when reused.

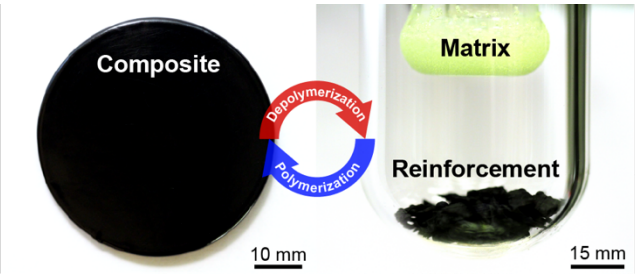

Figure 2.11. Photographs of a cPPA/CNF composite film (left) and sublimation apparatus after heating the composite film to 120 °C for 1 h (right). Depolymerization is achieved by heating *in vacuo* (0.1 torr) at ca. 100 °C. The film is recovered after *repolymerization* and solvent casting from chloroform.

Carbon nanofiber-reinforced composite films were prepared to assess the recyclability of cPPA FRPCs by casting chloroform solutions of carbon nanofibers (CNF) and cPPA (0.15 g CNF, 1 g cPPA, 0.9 mL chloroform) with the previously described drop casting and tape casting procedures (**Figure 2.11**, left). The use of carbon nanofiber composites in place of continuous or short fiber composites allowed for characterization of recycled composite films without the bias of fiber damage incurred during mechanical testing. Upon heating the CNF composite films to the desired depolymerization temperature in a sublimation apparatus, the films rapidly disintegrated and a yellow solid (*o*PA) was collected on the condenser. *o*PA was recovered quantitatively within 1 h

at 120 °C and 0.1 torr, and the fibers remained in place, indicating complete separation of the matrix and reinforcement phases (**Figure 2.11**, right). The CNF reinforcement was removed from the lower vessel as flakes of agglomerated fibers that immediately collapsed upon agitation, and the collected *o*PA (97% yield) was repolymerized directly (M_n = 231 kDa). The reclaimed fibers and recycled polymer were cast to make a recycled composite film. The properties of virgin and recycled composite films were compared via quasi-static tension (**Figure 2.12**). The recycled composites exhibited mechanical properties that were experimentally identical to the virgin composite. All four generations exhibited moduli of 4.5 ± 0.3 GPa and tensile strengths of 30.3 ± 3.5 MPa. The recycled composites were found to retain at least 100% of the original tensile strength and at least 99% of the original modulus; the differences among generations were all negligible at the 95% confidence level. This clearly demonstrates the utility of cPPA for the production of composite materials with facile recycling strategies that yield high value products.

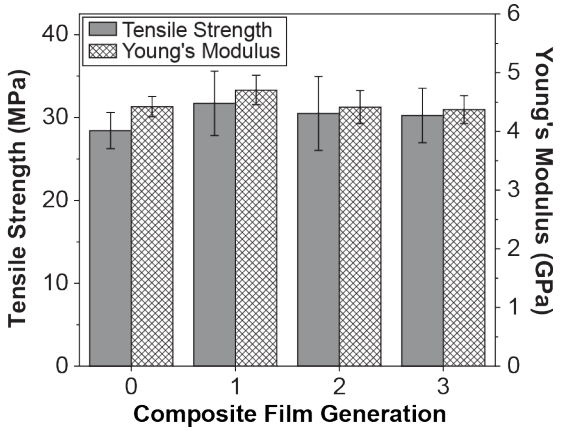

Figure 2.12. Mechanical properties of virgin and recycled cPPA/CNF composite films determined via quasi-static tension. Reported values and error bars represent the average and one standard deviation, respectively (n = 5 for Tensile Strength and n = 6 for Young's Modulus).

2.5 Fabrication of High Performance cPPA Monoliths and Composites

The relatively low degradation temperatures of cPPA (ca. 100 °C) and unpredictable thermal degradation behavior[46] present significant barriers to thermal processing of cPPA composite materials. Feinberg and coworkers recently demonstrated that removal of residual Lewis acid

catalysts through dropwise precipitation and the incorporation of a Lewis base stabilizer, *N,N'*-di-*sec*-butyl-*p*-phenylenediamine (DBPDA), significantly improved the thermal stability and allowed for more predictable degradation behavior.[46] Further, the addition of phthalate plasticizers reduced glass transition temperatures to well below the onset of thermal degradation, enabling the production of monoliths through thermoforming. However, the utilized formulations were not optimized for material performance, and the very high loadings of plasticizer and stabilizer led to soft, tacky plastics at room temperature.

To manufacture high performance transient plastics, a delicate balance among thermal stability, processability, and performance must be achieved. The concentration of small molecule plasticizers and stabilizers, which both contribute to a decay in mechanical integrity, must be minimized to achieve high performance, significantly reducing the available processing window. In addition, to maintain the ease of recycling presented above, the small molecule additives must have sufficiently different boiling points from *o*PA (267 °C). Diphenyl phthalate (DPP) was selected as a plasticizer for its high boiling point (ca. 400 °C), and DBPDA was selected as the stabilizer due to its ability to improve the thermal stability at extremely low concentrations (as little as 0.5 phr needed) and high boiling point (313 °C).

Feedstocks of various polymer blends were generated by casting from solutions of dichloromethane. After drying overnight in a dichloromethane saturated environment, the films were pulverized with a coffee grinder, and the resulting powder was dried *in vacuo*. The dried powder was then transferred to an aluminum mold and pressed at various temperatures and 20 MPa for 15 min. At very low concentrations of DPP (2.5 phr) and DBPDA (0.5 phr), samples pressed at 110 °C or below were filled with voids and cracks (**Figure 2.13**), significantly reducing their mechanical integrity. Increasing the temperature to 115 °C resulted in substantial

depolymerization, evidenced by severe softening of the material and the appearance of a large aldehyde peak in the ^{1}H NMR of the pressed samples. Increased pressure (40 MPa), which was much greater than pressure typically utilized during thermal processing of high-density polyethylene[55], at 110 °C was also attempted with minimal reduction in defects. Increasing the plasticizer loading to 5 phr resulted in defect free samples with a modulus of 2.7 ± 0.4 GPa and ultimate tensile strength (UTS) of 21.4 ± 0.4 MPa. Further increasing the plasticizer loading enables thermoforming at reduced temperatures and pressures, alleviating the risk of unwanted thermal depolymerization, but at the expense of mechanical performance. For example, samples with 10 phr DPP exhibited moduli of 1.7 ± 0.5 GPa and UTS of 16.8 ± 0.3 MPa. The properties of monolithic cPPA blends are comparable with industry standard thermplastics[52–54]; however, the proximity of the processing temperature to the thermal degradation temperature is likely to create reproducibility issues and sporadic cPPA depolymerization. Improvement in the thermal stability of cPPA is required for further advancement of the material and the potential for 3D printing of transient plastics.

Figure 2.13. Optical images of cPPA dogbones (2.5 phr DPP, 0.5 phr DBPDA) pressed at 20 MPa and 110 °C for 15 minutes.

After careful optimization of cPPA blends and processing parameters, cPPA nanocomposites were explored. To prevent cPPA depolymerization and account for the addition of inert fillers, higher plasticizer loadings were utilized. Feedstock blends were prepared by solvent casting mixtures of cPPA, DPP (20 phr), DBPDA (0.5 phr), and carbon nanofibers (CNF, x phr) in

dichloromethane saturated environments. To ensure dispersal of the nanofibers, mixtures were sonicated for 15 min prior to casting. The feedstocks were pulverized in a coffee grinder, and the powders were pressed in an aluminum mold at 100 °C and 20 MPa. The presence of carbon nanofibers had little influence on pressing at the higher plasticizer loadings under these conditions. Samples (**Figure 2.14**) were free of voids and defects, and the incorporation of nanofibers significantly improved mechanical properties. With 5 phr CNF, samples with a modulus of 4 GPa and tensile strength of 45 MPa were obtained. Increasing further to 15 phr CNF yielded samples with a modulus of 5 GPa while the tensile strength remained the same at 45 MPa. These initial results hold promise in the production of electrically active and electrically degradable transient materials.

Figure 2.14. cPPA nanocomposite with 15 phr CNF.

2.6 Conclusions

The material system presented here is the first demonstration of a fully recyclable polymeric matrix material with full monomer recovery and retention of polymer chemical and mechanical properties during recycling. cPPA is a model for a new generation of polymers and composites designed for ease of recycling. We have demonstrated the ability to depolymerize cPPA and quantitatively recover high-purity monomer under mild thermal conditions. Multiple cycles of depolymerization and repolymerization were performed, each yielding polymer with excellent

properties. Carbon fiber-reinforced cPPA composites were produced via solvent-casting from chloroform, and the resulting films were recycled without damaging the reinforcement phase or loss in mechanical properties over multiple generations. The presented process, which relies solely on a thermal stimulus, is easily scalable. Efficient scaling will require optimization of heat transfer during depolymerization and of condensation of the monomer. Thermally-mediated recycling of cPPA is not limited to fiber-reinforced composite materials but will likely find use in the electronics and consumer product industries as well. The development of polymers capable of undergoing an indefinite number of depolymerization and repolymerization cycles in response to specific environmental stimuli (e.g. temperature) not only impacts recyclability, but also opens new opportunities for self-healing and environmentally adaptive materials.

2.7 Experimental Details

2.7.1 cPPA Synthesis and Recycling

cPPA was synthesized according to literature procedures.[14,29,32] *o*PA was purified by recrystallization from a 5:2 dichloromethane:hexanes mixture and stored under argon atmosphere. *o*PA received from the manufacturer and purified by recrystallization served as virgin (generation 0) material. The purified *o*PA (12.0 g, 89.5 mmol) was dissolved in anhydrous dichloromethane (96 mL) under an inert argon atmosphere in flame dried glassware. The solution was cooled to -78 °C and 2 mol% boron trifluoride diethyl etherate (240 µL, 1.8 mmol) was added dropwise. The reaction was equilibrated for 2 h at -78 °C prior to the addition of pyridine (600 µL, 7.5 mmol). Following an additional 2 h equilibration period at -78 °C, polymer was precipitated from methanol and washed with diethyl ether. Vacuum filtration afforded a white solid in quantitative yield. cPPA depolymerizations were performed in a 40 mL Dailey vacuum sublimator from Chemglass at 0.1 torr and 120 °C for 1 h, unless otherwise specified. The lower portion of the sublimator was

maintained at the target temperature with a silicone oil bath heated on an IKA RCT Basic MAG digital round-top stirring hot plate equipped with an IKA ETS-D5 programmable temperature probe. *o*PA was collected *in situ* on a cold-finger maintained at 20 °C with a continuous stream of water. *o*PA was removed from the cold-finger and repolymerized without any further purification to yield recycled cPPA.

2.7.2 Preparation of cPPA Thin Films

cPPA thin films were prepared according to a literature procedure.[32] In a typical experiment, cPPA (100 mg) was dissolved in chloroform (1 mL). To minimize defects and ensure uniform film thickness, a chloroform-saturated casting environment was generated by placing a petri dish filled with chloroform (10 mL) under a crystallizing dish (90 mm × 50 mm). The cPPA solution was drop-cast into a polytetrafluoroethylene-lined petri dish and placed in the chloroform-saturated environment. The film was dried in the saturated environment for 18 h, and subsequently dried *in vacuo* (0.1 torr) for 24 h to remove residual solvent. Film thickness (40 μm – 100 μm) was varied by adjusting the initial amount of solution cast into the dish.

2.7.3 Characterization of Thermal Depolymerization

cPPA thermal depolymerization was monitored by Raman spectroscopy using a Horiba LabRAM HR 3D Raman Confocal Imaging Microscope equipped with a 785 nm laser, 300 g/mm grating (blazed at 600 nm), a long working distance 20× objective from Olympus, and a Horiba Synapse back-illuminated deep-depletion CCD camera. Temperature control was achieved with a Linkam THMS600 heating and cooling stage. Target isothermal temperatures were reached following a linear ramp of 20 °C/min. Thermal depolymerization was also monitored by Thermal Gravimetric Analysis (TGA) with a TA Instruments Q500 TGA equipped with an evolved gas analysis furnace and platinum pans. Isothermal segments began after an initial linear ramp of 20

°C/min to the target temperature. Chloroform (*m/z* 83) and *o*PA (*m/z* 134) evolution, corresponding to the mass loss observed in TGA traces, was monitored in real time with mass spectroscopy (MS) using a TA Instruments Discovery Mass Spectrometer. The mass spectrometer included a quadrupole detector equipped with a closed ion source, triple mass filter, and a dual (Faraday and Secondary Electron Multiplier) detection system. The mass spectrometer and TGA were coupled with a heated transfer line maintained at 300 °C. All TGA and MS analyses were performed in triplicate.

2.7.4 Characterization of Virgin and Recycled Materials

^{1}H and ^{13}C NMR spectra were obtained with a Varian 500 MHz spectrometer provided by the School of Chemical Sciences NMR laboratory at the University of Illinois at Urbana-Champaign or an NMReady 60Pro 60 MHz NMR. Spectra were obtained in either chloroform-*d*, dimethyl sulfoxide-d_6, or tetrahydrofuran-d_8. cPPA molecular weight was determined via gel permeation chromatography obtained on a system comprised of a Waters 1515 Isocratic HPLC pump, a Waters 2707 autosampler, a series of four Waters HR Styragel columns (HR1, HR3, HR4, and HR5), and a Waters 2414 refractive index detector. The system was calibrated with monodisperse polystyrene standards. Analyses were performed in HPLC grade THF (flow rate = 1.0 mL/min) at 25 °C.

The mechanical properties of virgin and recycled materials were evaluated with a combination of dynamic mechanical analysis (DMA) and quasi-static tension. DMA tests on cPPA thin films were performed on a TA Instruments RSA III equipped with thin film grips supplied by TA Instruments. cPPA films were cut into rectangular samples of 30 mm × 5 mm × 120 μm using a steel punch, and the gauge length was maintained at 10 mm. Dynamic loading was applied at 1 Hz and 0.1 % strain amplitude while the temperature was increased linearly at 5 °C/min. Data was obtained for a minimum of 5 specimens.

Tensile measurements of cPPA thin films and cPPA/carbon nanofiber (CNF) composite films were performed according to ASTM Standard D882 on a custom built bi-directional-screw-driven rail table. Sample dimensions were maintained at 80 mm × 5 mm × 200 μm. Gauge length was set at 35 mm, crosshead displacement was maintained at 58.4 μm/s, and the applied load was monitored with a 220 N capacity load cell. Strain within the films was measured with a virtual extensometer (VE). Points utilized for VE analysis were applied directly to the films with flat white or black paint 5 mm from each end of the gauge length. Images were acquired every 125 ms with an Allied Vision Stingray F145c CCD camera equipped with an AF Micro-Nikkor 60 mm lens from Nikon. All equipment was controlled with LabView 2015 and a homemade program. Data was collected for a minimum of 5 specimens.

Tensile tests of continuous carbon fibers were performed in accordance with ASTM Standard D3822 on a custom-built load frame described by Jones and coworkers[56]. Single carbon fibers were selected at random, mounted on cardstock tabs with a span of 25 mm using cyanoacrylate adhesive, and loaded in displacement control at 8 μm/s until failure with a Physik Instrumente M-230S high resolution linear actuator controlled with LabView 2015 and a homemade program. Applied load was measured with a 150 g load cell (Honeywell Sensotec). The fracture surfaces were collected, and the diameters were determined optically. Data was collected for a minimum of 50 specimens. The properties of virgin and recycled continuous carbon fibers were also qualitatively analyzed with Scanning Electron Microscopy (SEM) with a Philips XL30 ESEM-FEG. Prior to SEM imaging, fibers were mounted on carbon conductive tape and sputtered with a 12 nm layer of gold/palladium via a Denton Desk II TSC turbo-pumped sputter coater.

2.7.5 Production and Testing of cPPA Monoliths and Composites.

Feedstocks were generated by mixing cPPA, diphenyl phthalate (DPP), *N,N'*-di-*sec*-butyl-*p*-phenylenediamine (DBPDA), and carbon nanofibers (CNF) at the desired concentrations in dichloromethane. Mixtures containing CNF were sonicated for 15 min to ensure dispersal of the fibers. The mixtures were poured onto an ultra-high-molecular-weight polyethylene substrate, and the thickness of the film was set at 200 μm with a high precision film applicator. The films were dried overnight in a dichloromethane saturated environment. After drying, the films were pulverized with a coffee grinder and the powder was dried for 24 h *in vacuo* (0.1 torr). Dried powders were transferred to an aluminum mold (ASTM Standard D638 Type V dogbone). The mold was preheated at the desired temperature (100 – 115 °C) for 5 min, pressed at the desired pressure (20 – 40 MPa) and temperature for 5 min, and cooled to room temperature at 20 °C min^{-1}. The samples were removed from molds and polished to remove any surface defects with a MetPrep 3 polisher from Allied High Tech Products, Inc, equipped with a series of silicon carbide grinding papers (with a minimum grit of 1200) from Buehler.

Mechanical performance of cPPA monoliths and composites were evaluated via quasi-static tension on an Instron 5984 equipped with a 150 kN load cell and video extensometer. Tensile tests were performed at a crosshead speed of 1 mm min^{-1} until material failure. Young's moduli were calculated over a range of strain from 0.1% to 0.25%.

2.8 Notes and References

2.8.1 Notes

This is a collaborative effort with multiple contributors. E.M.L performed the experiments and authored the entire text. Hector Lopez Hernandez analyzed tensile measurements. Elizabeth Feinberg assisted with collection and analysis of NMR data and contributed to the fabrication of

cPPA monoliths. Mostafa Yourdkhani assisted with experimental design. Edwin Zen assisted with single fiber tension experiments. Edgar Mejia assisted with thin film preparation. Sydney Butikofer assisted with the fabrication of cPPA monoliths.

Portions of this chapter have been published. Lloyd, E. M.; Lopez Hernandez, H.; Feinberg, A. M.; Yourdkhani, M.; Zen, E. K.; Mejia, E. B.; Sottos, N. R.; Moore, J. S.; White, S. R. "Fully Recyclable Metastable Polymers and Composites" *Chem. Mater.* **2019**, 31, 398-406. They are reproduced/adapted with permission.

2.8.2 References

1. Pickering, S. J. Recycling Technologies for Thermoset Composite Materials-Current Status. *Composites, Part A* **2006**, 37, 1206-1215.
2. Al-Salem, S. M.; Lettieri, P.; Baeyens, J. Recycling and Recovery Routes of Plastic Solid Waste (PSW): A Review. *Waste Manage.* **2009**, 29, 2625-2643.
3. George, N.; Kurian, T. Recent Developments in the Chemical Recycling of Postconsumer Poly(ethylene terephthalate) Waste. *Ind. Eng. Chem. Res.* **2014**, 53, 14185-14198.
4. Schneiderman, D. K.; Hillmyer, M. A. 50th Anniversary Perspective: There Is a Great Future in Sustainable Polymers. *Macromolecules* **2017**, 50, 3733-3749.
5. Garcia, J. M.; Robertson, M. L. The Future of Plastics Recycling. *Science* **2017**, 358, 870–872.
6. Hong, M.; Chen, E. Y.-X. Chemically Recyclable Polymers: A Circular Economy Approach to Sustainability. *Green Chem.* **2017**, 19, 3692-3706.
7. Hadjidakis, D. J.; Androulakis, I. I. Bone Remodeling. *Ann. N. Y. Acad. Sci.* **2006**, 1092, 385-396.
8. Sims, N. A.; Martin, T. J. Coupling the Activities of Bone Formation and Resorption: A Multitude of Signals Within the Basic Multicellular Unit. *BoneKEy Rep.* **2014**, 3, 481-490.
9. Pimenta, S.; Pinho, S. T. Recycling Carbon Fibre Reinforced Polymers for Structural Applications: Technology Review and Market Outlook. *Waste Manage*. **2011**, 31, 378-392.
10. Pimenta, S.; Pinho, S. T. The Effect of Recycling on the Mechanical Response of Carbon Fibres and Their Composites. *Compos. Struct.* **2012**, 94, 3669-3684.
11. Akonda, M. H.; Lawrence, C. A.; Weager, B. M. Recycled Carbon Fibre-Reinforced Polypropylene Thermoplastic Composites. *Composites, Part A* **2012**, 43, 79-86.
12. La Rosa, A. D.; Banatao, D. R.; Pastine, S. J.; Latteri, A.; Cicala, G. Recycling Treatment of Carbon Fibre/Epoxy Composites: Materials Recovery and Characterization and Environmental Impacts Through Life Cycle Assessment. *Composites, Part B* **2016**, 104, 17-25.
13. Kaitz, J. A.; Lee, O. P.; Moore, J. S. Depolymerizable Polymers: Preparation, Applications, and Future Outlook. *MRS Commun.* **2015**, 5, 191-204.
14. Kaitz, J. A.; Diesendruck, C. E.; Moore, J. S. End Group Characterization of Poly(phthalaldehyde): Surprising Discovery of a Reversible, Cationic Macrocyclization Mechanism. *J. Am. Chem. Soc.* **2013**, 135, 12755-12761.
15. Kaitz, J. A.; Diesendruck, C. E.; Moore, J. S. Divergent Macrocyclization Mechanisms in the Cationic Initiated Polymerization of Ethyl Glyoxylate. *Macromolecules* **2014**, 47, 3603-3607.
16. Fan, B.; Trant, J. F.; Gillies, E. R. End-Capping Strategies for Triggering End-to-End Depolymerization of Polyglyoxylates. *Macromolecules* **2016**, 49, 9309-9319.
17. Fan, B.; Trant, J. F.; Yardley, R. E.; Pickering, A. J.; Lagugné-Labarthet, F.; Gillies, E. R. Photocontrolled Degradation of Stimuli-Responsive Poly(ethyl glyoxylate): Differentiating Features and Traceless Ambient Depolymerization. *Macromolecules* **2016**, 49, 7196-7203.
18. Lee, O. P.; Lopez Hernandez, H.; Moore, J. S. Tunable Thermal Degradation of Poly(vinyl butyl carbonate sulfone)s via Side-Chain Branching. *ACS Macro Lett*. **2015**, 4, 665-668.

19. Possanza Casey, C. M.; Moore, J. S. Base-Triggered Degradation of Poly(vinyl ester sulfone)s with Tunable Sensitivity. *ACS Macro Lett.* **2016**, 5, 1257-1260.
20. Olah, M. G.; Robbins, J. S.; Baker, M. S.; Phillips, S. T. End-Capped Poly(benzyl ethers): Acid and Base Stable Polymers That Depolymerize Rapidly from Head-to-Tail in Response to Specific Applied Signals. *Macromolecules* **2013**, 46, 5924-5928.
21. Baker, M. S.; Kim, H.; Olah, M. G.; Lewis, G. G.; Phillips, S. T. Depolymerizable Poly(benzyl ether)-Based Materials for Selective Room Temperature Recycling. *Green Chem.* **2015**, 17, 4541-4545.
22. Diesendruck, C. E.; Peterson, G. I.; Kulik, H. J.; Kaitz, J. A.; Mar, B. D.; May, P. A.; White, S. R.; Martínez, T. J.; Boydston, A. J.; Moore, J. S. Mechanically Triggered Heterolytic Unzipping of a Low-Ceiling-Temperature Polymer. *Nat. Chem.* **2014**, 6, 623-628.
23. Peterson, G. I.; Boydston, A. J. Kinetic Analysis of Mechanochemical Chain Scission of Linear Poly(phthalaldehyde). *Macromol. Rapid Commun.* **2014**, 35, 1611-1614.
24. Peterson, G. I.; Larsen, M. B.; Boydston, A. J. Controlled Depolymerization: Stimuli-Responsive Self-Immolative Polymers. *Macromolecules* **2012**, 45, 7317-7328.
25. DiLauro, A. M.; Robbins, J. S.; Phillips, S. T. Reproducible and Scalable Synthesis of End-Cap-Functionalized Depolymerizable Poly(phthalaldehydes). *Macromolecules* **2013**, 46, 2963-2968.
26. Fan, B.; Trant, J. F.; Wong, A. D.; Gillies, E. R. Polyglyoxylates: A Versatile Class of Triggerable Self-Immolative Polymers from Readily Accessible Monomers. *J. Am. Chem. Soc.* **2014**, 136, 10116-10123.
27. Wang, F.; Diesendruck, C. E. Polyphthalaldehyde: Synthesis, Derivatives, and Applications. *Macromol. Rapid Commun.* **2018**, 39, 1700519-1700540.
28. Lee, K. M.; Phillips, O.; Engler, A. Kohl, P. A.; Rand, B. P. Phototriggered Depolymerization of Flexible Poly(phthalaldehyde) Substrates by Integrated Organic Light-Emitting Diodes. *ACS Appl. Mater. Interfaces* **2018**, 10, 28062-28068.
29. Lopez Hernandez, H.; Lee, O. P.; Possanza Casey, C. M.; Kaitz, J. A.; Park, C. W.; Plantz, C. L.; Moore, J. S.; White, S. R. Accelerated Thermal Depolymerization of Cyclic Polyphthalaldehyde with a Polymeric Thermoacid Generator. *Macromol. Rapid Commun.* **2018**, 39, 1800046-1800050.
30. Ito, H.; Ueda, M.; Schwalm, R. Highly Sensitive Thermally Developable Positive Resist Systems. *J. Vac. Sci. Technol., B: Microelectron. Process. Phenom.* **1988**, 6, 2259-2263.
31. Uzunlar, E.; Schwartz, J.; Phillips, O.; Kohl, P. A. Decomposable and Template Polymers: Fundamentals and Applications. *J. Electron. Packag.* **2016**, 138, 020802-020815.
32. Lopez Hernandez, H.; Kang, S.-K.; Lee, O. P.; Hwang, S.-W.; Kaitz, J. A.; Inci, B.; Park, C. W.; Chung, S.; Sottos, N. R.; Moore, J. S.; Rogers, J. A.; White, S. R. Triggered Transience of Metastable Poly(phthalaldehyde) for Transient Electronics. *Adv. Mater.* **2014**, 26, 7637-7642.
33. Park, C. W.; Kang, S.-K.; Lopez Hernandez, H.; Kaitz, J. A.; Wie, D. S.; Shin, J.; Lee, O. P.; Sottos, N. R.; Moore, J. S.; Rogers, J. A.; White, S. R. Thermally Triggered Degradation of Transient Electronic Devices. *Adv. Mater.* **2015**, 27, 3783-3788.
34. Phillips, S. T.; Robbins, J. S.; DiLauro, A. M.; Olah, M. G. Amplified Responses in Materials Using Linear Polymers That Depolymerize from End-to-End When Exposed to Specific Stimuli. *J. Appl. Polym. Sci.* **2014**, 131, 40992-41004.
35. Phillips, S. T.; DiLauro, A. M. Continuous Head-to-Tail Depolymerization: An Emerging Concept for Imparting Amplified Responses to Stimuli-Responsive Materials. *ACS Macro Lett.* **2014**, 3, 298-304.
36. DiLauro, A. M.; Phillips, S. T. End-Capped Poly(4,5-dichlorophthalaldehyde): A Stable Self-Immolative Poly(aldehyde) for Translating Specific Inputs Into Amplified Outputs, Both in Solution and the Solid State. *Polym. Chem.* **2015**, 6, 3252-3258.
37. Esser-Kahn, A. P.; Odom, S. A.; Sottos, N. R.; White, S. R.; Moore, J. S. Triggered Release from Polymer Capsules. *Macromolecules* **2011**, 44, 5539-5553.
38. DiLauro, A. M.; Abbaspourrad, A.; Weitz, D. A.; Phillips, S. T. Stimuli-Responsive Core-Shell Microcapsules with Tunable Rates of Release by Using a Depolymerizable Poly(phthalaldehyde) Membrane. *Macromolecules* **2013**, 46, 3309-3313.
39. Köstler, S.; Zechner, B.; Trathnigg, B.; Fasl, H.; Kern, W.; Ribitsch, V. Amphiphilic Block Copolymers Containing Thermally Degradable Poly(phthalaldehyde) Blocks. *J. Polym. Sci., Part A: Polym. Chem.* **2009**, 47, 1499-1509.
40. Köstler, S. Polyaldehydes: Homopolymers, Block Copolymers and Promising Applications. *Polym. Int.* **2012**, 61, 1221-1227.
41. Fan, B.; Salazar, R.; Gillies, E. R. Depolymerization of Trityl End-Capped Poly(ethyl glyoxylate): Potential Applications in Smart Packaging. *Macromol. Rapid Commun.* **2018**, 39, 1800173-1800178.

42. Hong, M.; Chen, E. Y.-X. Completely Recyclable Biopolymers with Linear and Cyclic Topologies via Ring-Opening Polymerization of γ-Butyrolactone. *Nat. Chem.* **2016**, 8, 42-49.
43. Zhu, J.-B.; Watson, E. M.; Tang, J.; Chen, E. Y.-X. A Synthetic Polymer System with Repeatable Chemical Recyclability. *Science* **2018**, 360, 398-403.
44. Schwartz, J. M.; Engler, A.; Phillips, O.; Lee, J.; Kohl, P. A. Determination of Ceiling Temperature and Thermodynamic Properties of Low Ceiling Temperature Polyaldehydes. *J. Polym. Sci., Part A: Polym. Chem.* **2017**, 56, 221-228.
45. Schwartz, J. M.; Phillips, O.; Engler, A.; Sutlief, A.; Lee, J.; Kohl, P. A. Stable, High-Molecular-Weight Poly(phthalaldehyde). *J. Polym. Sci., Part A: Polym. Chem.* **2016**, 55, 1166-1172.
46. Feinberg, A. M.; Lopez Hernandez, H.; Plantz, C. L.; Mejia, E. B.; Sottos, N. R.; White, S. R.; Moore, J. S. Cyclic Poly(phthalaldehyde): Thermoforming a Bulk Transient Material. *ACS Macro Lett.* **2018**, 7, 47-52.
47. Aboulkas, A.; El harfi, K.; El Bouadili, A. Thermal Degradation Behaviors of Polyethylene and Polypropylene. Part I: Pyrolysis Kinetics and Mechanisms. *Energy Convers. Manage.* **2010**, 51, 1363-1369.
48. Faravelli, T.; Pinciroli, M.; Pisano, F.; Bozzano, G.; Dente, M.; Ranzi, E. Thermal Degradation of Polystyrene. *J. Anal. Appl. Pyrolysis* **2001**, 60, 103-121.
49. Vilaplana, F.; Ribes-Greus, A.; Karlsson, S. Degradation of Recycled High-Impact Polystyrene. Simulation by Reprocessing and Thermo-Oxidation. *Polym. Degrad. Stab.* **2006**, 91, 2163-2170.
50. Ignatyev, I. A.; Thielemans, W.; Vander Beke, B. Recycling of Polymers: A Review. *ChemSusChem* **2014**, 7, 1579-1593.
51. El Mehdi Mekhzoum, M.; Benzeid, H.; Rodrigue, D.; El Kacem Qaiss, A.; Bouhfid, R. Recent Advances in Polymer Recycling: A Short Review. *Curr. Org. Synth.* **2017**, 14, 171-185.
52. Kumar, A.; Gupta, R. K. *Fundamentals of Polymer Engineering Second Edition*; Marcel Dekker, Inc.: New York, 2003; pp 488-497.
53. Sharma, S. K.; Misra, A. The Effect of Stretching Conditions on Properties of Amorphous Polyethylene Terephthalate Film. *J. Appl. Polym. Sci.* **1987**, 34, 2231-2247.
54. Arrakhiz, F. Z.; El Achaby, M.; Kakou, A. C.; Vaudreuil, S.; Benmoussa, K.; Bouhfid, R.; Fassi-Fehri, O.; Qaiss, A. Mechanical Properties of High Density Polyethylene Reinforced with Chemically Modified Coir Fibers: Impact of Chemical Treatments. *Mater. Des.* **2012**, 37, 379-383.
55. Lim, K. L. K.; Mohd Ishak, Z. A.; Ishiaku, U. S.; Fuad, A. M. Y.; Yusof, A. H.; Czigany, T.; Pukanszky, B.; Ogunniyi, D. S. High-Density Polyethylene/Ultrahigh-Molecular-Weight Polyethylene Blend. I. The Processing, Thermal, and Mechanical Properties. *J. Appl. Polym. Sci.* **2005**, 97, 413-425.
56. Jones, A. R.; Blaiszik, B. J.; White, S. R.; Sottos, N. R. Full Recovery of Fiber/Matrix Interfacial Bond Strength Using a Microencapsulated Solvent-Based Healing System. *Compos. Sci. Technol.* **2013**, 79, 1-7.

Chapter 3: Triggering Transience of Plastics

3.1 Introduction

Synthetic polymers are ubiquitous in our day-to-day lives due to their ease of manufacture[1], wide range of mechanical properties[2], and resistance to corrosion and aging[3]. In contrast to polymer production, plastic waste remediation has proven challenging. Synthetic polymers are largely unrecovered at the end of the material lifespan; notably, less than 10% of plastic waste in the U.S. was recycled in 2015, with the remainder largely being sent to landfills (ca. 75%) or burned (ca. 15%). This lack of end-of-life management has resulted in the global plastic pollution crisis.[4] Transient materials may provide controlled end-of-life strategies for plastic waste mitigation.

The ideal transient material has good mechanical properties, is readily accessible from inexpensive feedstocks, is processable by conventional methods, and is easily tailored to respond to different and orthogonal triggering stimuli. Depolymerization reactions are typically triggered by light[5], acid[6], and specific ions[7], stimuli that are ubiquitous in everyday use. Single electron transfer (SET) triggering of transient polymers presents an alternative route to tunable transient materials. An SET-triggered polymer unzipping reaction offers versatility for materials formulation. Tailored additives would enable SET-triggering from specific light[8], chemical[9,10], or electrical[11] input to initiate depolymerization using a single, easily-accessible pathway. In this work, we sought to demonstrate a transient material that is easily synthesized, has a storage modulus of at least 1 GPa, is processable, and is triggered to depolymerize by SET.

A promising transient polymer is cyclic poly(phthalaldehyde) (cPPA), which has a room temperature storage modulus of 1.5-2 GPa[12] and is prepared in a scalable, one-step cationic polymerization reaction from *ortho*-phthalaldehyde (*o*PA), a readily available monomer[13,14]. cPPA

rapidly unzips to form *o*PA on thermal[15], acid[16], or mechanical[17] triggering due to its low ceiling temperature (T_c = -36 °C[18]). The mechanisms of acid-triggered[19] and mechanically-triggered[17] cPPA unzipping are well known, but the mechanism of thermal triggering has not been established. While purely ionic and purely radical thermolytic depolymerization mechanisms have been previous proposed[20], we hypothesized that SET effectively initiates the unzipping of cPPA by mesolytic cleavage of the radical cation intermediate (**Figure 3.1**). Here, we present evidence in support of the SET-triggered depolymerization of cPPA and demonstrate the application of this mechanism in the manufacture of sunlight-degradable monolithic materials.

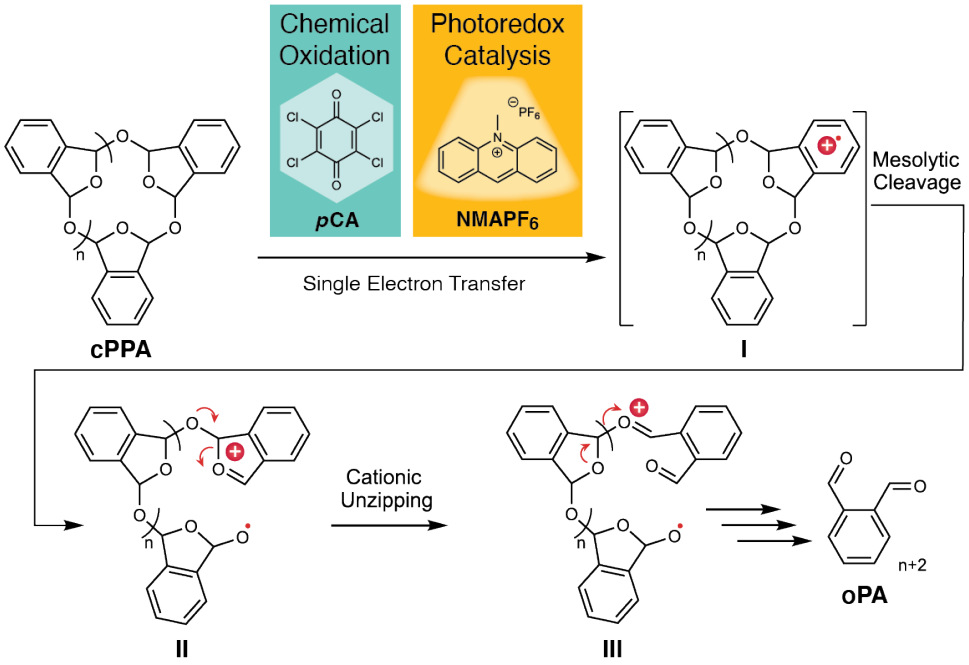

Figure 3.1. Putative single electron transfer (SET) induced depolymerization of cyclic poly(phthalaldehyde) | One electron oxidation of cPPA either via chemical oxidation using *p*-chloranil (*p*CA) or photoredox catalysis using *N*-methylacridinium hexafluorophosphate ($NMAPF_6$) results in the formation of the corresponding cation radical intermediate I. Following SET activation, mesolytic cleavage of I forms the distonic cation radical II, which is hypothesized to undergo cationic unzipping of the activated oxonium chain end, forming intermediate III, and ultimately the monomer *o*PA.

3.2 Single Electron Transfer Induced Depolymerization of cPPA

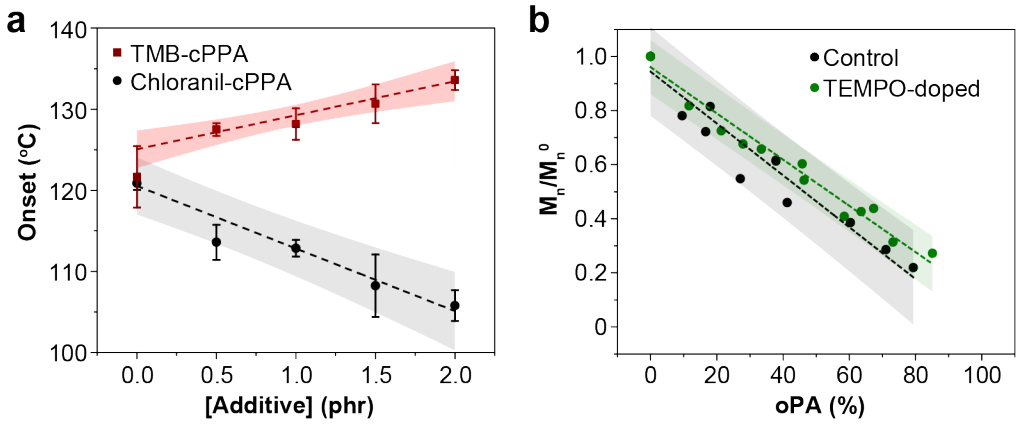

Figure 3.2. Thermolysis of cPPA in the presence of reductants and oxidants | (a) Change in degradation onset temperature during 5 °C/min dynamic TGA scans of cPPA thin films as a function of 1,3,5-trimethoxybenzene (TMB) and *p*-chloranil concentration, phr = parts per hundred resin. (b) Evolution of molecular weight (M_n) as a function of conversion during thermolysis of cPPA thin films containing 2 phr TEMPO. In each plot, error bands and error bars represent 95% confidence. Plotted points in (a) represent the average of three measurements.

We hypothesized that, during thermolysis, SET oxidation of cPPA leads to the formation of a benzylic cation radical[21]. Mesolytic fragmentation of the benzylic cation radical[22,23] is followed by subsequent cationic chain unzipping throughout the polymer chain (**Figure 3.1**). To test the SET-triggering hypothesis, we first examined the effect of a small molecule oxidant, *p*-chloranil (pCA, E_{red} = -0.005 V vs SCE in acetonitrile[24])**,** on cPPA thermal stability (**Figure 3.2a**). If SET triggers cPPA depolymerization, addition of an oxidant is expected to destabilize the polymer. The addition of pCA resulted in significantly reduced thermal stability, which decreased in a dose-dependent manner. This linear dependence enabled tuning of the thermal degradation onset temperatures over a ca. 15 °C range (0-2 phr (parts per hundred resin) pCA). These results demonstrate that SET is an effective method for triggering cPPA degradation, but do not indicate whether the SET triggering mechanism is operative under typical thermolytic conditions, as SET requires a reductant/oxidant pair. A plausible thermo-oxidant is BF_3-pyridine, known to be both a mild oxidant[25] and a common impurity in cPPA which results in lowered polymer thermal stability[20].

Though it is not possible to determine if the BF_3-pyridine in cPPA is the operative oxidant, we can conclusively establish whether SET is the primary mode of thermolytic cPPA depolymerization. This SET triggering mechanism further predicts that electron donors, such as 1,3,5-trimethoxybenzene (TMB, E_{ox} = 1.539 V vs SCE)[26], will inhibit the thermal degradation of cPPA. As shown in **Figure 3.2a**, addition of TMB to cPPA films results in a material with a higher degradation onset temperature. The onset of polymer degradation measured during dynamic TGA experiments varied linearly with TMB concentration. GPC analysis of the cPPA films during thermolysis in the presence and absence TMB show no significant differences in M_n evolution in doped and undoped samples. This result indicates that the inhibitory action of TMB occurs *before* the activation of cPPA chains, consistent with the SET triggering mechanism and inconsistent with purely radical or purely ionic thermolysis mechanisms.

The addition of TEMPO to cPPA is known to stabilize the polymer toward thermolysis.[20] This effect had previously been rationalized by trapping of radical chain ends by TEMPO. In contrast, the SET triggering hypothesis predicts that TEMPO inhibition is due to sacrificial oxidation of TEMPO (E_{ox} = 0.50 V vs SCE[27]). To probe the nature of TEMPO inhibition, we monitored by GPC the evolution of polymer molecular weight during the thermolytic depolymerization of cPPA films in the presence and absence of added TEMPO. If the stabilizing effect of TEMPO was due to radical trapping, i.e. the deactivation of reactive cPPA termini after a scission event, the change in M_n during depolymerization would follow a non-linear trend[28], generating low molecular weight chains at low conversion. Instead, M_n of cPPA samples without TEMPO and with 2 phr added TEMPO followed statistically similar linear trends during depolymerization, with no observable low M_n species at low conversion (**Figure 3.2b**). This trend indicates that the stabilizing effect of TEMPO is not due to radical trapping, but rather suggests that TEMPO inhibits SET-*activation* of

the polymer chain. These results exclude a homolytic thermal depolymerization mechanism and further support the SET-triggering hypothesis. Having established a novel SET triggering mechanism as the primary thermal depolymerization pathway for cPPA, we were interested in the application of SET chemistry to develop photodegradable monolithic materials using photoinduced single electron transfer.

3.3 Mechanical Deterioration during Photo-Oxidative Depolymerization of cPPA

While photodegradable thin films have been demonstrated previously by the creative application of photoacid generators (PAGS)[6,29], the thermal decomposition of PAGs precludes their use in the manufacture of monolithic photodegradable materials[30,31], which generally requires extended time at elevated temperature for melt processing. Thermally stable organic photooxidants present a promising tool for the manufacture of monolithic, photodegradable engineering plastics. Bulk material samples were fabricated following our previously reported procedure[20]. Briefly, cPPA was solvent-blended in dichloromethane with a plasticizer (diphenylphthalate, 40-60 phr) and a photooxidant ($NMAPF_6$, 1 mol %) and drop cast in a dark enclosure to exclude ambient light. After 24 hours, the blended films were pulverized, and the resultant powder was used as a feedstock for thermoforming. Type V dog-bone samples (ASTM standard D638) were fabricated by hot-pressing the cPPA-$NMAPF_6$-DPP feedstock at 90 °C, 10 MPa for 5 minutes. The resultant monolithic materials were high-quality, optically transparent thermoplastics with an average storage modulus of 1.8 GPa, as measured by dynamic mechanical analysis (DMA).

To study photooxidative depolymerization of bulk polymers, the mechanical integrity of cPPA samples (thickness = 500 μm) was measured by DMA during exposure to UV light. Optical images of a cPPA-$NMAPF_6$-DPP sample during UV irradiation at 0.35 Wcm^{-2} in the DMA instrument are shown in **Figure 3.3a-c**. The bulk material completely degrades in the irradiated area, resulting in

a viscous liquid composed of monomer, plasticizer, and the photooxidant by-products. Unexposed and under-exposed regions remained visibly unaffected. As shown in **Figure 3.3d** the rate of material degradation is controlled by irradiation intensity. Bulk samples were monitored in the dark for a 300 second pre-exposure period to obtain a baseline stiffness, at which point the UV light source (375 nm) was turned on. Samples exposed to 0.1, 0.15, and 0.2 Wcm^{-2} UV irradiation rapidly lost mechanical integrity, failing under tension within 600, 300, and 200 seconds, respectively. Samples that were not exposed to UV light maintained their original stiffness throughout the experiment. Control samples without $NMAPF_6$ did not undergo significant change on exposure to equivalent UV irradiation.

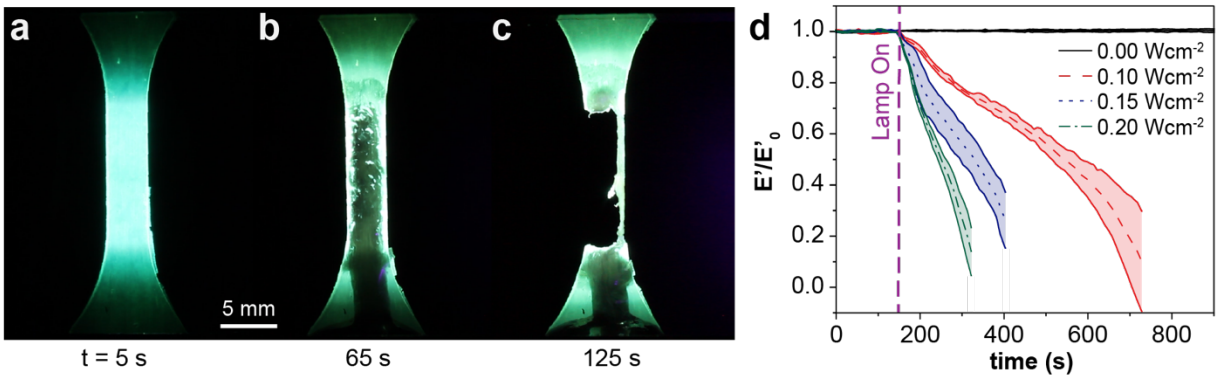

Figure 3.3. Controlled depolymerization of bulk cPPA samples by photochemical SET triggering | (a-c) Photographs of a cPPA-$NMAPF_6$ dog bone under 375 nm radiation (0.35 Wcm^{-2}) at 5, 65, and 125 s, showing physical destruction of the polymer matrix. (d) Normalized E' of $NMAPF_6$-doped cPPA dog bones during photolysis at 375 nm at varying light intensities. Samples were monitored in the absence of light for 150 s, at which point the lamp was turned on. Each curve is an average of 3 samples, and error bands represent 95% confidence.

3.4 Sunlight Degradation of Monolithic Solids

Finally, the efficacy of SET-triggering for applications in environmental degradation was tested. Using the above thermoforming procedure, an I-shaped monolithic solid was manufactured (thickness = 2.0 mm). The sample was exposed to solar radiation (measured light intensity = 30 $mWcm^{-2}$) and photographed at regular intervals (**Figure 3.4a-e**) on a white cardstock background. After 3 minutes of exposure to sunlight, the sample discolored along its surface. Within 6 minutes,

viscous liquid had begun to pool around the sample. After 12 minutes of exposure, large, needle-like crystals appeared, indicating the formation of the crystalline monomer, *o*PA. Within 24 minutes of sunlight exposure, no visible polymer remained. By using the novel SET triggering mechanism, we have successfully produced a sunlight-degradable monolithic material.

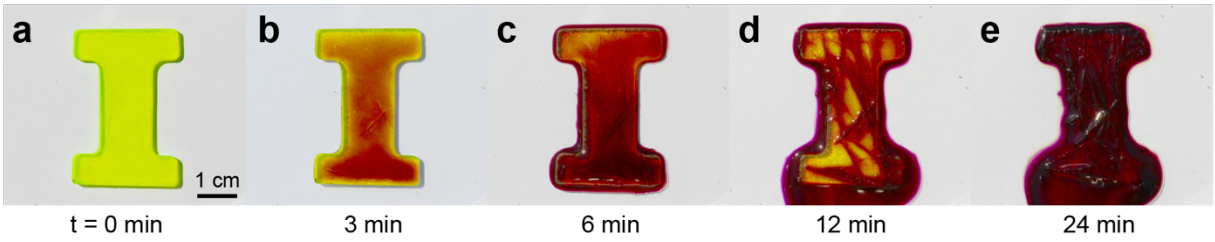

Figure 3.4. Sunlight degradation of cPPA plastics | (a-e) Bulk cPPA-NMAPF$_6$ degrading in sunlight on a sunny day in August in Champaign, IL, US, over the span of 25 minutes. UV intensity during sunlight photodegradation was measured at 30 mWcm^{-2}, and the outdoor temperature was 24.5 °C.

3.5 Conclusions

We have presented for the first time a transient polymer which undergoes rapid chain unzipping depolymerization to its constituent monomer following a single electron transfer trigger. SET triggering is achieved through multiple modes and was realized in both thermal and photochemical depolymerization of cyclic poly(phthalaldehyde). The collection of evidence presented here supports the mechanistic hypothesis of SET activation and subsequent mesolytic cleavage. This mechanism was used to tune the thermal stability of cPPA by the addition of oxidants and reductants. Additionally, photooxidation of cPPA using NMAPF$_6$ was demonstrated as an effective method of depolymerization in solution and in thin films. Finally, monolithic solids comprised of cPPA, diphenylphthalate, and NMAPF$_6$ were fabricated. These photooxidant-doped bulk solids were shown to exhibit desirable mechanical properties (E' = 1.8 GPa), and to respond rapidly to applied UV light, degrading completely into the corresponding monomer. Additionally, it was shown that the monolithic cPPA materials fully degraded to monomer within 25 minutes of sunlight exposure.

Given the ease with which cPPA depolymerizes by frequently encountered stimuli, it is unlikely to serve as a candidate to mitigate the environmental burden of single use plastics. Nonetheless, as a bulk engineering plastic that rapidly depolymerizes via photoredox catalysis, the chemical concepts presented here may inspire the development of new transient packaging. Even in its present state the applications for cPPA are evident, such as in the manufacture of transient delivery systems, and environmental sensing applications. For examples, it is conceivable that SET-triggered cPPA is well-suited for use in the manufacture of air gliding vehicles that deliver critical supplies and subsequently vanish by programmable transience, leaving no trace of the device. Most importantly, this work demonstrates a novel mode of SET-triggered transience and raises the prospect of SET as a depolymerization mechanism in a potentially broad range of polymers. Thus, SET triggering of transient polymers is viewed as a promising area for future exploration.

3.6 Future Work

The availability of orthogonal triggering mechanisms is of critical importance to the design of sustainable materials as a balance between stability in service life and recyclability at the end of life must be struck. SET triggered depolymerization can be tailored to be completely orthogonal to the polymer service life, and the exploration of SET triggering in thermally stable transient plastics, such as poly(benzyl ether)s[32] and poly(4,5-dichlorophthalaldehyde)[33], will effectively demonstrate that this balance is attainable. Further, addition of inert fillers, such as carbon nanofibers,[34] will enable electron transduction in bulk materials and the development of electrically degradable devices. Additionally, through the incorporation of piezoelectric particles[35], mechanical activation will be possible in the solid state, representing a significant step in the realization of bioinspired bone remodeling in synthetic materials. Finally, SET triggered

depolymerization presents an avenue towards enzymatic degradation of plastic waste. P450 enzymes have been found to promote oxidation of aromatic small molecules to radical cations[36], and are anticipated to support SET initiated depolymerization of transient polymers.

3.7 Experimental Details

3.7.1 General

All materials were purchased from Sigma-Aldrich and used without further purification unless otherwise noted. *Ortho*-Phthalaldehyde (*o*PA) was purchased from Oakwood Chemical and purified via vacuum distillation (0.1 torr, 90 °C). Poly(tetrafluoroethylene) petri dish liners were purchased from Welch Fluorocarbon Inc. Ultra-high-molecular-weight polyethylene substrates were purchased from McMaster Carr. All prepared thin films were stored at -20 °C until use.

Analytical Gel Permeation Chromatography (GPC) was performed using a Waters 1515 isocratic HPLC pump and Waters 2707 96-well autosampler, equipped with a Waters 2414 refractive index detector and 4 Waters HR Styragel Column (7.8 × 300 mm, HR1, HR3, HR4, and HR5) in THF at 30 °C. The GPC system was calibrated using monodisperse polystyrene standards.

Thermogravimetric analysis (TGA) was performed using a TA Instruments Q500 TGA under a nitrogen atmosphere (90 mL/min). Dynamic TGA traces were obtained during a 5 °C/min ramp after equilibration at 40 °C. TGA samples consisted of 3-5 mg of the analyte film in a platinum pan. ^{1}H NMR spectra were recorded on a Varian VXR 500 (500 MHz) or an NMReady-60 benchtop NMR (60 MHz) purchased from Nanalysis Scientific Corp. UV photodepolymerization was performed using a custom-made 375 nm LED equipped with an AR coated aspherical condenser lens and an AR coated biconvex focusing lens (75 mm focal length). All parts were purchased from Thor Labs and assembled manually. A Keyence VHX-5000 series digital microscope was used to visualize photodegradation of cPPA thin films. A Canon EOS 7D camera

equipped with a 100 mm macro lens from Canon was used to image photodegradation of cPPA bulk materials.

3.7.2 Synthesis of Cyclic Poly(Phthalaldehyde)

Cyclic poly(phthalaldehyde) (cPPA) was prepared via the cationic polymerization of purified *o*PA using a Lewis acid catalyst, BF_3-EtO_2, according to a known procedure.[14] All reactions were run in anhydrous dichloromethane at -78 °C. Briefly, 40 g of *ortho*-phthalaldehyde (300 mmol) was dissolved in 200 mL of anhydrous DCM (1.5 M). The solution was first cooled down to -78 °C for 2 minutes upon which 0.8 mL of BF_3-EtO_2 (6.5 mmol) was added to the reaction. The solution was stirred using a mechanical stirrer for 2 hours, at which point it had become highly viscous. The reaction was then quenched using 2 mL of pyridine and was stirred for an additional 2 hours. Finally, the reaction mixture was precipitated in 4 L of methanol. The precipitated polymer was dried via vacuum filtration for 1 hour and subsequently dried on hi-vac overnight to afford 36.5 g (92%) of a white solid. The polymer was stored at -20 °C until use.

^{1}H NMR (CD_2Cl_2, 500 MHz) δ 5.75-7.75 (br, 6 H). M_n = 250 kDa, Đ = 1.67.

3.7.3 Synthesis of *N*-Methylacridinium Iodide

N-methylacridinium iodide (NMAI) was synthesized according to literature procedure.[37] Briefly, a 100 mL oven dried round bottom flask was charged with a stir bar. 5.0 g of acridine (27.6 mmol) was dissolved in 20 mL DMF and was heated to 35 °C for 10 minutes. 3.4 mL iodomethane (55 mmol) was added into the reaction flask. The reaction flask was heated to 50 °C overnight under dry nitrogen. 100 mL of diethyl ether was added to the reaction mixture, and the precipitated solid was then isolated via vacuum filtration. The compound was dried on hi-vac overnight to yield 6.6 g of material (74%) and was used without further purification.

^{1}H NMR (CD_2Cl_2, 500 MHz) δ 10.02 (s, 0.95 H), 8.67 (d, 2 H), 8.61 (dd, 1.96 H), 8.47 (ddd, 1.99 H), 8.02 (ddd, 1.97 H), 5.00 (s, 3.16 H).

3.7.4 Synthesis of *N*-Methylacridinium Hexafluorophosphate

1.09 g of NMAI (3.3 mmol) was dissolved in 120 mL of water and a 20 mL aqueous potassium hexafluorophosphate (1.22 g, 6.6 mmol) solution was added. A yellow precipitate formed immediately. The solution was stirred for 30 minutes and the precipitate was isolated via vacuum filtration. The precipitate was washed with 3×50 mL water and was then dried under vacuum overnight. The dried product purified via recrystallization in methanol, forming small needle-like crystals (253 mg, 28.6 % yield). The resulting compound was dried under vacuum and stored away from light.

^{1}H NMR (CD_2Cl_2, 500 MHz) δ 9.77 (s, 0.98 H), 8.52 (ddd, 3.95 H), 8.45 (m, 1.99 H), 8.02 (ddd, 1.95 H), 4.87 (s, 3.13 H).

3.7.5 Solvent cPPA Thin Films

Free standing pristine cPPA thin films were prepared according to literature procedure.[20] Briefly, cPPA (100 mg) was dissolved in HPLC grade dichloromethane (3 mL). The solution was then cast into a 50 mm diameter PTFE-lined petri dish and allowed to dry for 24 hours in a light-free cardboard enclosure with solvent-saturated atmosphere. Films used in reductant and oxidant stability tests were doped with 0.5, 1.0, 1.5 and 2.0 mg of 1,3,5-trimethoxybenzene (TMB) or *p*-chloranil (*p*CA) before casting. Films used in trapping experiments were doped with 2.0 mg TEMPO or TMB before casting.

3.7.6 cPPA Trapping Experiments

Small sections of cPPA thin films were cut and weighed out (~5 mg). The films were placed into the bottom of scintillation vials. The vials were then immersed in an oil bath that was kept at

100 °C. The vials were removed at 5-minute intervals and the depolymerization quenched using an ice bath. The vial contents were dissolved in 0.25 ml of THF and analyzed by GPC. The GPC traces were normalized by the initial mass of the film, and conversion was determined via the ratio of the normalized area of high molecular weight peaks (retention times between 20-35 minutes) of samples subjected to thermolysis and a control sample that was not subjected to thermolysis.

The trends of M_n vs. conversion for samples doped with TMB and with TEMPO were compared against those of pristine cPPA films run at the same time using an F-test. The trends were not found to be statistically different at the 95 percent confidence level.

3.7.7 Fabrication of cPPA Monoliths

cPPA Feedstock Preparation

5.0 g of cPPA and diphenylphthalate (2.0 or 3.0 g for dog-bone feedstock and I-shaped monolith feedstock, respectively) were dissolved in HPLC grade dichloromethane (40 mL). To prepare the photooxidant-doped feedstock 127 mg (1 mol % with respect to *o*PA repeat unit) $NMAPF_6$ was added to the solution. Solutions were then tape cast onto an ultra-high-molecular-weight polyethylene substrate in the dark. Film thickness (200 μm) was set with a high precision film applicator. Films were left in a dichloromethane-saturated environment for 24 h. This process generated a free-standing film which was then pulverized into a powder feedstock using a coffee grinder.

cPPA Monolith Preparation

300 mg of cPPA feedstock prepared above (with or without added $NMAPF_6$) were placed into an aluminum dogbone mold (ASTM Standard D638 Type V). The filled mold was then preheated at 90 °C for 5 minutes. Samples were then pressed at 10 MPa and 90 °C for 5 minutes. The mold was cooled down (10 °C/min) to room temperature, and the dog-bones (500 μm thick) were

removed from the mold. The same process was used to produce the "I" shaped monoliths using 1.5 g of cPPA feedstock.

Storage Modulus Determination

Dynamic mechanical analysis (DMA) was performed using a TA Instruments RSA III. Both pristine cPPA and $NMAPF_6$-doped cPPA samples were loaded onto the DMA using thin film grips provided by TA Instruments. The gauge length was set to 8 mm. Oscillatory load was applied at 10 Hz and 0.1 % strain amplitude at 20 °C. The storage modulus of three samples was measured for both pristine cPPA samples and $NMAPF_6$-doped samples. The average storage moduli of pristine and $NMAPF_6$-doped samples were 1.54 ± 0.10 and 1.78 ± 0.11 GPa, respectively.

3.7.8 Dynamic Mechanical Analysis of cPPA during Photodegradation

Pristine cPPA and $NMAPF_6$-doped cPPA specimens were loaded onto the DMA, and the gauge length was set to 25 mm. Oscillatory loading was applied at 10 Hz and 0.1 % strain amplitude at 20 °C. The samples were first characterized in the dark for a 300 second pre-exposure period after which the UV light source (0.1, 0.15, or 0.2 Wcm^{-2}) was turned on. Specimens were tested until they failed in tension. Degradation was monitored optically with a Canon EOS 7D camera equipped with a 100 mm macro lens.

3.7.9 Sunlight Depolymerization of cPPA Monoliths

"I" shaped cPPA monoliths prepared above were placed on a glass petri dish and placed outside on a sunny day, September 6th, 2019 in Urbana, Illinois. Photographs of the specimens were taken at 5 second intervals for 25 minutes. The UV intensity during sunlight photodegradation was measured to be 30 $mWcm^{-2}$, and the outdoor temperature was 30.5 °C. The $NMAPF_6$-doped cPPA sample showed complete degradation after 24 minutes of exposure whereas the pristine cPPA sample showed no visual signs of degradation.

3.8 Notes and References

3.8.1 Notes

This is a collaborative effort with multiple contributors. E.M.L prepared bulk monoliths, performed the dynamic mechanical analysis experiments, and conducted the sunlight degradation experiments. Oleg Davydovich performed all syntheses and conducted the thermal gravimetric analysis, gel permeation chromatography, and NMR experiments. Douglas Ivanoff aided in sample imaging. Elizabeth Feinberg directed the research. Elizabeth Feinberg, Oleg Davydovich, and E.M.L authored the text.

Portions of this chapter have been published. Feinberg, E. C.; Davydovich, O.; Lloyd, E. M.; Ivanoff, D. G.; Shiang, B.; Sottos, N. R.; Moore, J. S. "Triggered Transience of Plastic Materials by a Single Electron Transfer Mechanism" *ACS Cent. Sci.* **2020**, 6, 266-273. They are reproduced/adapted with permission. Copyright 2020 American Chemical Society.

3.8.2 References

1. Brian, N. T. A Review of Melt Extrusion Additive Manufacturing Processes: I. Process Design and Modeling. *Rapid Prototyp. J.* **2014**, 20, 192-204.
2. Marsavina, L.; Cernescu, A.; Linul, E.; Scurtu, D.; Chrita, C. Experimental Determination and Comparison of Some Mechanical Properties of Commercial Polymers. *Mater. Plast.* **2010**, *47*, 45-89.
3. Kondo, H.; Tanaka, T.; Masuda, T.; Nakajima, A. Aging Effects in 16 Years on Mechanical Properties of Commercial Polymers (Technical Report). *Pure and Applied Chemistry*. 1992, p. 1945.
4. Eriksen, M.; Lebreton, L. C. M.; Carson, H. S.; Thiel, M.; Moore, C. J.; Borerro, J. C.; Galgani, F.; Ryan, P. G.; Reisser, J. Plastic Pollution in the World's Oceans: More than 5 Trillion Plastic Pieces Weighing over 250,000 Tons Afloat at Sea. *PLoS One* **2014**, 9, e111913.
5. Joo, W.; Wang, W.; Mesch, R.; Matsuzawa, K.; Liu, D.; Wilson, C. G. Synthesis of Unzipping Polyester and a Study of Its Photochemistry. *J. Am. Chem. Soc.* **2019**, 141, 14736-14741.
6. Lopez Hernandez, H.; Kang, S.-K.; Lee, O. P.; Hwang, S.-W.; Kaitz, J. A.; Inci, B.; Park, C. W.; Chung, S.; Sottos, N. R.; Moore, J. S.; Rogers, J. A.; White, S. R. Triggered Transience of Metastable Poly(Phthalaldehyde) for Transient Electronics. *Adv. Mater.* **2014**, 26, 7637-7642.
7. Sagi, A.; Weinstain, R.; Karton, N.; Shabat, D. Self-Immolative Polymers. *J. Am. Chem. Soc.* **2008**, 130, 5434-5435.
8. Romero, N. A.; Nicewicz, D. A. Organic Photoredox Catalysis. *Chem. Rev.* **2016**, 116, 10075-10166.
9. Zhang, N.; Samanta, S. R.; Rosen, B. M.; Percec, V. Single Electron Transfer in Radical Ion and Radical-Mediated Organic, Materials and Polymer Synthesis. *Chem. Rev.* **2014**, 114, 5848-5958.
10. Pross, A. The Single Electron Shift as a Fundamental Process in Organic Chemistry: The Relationship between Polar and Electron-Transfer Pathways. *Acc. Chem. Res.* **1985**, 18, 212-219.
11. Weinberg, N. L.; Weinberg, H. R. Electrochemical Oxidation of Organic Compounds. *Chem. Rev.* **1968**, 68, 449-523.

12. Lopez Hernandez, H.; Tekekuma, S. K.; Mejia, E. B.; Plantz, C. L.; Sottos, N. R.; Moore, J. S.; White, S. R. Processing Dependent Mechanical Properties of Solvent Cast Cyclic Polyphthalaldehyde. *Polymer*, **2019**, 162, 29-34.
13. Schwartz, J. M.; Phillips, O.; Engler, A.; Sutlief, A.; Lee, J.; Kohl, P. A. Stable, High-Molecular-Weight Poly(Phthalaldehyde). *J. Polym. Sci. Part A Polym. Chem.* **2017**, 55, 1166-1172.
14. Kaitz, J. A.; Diesendruck, C. E.; Moore, J. S. End Group Characterization of Poly(Phthalaldehyde): Surprising Discovery of a Reversible, Cationic Macrocyclization Mechanism. *J. Am. Chem. Soc.* **2013**, 135, 12755-12761.
15. Lloyd, E. M.; Lopez Hernandez, H.; Feinberg, A. M.; Yourdkhani, M.; Zen, E. K.; Mejia, E. B.; Sottos, N. R.; Moore, J. S.; White, S. R. Fully Recyclable Metastable Polymers and Composites. *Chem. Mater.* **2019**, 31, 398-406.
16. Park, C. W.; Kang, S.-K.; Lopez Hernandez, H.; Kaitz, J. A.; Wie, D. S.; Shin, J.; Lee, O. P.; Sottos, N. R.; Moore, J. S.; Rogers, J. A.; White, S. R. Thermally Triggered Degradation of Transient Electronic Devices. *Adv. Mater.* **2015**, 27, 3783-3788.
17. Diesendruck, C. E.; Peterson, G. I.; Kulik, H. J.; Kaitz, J. A.; Mar, B. D.; May, P. A.; White, S. R.; Martínez, T. J.; Boydston, A. J.; Moore, J. S. Mechanically Triggered Heterolytic Unzipping of a Low-Ceiling-Temperature Polymer. *Nat. Chem.* **2014**, 6, 623-628.
18. Lutz, J. P.; Davydovich, O.; Hannigan, M. D.; Moore, J. S.; Zimmerman, P. M.; McNeil, A. J. Functionalized Degradable Polyphthalaldehyde Derivatives. *J. Am. Chem. Soc.* **2019**, 141, 14544-14548.
19. Tsuda, M.; Hata, M.; Nishida, R.; Oikawa, S. Acid-Catalyzed Degradation Mechanism of Poly(Phthalaldehyde): Unzipping Reaction of Chemical Amplification Resist. *J. Polym. Sci. Part A Polym. Chem.* **1997**, 35, 77-89.
20. Feinberg, A. M.; Hernandez, H. L.; Plantz, C. L.; Mejia, E. B.; Sottos, N. R.; White, S. R.; Moore, J. S. Cyclic Poly(Phthalaldehyde): Thermoforming a Bulk Transient Material. *ACS Macro Lett.* **2018**, 7, 47-52.
21. Boyd, J. W.; Schmalzl, P. W.; Miller, L. L. Mechanism of Anodic Cleavage of Benzyl Ethers. *J. Am. Chem. Soc.* **1980**, 102, 3856-3862.
22. Rathore, R.; Kochi, J. K. Radical-Cation Catalysis in the Synthesis of Diphenylmethanes via the Dealkylative Coupling of Benzylic Ethers. *J. Org. Chem.* **1995**, 60, 7479-7490.
23. Carlotti, B.; Del Giacco, T.; Elisei, F. Competition of C–H and C–O Fragmentation in Substituted *p*-Methoxybenzyl Ether Radical Cations Generated by Photosensitized Oxidation. *Photochem. Photobiol. Sci.* **2013**, 12, 489-499.
24. Sasaki, K.; Kashimura, T.; Ohura, M.; Ohsaki, Y.; Ohta, N. Solvent Effect in the Electrochemical Reduction of *p*-Quinones in Several Aprotic Solvents. *J. Electrochem. Soc.* **1990**, 137, 2437-2443.
25. Chénard, E.; Sutrisno, A.; Zhu, L.; Assary, R. S.; Kowalski, J. A.; Barton, J. L.; Bertke, J. A.; Gray, D. L.; Brushett, F. R.; Curtiss, L. A.; Moore, J. S. Synthesis of Pyridine– and Pyrazine–BF_3 Complexes and Their Characterization in Solution and Solid State. *J. Phys. Chem. C* **2016**, 120, 8461-8471.
26. Luo, P.; Feinberg, A. M.; Guirado, G.; Farid, S.; Dinnocenzo, J. P. Accurate Oxidation Potentials of 40 Benzene and Biphenyl Derivatives with Heteroatom Substituents. *J. Org. Chem.* **2014**, 79, 9297-9304.
27. Israeli, A.; Patt, M.; Oron, M.; Samuni, A.; Kohen, R.; Goldstein, S. Kinetics and Mechanism of the Comproportionation Reaction between Oxoammonium Cation Hydroxylamine Derived from Cyclic Nitroxides. *Free Radic. Biol. Med.* **2005**, 38, 317-324.
28. Carothers, W. H. Polymers and Polyfunctionality. *Trans. Faraday Soc.* **1936**, 32, 39-49.
29. Jiang, J.; Phillips, O.; Engler, A.; Vong, M. H.; Kohl, P. A. Photodegradable Transient Bilayered Poly(Phthalaldehyde) with Improved Shelf Life. *Polym. Adv. Technol.* **2019**, 30, 1198-1204.
30. Spencer, T. J.; Kohl, P. A. Decomposition of Poly(Propylene Carbonate) with UV Sensitive Iodonium Salts. *Polym. Degrad. Stab.* **2011**, 96, 686-702.
31. Yamato, H.; Asakura, T.; Matsumoto, A.; Ohwa, M. Novel Photoacid Generators for Chemically Amplified Resists. In *Proc.SPIE*; 2002; Vol. 4690.
32. Olah, M. G.; Robbins, J. S.; Baker, M. S;. Phillips, S. T. End-Capped Poly(Benzyl Ethers): Acid and Base Stable Polymers that Depolymerize Rapidly from Head-to-Tail in Response to Specific Applied Signals. *Macromolecules* **2013**, 46, 5924–5928.
33. DiLauro, A. M.; Phillips, S. T. End-Capped Poly(4,5-Dichlorophthalaldehyde): A Stable Self-Immolative Poly(Aldehyde) for Translating Specific Inputs into Amplified Outputs, Both in Solution and the Solid State. *Polym. Chem.* **2015**, 6, 3252–3258.
34. Yang, Y.; Gupta, M. C.; Dudley, K. L.; Lawrence, R. W. Conductive Carbon Nanofiber–Polymer Foam Structures. *Adv. Mater.* **2005**, 17, 1999–2003

35. Mohapatra, H.; Ayarza, J.; Sanders, E. C.; Scheuermann, A. M.; Griffin, P. J.; Esser-Kahn, A. P. Ultrasound Promoted Step-Growth Polymerization and Polymer Crosslinking via Copper Catalyzed Azide–Alkyne "Click" Reaction. *Angew. Chem., Int. Ed.* **2018**, 57, 11208–11212.
36. Sato, H.; Guengerich, F. P. Oxidation of 1,2,4,5-Tetramethoxybenzene to a Cation Radical by Cytochrome P450. *J. Am. Chem. Soc.* **2000**, 122, 8099–8100.
37. Eberhard, J.; Peuntinger, K.; Fröhlich, R.; Guldi, D. M.; Mattay, J. Synthesis and Properties of Acridine and Acridinium Dye Functionalized Bis(Terpyridine) Ruthenium(II) Complexes. *European J. Org. Chem.* **2018**, 2018, 2682-2700.

Chapter 4: Energy-Efficient Synthesis and Upcycling of Degradable Thermosets

4.1 Introduction

Since the invention of the first electricity-generating wind turbine in 1888, the design of turbine blades has evolved to center on fiber-reinforced polymer composites (FRPCs).[1] The high specific stiffness, high specific strength, and physical and chemical resilience of FRPCs enable long service lives coupled with exceptional performance and efficiency.[2] While wind energy will ultimately reduce our reliance on fossil fuels and help to minimize our carbon footprint, the use of FRPCs in turbine blades poses two significant environmental challenges. First, the initial manufacture of FRPCs is extremely energy intensive. The thermoset resins frequently employed in the glass FRPCs of wind turbine blades must be cured under pressure and at elevated temperatures for several hours.[3] Second, these FRPCs lack end-of-life strategies as the chemical and thermal stability of the high-strength covalent networks formed during thermoset curing make degradation and recycling impractical.[4] Unfortunately, the turbine blades of the first-generation, large-scale wind farms are reaching the end of their useful lifespans. Thousands of turbine blades are being removed from service annually. It is estimated that eight thousand blades will be decommissioned annually for the next few years in the United States alone[5], with similar trends across the world. Currently, these massive structures, which often exceed 30 m in length and can weigh more than 12,000 kg[6], are being sectioned for transportation and buried in landfills, where they represent significant economic losses and environmental concerns. To alleviate these issues and further reduce the environmental impact of clean energy sources, the next generation of thermoset materials must be manufactured with as little energy as possible and include end-of-life strategies.

Frontal polymerization (FP), which harnesses the latent chemical energy stored within a resin to drive materials synthesis,[7] has been shown to reduce both the manufacturing time and energy

for thermosets and FRPCs by several orders of magnitude[8]. To date, the majority of resin development has centered on acrylates[9–15], epoxies[16–20], and strained cyclic olefins[8,21–26], all of which lack degradable functionality and fail to address the end of life of polymeric materials. Recently, several monomers for ring-opening metathesis polymerization (ROMP) which install cleavable units into the polymer backbone have been explored.[27–30] Moatsou and coworkers utilized monosubstituted dioxepins as localized spacers in multiblock poly(norbornenes).[27] The acid-labile acetal group from the dioxepin monomer enabled precise scission of the spacer and the release of poly(norbornene) blocks. Utilizing an analogous approach, Shieh and coworkers copolymerized cyclic silyl ethers with norbornene derivatives to create cleavable linear, bottlebrush and star copolymers.[28] Shieh's cyclic silyl ethers were also incorporated into poly(dicyclopentadiene) (pDCPD) thermosets.[29] By installing the cleavable unit into the backbone of the thermoset rather than the crosslinks, Shieh and coworkers were able to fully degrade pDCPD thermosets at relatively low loadings of cyclic silyl ether (< 10 vol %).

Inspired by recent advances in FP and degradable ROMP polymers, we seek to combine the two concepts to generate degradable thermosets in an energy efficient manner. Cleavable units will be incorporated into a pDCPD backbone by copolymerizing cyclic silyl ethers and cyclic acetals during the frontal ring-opening metathesis polymerization (FROMP) of dicyclopentadiene (DCPD) (**Figure 4.1a,b**). Hydrolysis of the cleavable units will generate oligomers with a high concentration of olefins and terminal hydroxyl groups which will be leveraged for recycling and upcycling (**Figure 4.1c**). Comonomer performance will be evaluated on three criteria: synthesizability, copolymerization during FROMP, and degradability.

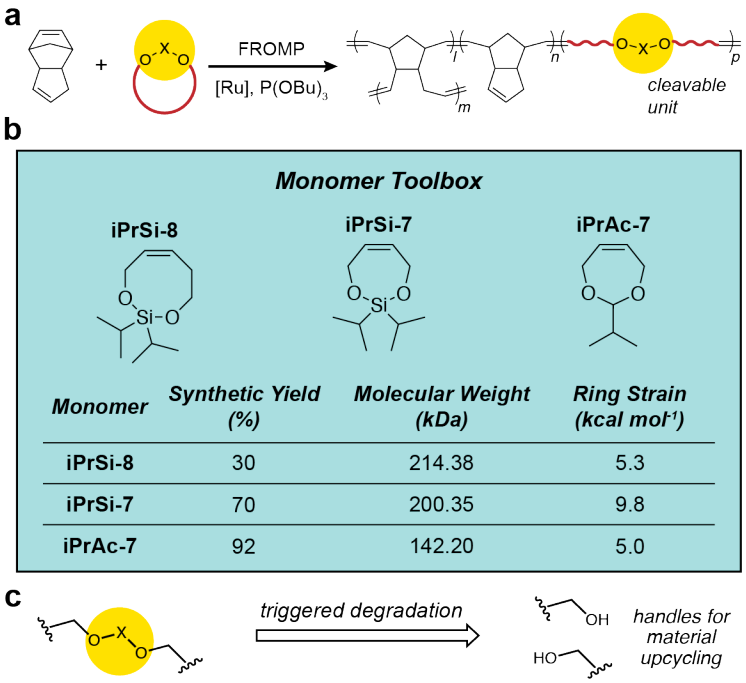

Monomer	Synthetic Yield (%)	Molecular Weight (kDa)	Ring Strain (kcal mol⁻¹)
iPrSi-8	30	214.38	5.3
iPrSi-7	70	200.35	9.8
iPrAc-7	92	142.20	5.0

Figure 4.1. Design of cleavable comonomers for FROMP | a, Frontal copolymerization of DCPD and a cleavable cyclic olefin in the presence of a ruthenium catalyst and tributyl phosphite inhibitor. The chemical unit highlighted in yellow is easily hydrolyzed in the presence of fluoride (X = Si) or acid (X = C). b, Schematic representation and several key properties of candidate olefins. Ring strains are estimated via DFT calculations. c, Triggered degradation of O-X-O unit within thermosets yields hydroxyl units which are leveraged for recycling or upcycling.

4.2 Synthesizability of Cleavable Cyclic Olefins

To be competitive with commodity thermoset resins, all components must be made easily and cheaply at scale. Eight-membered cyclic silyl ethers (e.g. iPrSi-8) are synthesized from *cis*-2-pentene-1,5-diol, which is not commercially available and synthesized over four steps from 3-butynol[28]. Multistep syntheses significantly reduce overall yield (30% overall yield observed for iPrSi-8) and greatly increase manufacturing time, energy, and waste. Conversely, seven-membered cyclic silyl ethers (e.g. iPrSi-7) and cyclic acetals (e.g. iPrAc-7) are synthesized in one step from *cis*-2-butene-1,4-diol, which is available commercially for less than $0.10 per gram, in high yields (≥ 70%). Further, eight-membered cyclic monomers suffer from thermodynamic effects that result in competitive oligomerization during cyclization. The oligomers are easily removed by distillation, but this represents additional energetic inputs and is impractical for high molecular

weight species. The synthesis of a seven-membered ring, however, is less susceptible to oligomer formation. Both iPrSi-7 and iPrAc-7 are synthesized without oligomer formation or the need for distillation. Finally, dichlorosilanes, which are utilized in the synthesis of silyl ethers, are significantly more expensive than the aldehydes required in acetal synthesis. For example, dichlorodiisopropylsilane is available for approximately $4.00 per gram and isobutyraldehyde is available for approximately $0.08 per gram, a fifty-fold difference in price. We therefore rank synthesizability of the cleavable cyclic olefins as follows: iPrAc-7 > iPrSi-7 >> iPrSi-8.

4.3 Frontal Copolymerization of Cleavable Cyclic Olefins

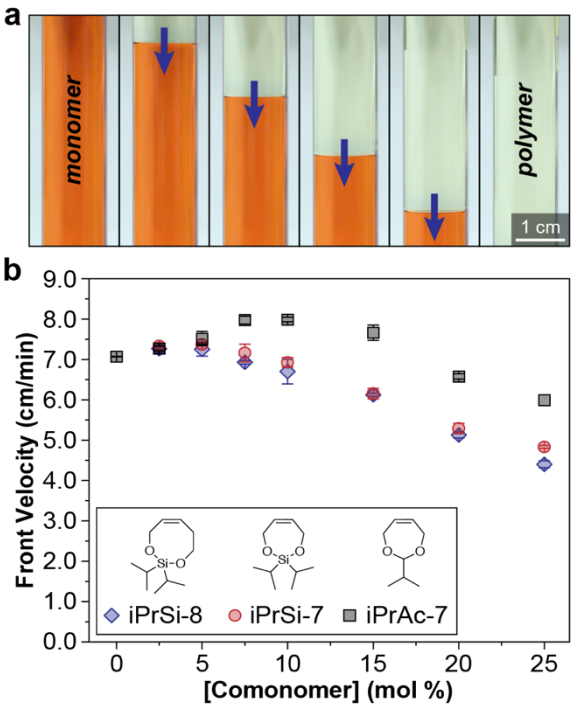

Figure 4.2. Frontal copolymerization of DCPD and cleavable cyclic olefins | a, Optical images of FROMP of DCPD and 10 mol % iPrSi-7 containing 150 ppm Grubbs Catalyst M202 and 1 molar equivalent (with respect to catalyst) of tributyl phosphite. Images were taken at 5 s intervals. Grubbs Catalyst M202, which exhibits a strong color change during propagation, was utilized to enhance visualization of the polymerization front. b, Front velocity measured at various loadings of iPrSi-8, iPrSi-7, and iPrAc-7. All measurements were conducted at 25 °C with 150 ppm Grubbs Catalyst 2nd Generation (GC2) and 1 molar equivalent (with respect to GC2) of tributyl phosphite (TBP). Reported values represent the average and one standard deviation (n = 3).

Each of the candidate monomers possess significantly less ring strain (**Figure 4.1b**) than the norbornene ring of DCPD[31], calculated to be 26.7 kcal mol^{-1}. The low ring strain of the comonomers is anticipated to reduce the energy density of the resin, leading to decreased front velocities at increased comonomer loadings. While it is preferable to have a high ring strain monomer, low ring strain monomers have previously been copolymerized during FROMP of DCPD[24]. Even at 50 vol % cyclooctadiene, Dean and coworkers reported front velocities greater than 4 cm min^{-1}.[24] Further, Shieh and coworkers required less than 10 vol % of cyclic silyl ether to ensure full degradation of oven cured pDCPD. This small fraction of comonomer is expected to have minimal impact on frontal propagation.

Frontal copolymerization of DCPD and cleavable cyclic olefins yields high quality materials free of voids (**Figure 4.2a**) for all comonomers up to the tested 25 mol % loading. Due to the significant difference in ring strain between DCPD and the cleavable comonomers, we anticipate that propagation dynamics will be dominated by the density of DCPD within the system, and monomers with lower molecular weights are, therefore, expected to sustain higher front velocities. Initially, the front velocity increases with increasing comonomer concentration, reaching a maximum at 5 mol % iPrSi-7 and iPrSi-8 and 10 mol% iPrAc-7 (**Figure 4.2b**). This nonmonotonic increase in front velocity has been reported previously[32] and is attributed to the decrease in crosslink density from the incorporation of a monofunctional olefin that reduces the effective activation barriers for frontal propagation[10]. Front velocity then decays steadily due to the decrease in energy density with increased loadings of the less-strained cleavable olefins. iPrSi-8 and iPrSi-7 copolymerizations yield statistically similar trends in front velocity, likely a result of the small (6%) difference in molecular weight. However, the nearly 30% difference in molecular weight between iPrSi-7 and iPrAc-7 leads to significantly higher front velocities when iPrAc-7 is utilized

as a comonomer. We further investigated the impact of atom economy on front velocity by synthesizing a phenyl-substituted seven-membered cyclic acetal (PhSi-7), which represents an increase in molecular weight of 34%. The presence of the phenyl substituents significantly decreases front velocity and results in quenched fronts at 25 mol % loading of PhSi-7 (**Figure 4.3**), supporting our initial hypothesis.

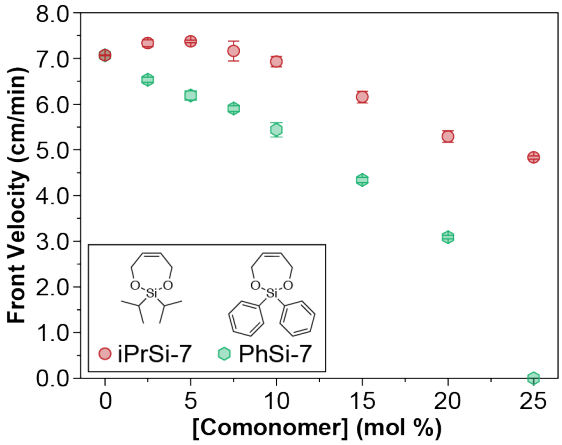

Figure 4.3. Investigation of the importance of atom economy in frontal copolymerization | Front velocity measured at various loadings of iPrSi-7 (MW = 200. 35 g mol^{-1}) and PhSi-7 (MW = 268.39 g mol^{-1}). All measurements were conducted at 25 °C with 150 ppm GC2 and 1 molar equivalent (with respect to GC2) of TBP. Reported values represent the average and one standard deviation (n = 3).

Minimal residual exotherm (< 1 J g^{-1}) is detected during dynamic differential scanning calorimetry (DSC) traces of FROMP copolymers containing up to 15 mol % iPrSi-8 or iPrSi-7. Those containing iPrAc-7 exhibit minimal residual exotherm up to 10 mol%, but at 15 mol % a residual exotherm of 7.8 ± 3.7 J g^{-1} is measured. At 20 mol % comonomer loading, residual exotherms of 3.8 ± 1.1, 10.5 ± 0.5, and 23.7 ± 3.3 J g^{-1} are detected for iPrSi-8, iPrSi-7, and iPrAc-7, respectively. These values increase to 11.4 ± 1.3, 16.9 ± 3.3, and 31.8 ± 3.6 J g^{-1} at 25 mol % comonomer. Unfortunately, the Raman signatures of all three comonomers are masked by pDCPD peaks, making solid state detection of residual comonomer difficult. However, Raman spectra of the copolymers (**Figure 4.4a**) show no signs of unreacted DCPD, suggesting that the residual exotherm is a result of unreacted comonomer. Together, these findings indicate that the

comonomers do not completely incorporate at high concentrations and that iPrAc-7 is incorporated into the polymer network with less efficiency than the silyl ether monomers.

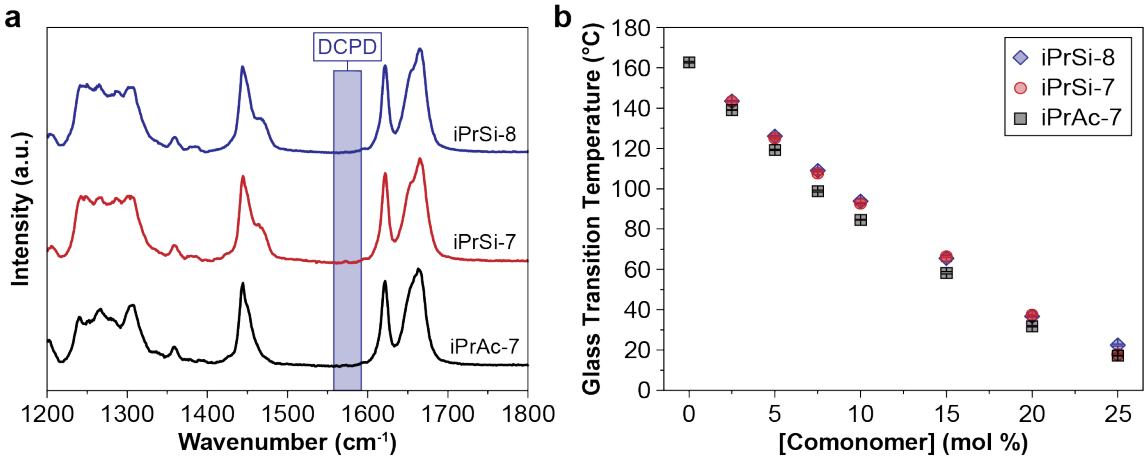

Figure 4.4. Characterization of FROMP copolymers | a, Raman spectra of FROMP copolymers containing 25 mol % cleavable comonomer. The absence of the norbornene C=C stretch of DCPD at 1575 cm^{-1} is noted in all spectra.[33] b, Glass transition temperature of FROMP copolymers at varied cleavable comonomer loadings. T_g was determined as the inflection point in dynamic DSC traces obtained at 5 °C min^{-1}. Reported values represent the average and one standard deviation (n = 3).

Given that pDCPD is typically employed in structural applications[8], we sought to investigate the impact of the cleavable comonomers on the mechanical performance of the resulting thermosets (**Figure 4.4b**). The incorporation of long aliphatic chains into the thermoset significantly reduces the crosslink density and, subsequently, the glass transition temperature (T_g), determined as the inflection point in dynamic DSC traces. The glass transition temperature decreases from 162.7 ± 0.3 °C at 0 % comonomer to approximately 100 °C at 7.5 mol % comonomer. Further increasing the comonomer loading to 25 mol % yields copolymers with T_g values near room temperature. Due to the similarities in the aliphatic chain length and substituents, all three comonomers produce statistically similar trends in T_g. To avoid sacrificing material performance, the comonomer concentration must be minimized.

4.4 Degradation and Upcycling of FROMP Copolymers

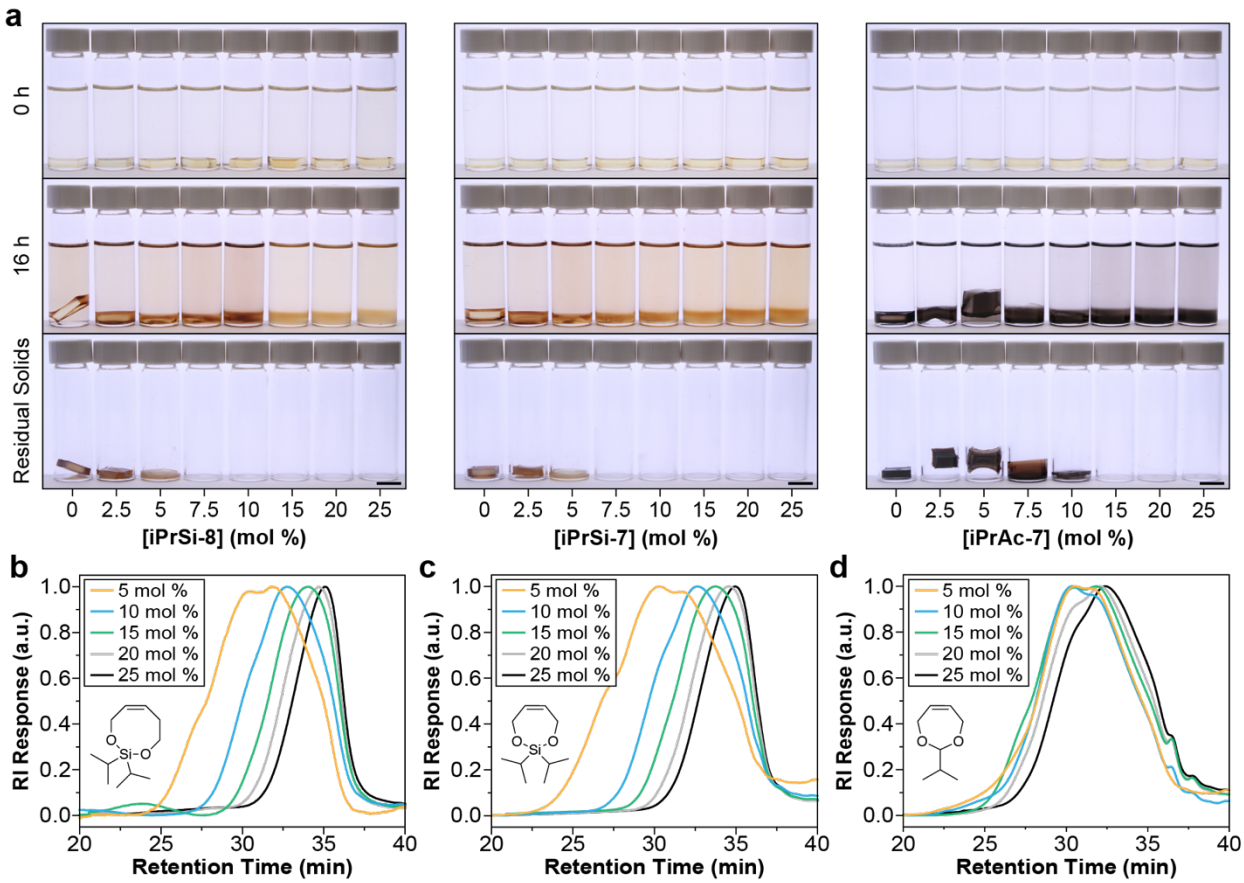

Figure 4.5. Degradation of FROMP copolymers | a, Optical images taken at 0 h and 16 h after submerging thermosets in 1.0 M degradation solutions (TBAF for silyl ether containing thermosets and HCl for acetal containing thermosets) and after removal of the soluble fraction from the residual solids. From left to right, the image sets correspond to iPrSi-8, iPrSi-7, and iPrAc-7 samples. Scale bars are 1 cm. b-d, SEC traces of isolated degradation fragments.

The silyl ether and acetal linkages of the comonomers are easily cleaved by hydrolysis in the presence of either fluoride or acid, respectively. For a typical structural application, these hydrolysis triggers are orthogonal to the service life of the thermoset and are unlikely to result in unwanted degradation. To evaluate the degradability of the FROMP copolymers, samples are immersed in either 1.0 M tetrabutylammonium fluoride (TBAF) solutions for silyl ether copolymers or 1.0 M HCl solutions for acetal copolymers overnight (**Figure 4.5a**). Discoloration is observed in all samples, likely a result of the catalyst reacting with either TBAF or HCl. Samples submerged in TBAF turn brown, and those submerged in HCl turn black. Solutions containing

sufficient cleavable comonomer became cloudy and a brown or black layer forms at the bottom of the vial, which is homogeneously dispersed upon agitation. Samples with insufficient comonomer either remain fully intact (e.g. 0 and 2.5 mol % iPrSi-8) or form an insoluble gel (e.g. 5 mol % iPrSi-8). Complete degradation, indicated by the absence of any residual solids, is observed for samples containing at least 7.5 mol % of iPrSi-8 or iPrSi-7. However, a significantly higher concentration of iPrAc-7, 15 mol %, is required to ensure complete degradation. Shieh and coworkers previously reported that the formation of a random copolymer is critical to degradation at low cleavable comonomer loadings.[28,29] If blocks are formed rather than a random distribution, the cleavable units will fail to disrupt the DCPD crosslinking, and the network will remain intact after hydrolysis of the cleavable units. The relatively higher loadings required when employing iPrAc-7 suggest the comonomer distribution is not completely random, supporting our previous observations that cyclic acetals do not incorporate as efficiently as silyl ethers. The low molar fractions (ca. 7.5 mol %) required to ensure complete degradation in iPrSi-8 and iPrSi-7 will have minimal impact on the properties of FROMP copolymers. Glass transition temperatures greater than 100 °C and front velocities in excess of 7 cm min^{-1} are attainable at these loadings.

Degradation fragments are isolated as white powders from the soluble fraction by dropwise precipitation into methanol. Fragments suitable for characterization are obtained for all samples that exhibited partial (5 mol % iPrSi-8 and iPrSi-7 or 5, 7.5, 10 mol % iPrAc-7) or complete degradation (≥ 7.5 mol % iPrSi-8 and iPrSi-7 or ≥ 15 mol % iPrAc-7). Fragments are isolated in near quantitative yield (ca. 90 %) in samples that fully degrade. This facile and high-yield recovery of desired products is in great contrast to traditional recycling efforts which are often plagued by multiple purification steps and low yields of the desired products[34]. No fragments are isolated for samples which remained fully intact (0 or 2.5 mol % cleavable comonomer). Size exclusion

chromatography (SEC) reveals that the fragments are small oligomers with molecular weights of less than 10 kDa (**Figure 4.5b-d**). Both iPrSi-7 and iPrSi-8 containing samples display very strong fragment size dependence on the comonomer concentration (**Figure 4.5b,c**), indicating a random copolymer network. In a random network, increasing cleavable comonomer loading further disrupts pDCPD containing regions and results in smaller fragments. iPrAc-7 containing thermosets show a weak fragment size dependence on comonomer loading (**Figure 4.5d**). These results suggest that frontal copolymerization DCPD and iPrAc-7 produces blocks of cleavable units, as increasing comonomer loading increases the size of the cleavable blocks but does little to disrupt the pDCPD regions. Subsequently, the size of the fragments changes little at increased loadings.

Hydrolysis of the cleavable units yields oligomers with terminal hydroxyl units and a high concentration of olefin functionality. Shieh and coworkers previously utilized the residual olefins to seamlessly integrate degradation fragments as fillers in new pDCPD networks.[29] Materials containing degradation fragments exhibited comparable mechanical properties to a pristine pDCPD network. We sought to, instead, utilize the hydroxyl functionality to create new polymeric materials, in particular polyurethane networks (**Figure 4.6a**). ^{1}H NMR of the degradation fragments shows peaks corresponding to CH_2-OH functionality near 4 ppm, confirming the presence of hydroxyl units (**Figure 4.6b**). Comparison of the integration values of these peaks with that of a mesitylene internal standard reveals that the fragments obtained from a 20 mol % iPrSi-7 thermoset contain 1.0×10^{-3} mmol hydroxyl units per mg of fragments.

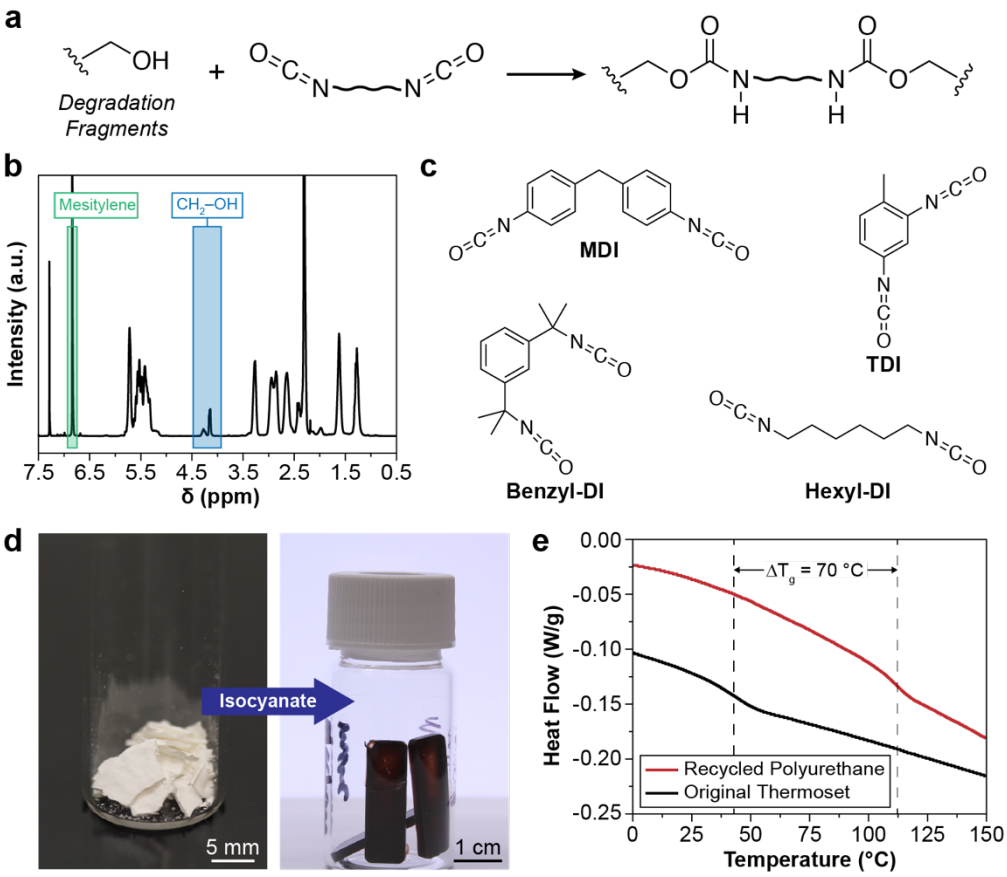

Figure 4.6. Upcycling of degradation fragments | a, Schematic representation of the incorporation of degradation fragments into a polyurethane network with a diisocyanate. b, ^{1}H NMR spectrum of degradation fragments from a thermoset containing 20 mol % iPrSi-7. c, Example diisocyanates utilized when upcycling degradation fragments (MDI = 4,4'-methylenebis(phenyl isocyanate), TDI = tolylene-2,4-diisocyanate, benzyl-DI = 1,3-bis(1-isocyanato-1-methylethyl)benzene, hexyl-DI = hexamethylene diisocyanate). d, Optical images of the degradation products isolated from a thermoset containing 20 mol % iPrSi-7 (left) and the free-standing films obtained after reaction with MDI (right). e, Dynamic DSC traces obtained at 5 °C min^{-1} for a pDCPD thermoset containing 20 mol % iPrSi-7 and the recycled polyurethane film shown in d.

We next probe the reaction conditions required to generate high quality polyurethanes from the degradation fragments. The activity of several diisocyanates (**Figure 4.6c**) is evaluated in the presence of a 1,4-diazabicyclo[2.2.2]octane (DABCO) catalyst. The diisocyanates and DABCO are mixed with the degradation fragments at 50 and 20 mol % loadings (with respect to the hydroxyl content), respectively, in tetrahydrofuran. After 22 h reaction time, both MDI and TDI generate a gelled material. Removal of tetrahydrofuran yields a crosslinked material that is insoluble in dichloromethane. No observable gelation is detected in samples containing benzyl-DI

or hexyl-DI, suggesting less reactivity with the fragments. Further, when DABCO is removed, no gelation is observed after 22 h, confirming the need for a catalyst. Utilizing a more active catalyst, dibutyltin dilaurate (DBTL), results in gelation for all four diisocyanates. We therefore propose the use of MDI and DBTL to generate polyurethane networks from the FROMP copolymer degradation products.

Free-standing polyurethane films are prepared by dissolving degradation fragments and MDI (50 mol %) in THF (100 mg solids per 0.7 mL THF). DBTL (20 mol %) is added and the solution is rapidly transferred to a mold and allowed to set at room temperature for 1 h. THF is then slowly removed by heating at 50 °C under a steady flow of N_2 for two days. The robust free-standing films (**Figure 4.6d**) are easily handled and sustain significant bending without cracking. The thermomechanical properties of the resulting polyurethane films are probed via dynamic DSC at 5 °C min^{-1} and compared to the original pDCPD network, which contained 20 mol % iPrSi-7. By replacing the flexible aliphatic chain of the silyl ether with a rigid, aromatic urethane, an increase in T_g of 70 °C is observed. Impressively, the glass transition temperature of the polyurethane is greater than any of the FROMP copolymers that fully degrade. These promising results suggest that recycling, and even upcycling, is possible for high performance thermosets.

4.5 Conclusions

We have presented, for the first time, a rapid and energy-efficient route to fully degradable and recyclable thermosets through frontal copolymerization. Three cleavable comonomers, seven- and eight-membered cyclic silyl ethers and seven-membered cyclic acetals, were evaluated on the metrics of synthesizability, performance during frontal copolymerization, and degradability. While seven-membered cyclic acetals offered the easiest and most scalable synthetic routes and the fastest front velocities, they suffered from inefficient incorporation into the polymer network.

Subsequently, a relatively high concentration of acetal was needed to ensure full degradation by hydrolysis of the acetal unit. We therefore selected iPrSi-7, which displayed a balance among synthesizability, high front velocities, and degradability at low loadings, as the best candidate comonomer for degradable FROMP copolymers. Degradation fragments were easily isolated in near quantitative yield, and the terminal hydroxyl groups were leveraged to generate polyurethane networks upon reaction with a diisocyanate. The thermomechanical properties of the resulting polyurethane films were superior to those of the original pDCPD networks, a true embodiment of upcycling. With its speed and energy efficiency, frontal polymerization truly represents a paradigm shift in materials manufacturing. This fundamental study highlights to ability to generate multifunctional materials through frontal polymerization and will stimulate the development of a library of functional cyclic olefin comonomers.

4.6 Experimental Details

4.6.1 Materials

All reagents were purchased from commercial suppliers and used as received unless otherwise noted. Dogbone molds were prepared with RTV630 silicone rubber compound from Momentive®. To depress the freezing point of DCPD, 5 wt% ENB was blended with DCPD at 35 °C. The liquid mixture was then degassed overnight at room temperature and 15 kPa with stirring. All references to DCPD refer to the 95:5 DCPD:ENB mixture.

4.6.2 Synthesis of 7-membered Cyclic Silyl Ethers

iPrSi-7

iPrSi-7 was synthesized by dissolving 8.8 g of *cis*-butene-1,4-diol (100 mmol) and 13.6 g of imidazole (200 mmol, 2 equiv.) in 2 L anhydrous dichloromethane in a flame-dried flask charged with a stir bar. 18.0 mL of dichlorodiisopropylsilane (18.5 g, 100 mmol, 1 equiv.) was dissolved in 120 mL of anhydrous dichloromethane and added dropwise to the reaction flask over 1 h, during which time a white precipitate formed. The reaction mixture was filtered over a pad of silica and concentrated to yield 8.8 g **iPrSi-7** (67 %) as a clear oil which was analytically pure. ^{1}H NMR (500 MHz, chloroform-*d*) δ 5.70 (t, *J* = 1.9 Hz, 2H), 4.50 (d, *J* = 1.8 Hz, 4H), 1.07 (d, *J* = 2.0 Hz, 14 H).

PhSi-7

PhSi-7 was synthesized by dissolving 8.8 g of *cis*-butene-1,4-diol (100 mmol) and 13.6 g of imidazole (200 mmol, 2 equiv.) in 2 L anhydrous dichloromethane in a flame-dried flask charged with a stir bar. 21.0 mL of dichlorodiphenylsilane (25.3 g, 100 mmol, 1 equiv.) was dissolved in 120 mL of anhydrous dichloromethane and added dropwise to the reaction flask over 1 h, during which time a white precipitate formed. The reaction mixture was filtered over a pad of silica to remove imidazolium salts and concentrated. The cloudy residue was distilled under vacuum (0.1 torr, 200 °C) to yield 8.9 g **PhSi-7** (33%) as a clear oil. ^{1}H NMR (500 MHz, chloroform-*d*) δ 7.78 – 7.73 (m, 4H), 7.52 – 7.46 (m, 2H), 7.46 – 7.39 (m, 4H), 5.79 (t, *J* = 1.9 Hz, 2H), 4.61 (d, *J* = 1.9 Hz, 4H).

4.6.3 Synthesis of 8-membered Cyclic Silyl Ether

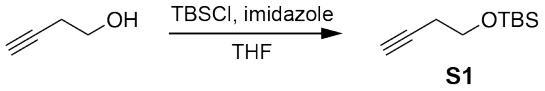

S1

The 8-membered cyclic silyl ether was synthesized according to literature procedure.[28] In the first step, a TBS-protected alkyne (**S1**) was synthesized by dissolving 20.0 g of 3-butynol (285 mmol) in 200 mL of anhydrous THF in a flame-dried flask charged with a stir bar under a dry nitrogen environment. 43.0 g of *tert*-butyldimethylsilyl chloride (285 mmol, 1 equiv.) and 29.1 g of imidazole (428 mmol, 1.5 equiv.) were added. The mixture was stirred at room temperature for 2 h, filtered to remove imidazolium salts, and concentrated. The remaining oil was diluted in 200 mL of diethyl ether and washed with 200 mL of saturated ammonium chloride and 200 mL of saturated sodium bicarbonate. The organics were dried over sodium sulfate and concentrated. The oil was dried overnight *in vacuo* to yield 48.7 g (92.7%) of **S1**. NMR spectra matched those reported in literature.[35]

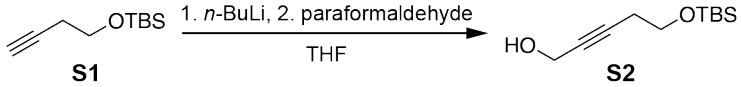

S1 **S2**

S1 (41.7 g, 226 mmol) was dissolved in 400 mL dry THF in a flame-dried flask charged with a stir bar under an ultra-high purity argon environment. The mixture was cooled to -78 °C in a dry ice/acetone bath. 95 mL of 2.5 M *n*-butyllithium (237.3 mmol, 1.05 equiv.) was added dropwise over 20 minutes. The reaction mixture was stirred at -78 °C for 1 h and then gently warmed to 0 °C. Next, 8.1 g of paraformaldehyde (271.3 mmol, 1.2 equiv.) was added in a single portion. The reaction mixture was stirred overnight at room temperature and quenched by adding 300 mL ammonium chloride. 300 mL of diethyl ether was added, and the organic layer was extracted. The aqueous layer was washed with 300 mL of diethyl ether, and the combined organic layers were dried over sodium sulfate and concentrated. The pale yellow oil was purified by silica gel

chromatography with 6:1 hexanes:ethyl acetate to yield 36.3 g of **S2** (75%). NMR spectra matched those in literature.[36]

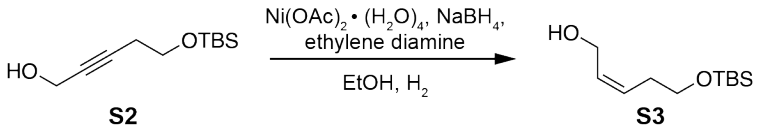

S2 **S3**

In the next step, 3.0 g of nickel acetate tetrahydrate (12.2 mmol, 0.13 equiv.) was added to 200 mL of anhydrous ethanol under a dry nitrogen environment. The reaction mixture was placed under a hydrogen atmosphere with hydrogen filled balloons. A solution of 0.630 g of sodium borohydride (16.7 mmol, 0.178 equiv.) in 50 mL anhydrous ethanol was added to the reaction mixture. The light teal solution immediately turned black upon addition of the sodium borohydride solution. The mixture was stirred for 30 min under H_2 and 3.7 mL of ethylene diamine (3.3 g, 54.8 mmol, 0.586 equiv) was added. A solution of **S2** (20.0 g, 93.5 mmol) in 60 mL anhydrous ethanol was added to the reaction mixture. The mixture was stirred overnight at room temperature under H_2 atmosphere. The flask was evacuated of hydrogen, and 500 mL diethyl ether was added. The mixture was passed through a pad of silica to remove Ni salts and then concentrated. The residue was purified with a short silica plug using 4:1 hexanes:ethyl acetate to yield 16.7 g (82%) of **S3** as a clear oil. NMR spectra matched those reported in literature.[28]

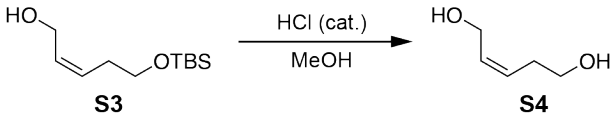

S3 **S4**

During the deprotection of **S3**, 16.7 g of **S3** (77.0 mmol) was added to 250 mL of MeOH containing 1 vol% concentrated HCl. The reaction was stirred at room temperature while monitoring the progress by TLC. After 15 min, conversion to product was observed, and the reaction was quenched by adding 30 wt% aqueous sodium hydroxide. The mixture was concentrated, diluted in 100 mL diethyl ether, and filtered to remove NaCl. The mixture was dried over sodium sulfate and concentrated. The residue was purified by silica gel chromatography with

10:1 dichloromethane:methanol to yield 7.0 g of **S4** (89%) as a clear oil. NMR spectra matched those reported in literature.[28]

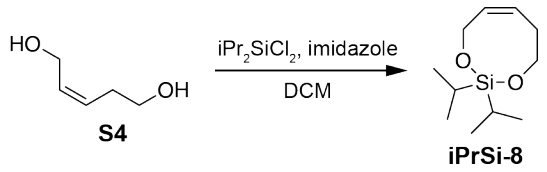

iPrSi-8 was synthesized by dissolving 3.6 g of **S4** (35.8 mmol) and 4.88 g of imidazole (71.6 mmol, 2 equiv.) in 1.8 L anhydrous dichloromethane in a flame-dried flask charged with a stir bar. Next, 6.5 mL of dichlorodiisopropylsilane (6.63 g, 35.8 mmol, 1 equiv.) was added dropwise over 5 minutes, during which time a white precipitate formed. The mixture was stirred at room temperature for 3 h, filtered to remove imidazolium salts, and concentrated. The cloudy yellow residue was distilled under vacuum (50 mTorr, 130 °C) to yield a clear oil free of any oligomers that formed during the reaction. The oil was further purified by silica gel chromatography with 20:1 hexanes:ethyl acetate to yield 4.77 g of **iPrSi-8** (61%) as a clear oil, which was stored at -20 °C until use. NMR spectra matched those reported in literature.[28]

4.6.4 Synthesis of 7-membered Cyclic Acetal

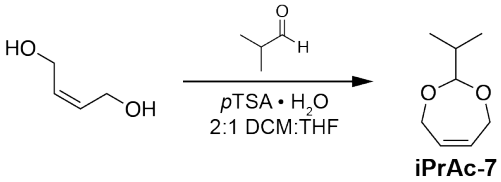

iPrAc-7 was synthesized by dissolving 15.0 g *cis*-2-butene-1,4-diol (170 mmol), 16.0 g isobutyraldehyde (221 mmol, 1.3 equiv.), and 0.97 g *p*-toluenesulfonic acid monohydrate (5.1 mmol, 0.03 equiv.) in 120 mL of a 2:1 mixture of dichloromethane:tetrahydrofuran in a flame-dried flask charged with a stir bar. Sodium sulfate was added until the supernatant was clear, and the mixture was stirred overnight at room temperature. The reaction mixture was filtered and concentrated under gentle vacuum. The clear oil was purified by basic alumina column

chromatography with 8:1 hexanes:ethyl acetate to yield 22.2 g **iPrAc-7** (92%) as a clear oil, which was stored at -20 °C until use. ^{1}H NMR (500 MHz, chloroform-*d*) δ 5.72 (m, 2H, CH=CH), 4.43 – 4.13 (m, 4 H, CH_2), 4.33 (d, J = 6.9 Hz, 1 H, acetal), 1.96 – 1.84 (m, 1H, CH), 0.95 (d, J = 6.8 Hz, CH_3).

4.6.5 Frontal Polymerization of Cyclic Comonomers with Dicyclopentadiene

To prepare a frontal polymerization resin containing 10 mol % **iPrSi-8**, 5.0 mg GC2 (0.00589 mmol) was weighed out in a vial. In a separate vial, TBP (1.6 μL, 0.00589 mmol) was added to a mixture of DCPD (4.67 g, 35.3 mmol) and **iPrSi-8** (0.84 g, 3.93 mmol). The solution was added to the vial containing GC2, and the mixture was sonicated for 10 min to ensure complete dissolution of GC2. The resin was filtered with a 0.45 μm PTFE syringe filter from Fisher Scientific to remove any particulates. The filtered solution was added to a dogbone mold with gauge dimensions of 25.4 mm × 3.75 mm × 4.00 mm consisting of RTV 630 silicone molding compound and a glass slide (75.0 mm × 25.0 mm × 1.00 mm) clamped to the open surface of the mold. The resin and mold were equilibrated to 25.0 °C in a MicroClimate environmental chamber from Cincinnati Sub-Zero Products. Frontal polymerization was initiated within the environmental chamber with a soldering iron, and frontal propagation was tracked optically. Front velocity was calculated as the slope of a best-fit line of the frontal position over time within the gauge length of the dogbone mold. Samples containing various comonomers at varied concentration were prepared in a similar manner.

4.6.6 Degradation of Copolymers and Isolation of Degradation Fragments

After frontal polymerization, copolymer samples were cut to the desired dimensions (8 mm x 10 mm x 3 mm) and placed in 7 mL glass scintillation vials. 5 mL of degradation solution, 1.0 M TBAF in THF for copolymers containing silyl groups or 1.0 M HCl in cyclopentyl methyl ether

for copolymers containing acetal groups, were added to the vials. Degradation was monitored optically with a Canon EOS 7D camera equipped with a 100 mm macro lens. Following a 16 h period, the soluble fraction was removed, and the residual solids that remained in the vials were dried overnight *in vacuo*. The degradation fragments were isolated from the soluble fraction by dropwise precipitation into cold methanol. The fragments were further purified by an additional dropwise precipitation from THF in cold methanol. After isolation, the fragments were dried overnight *in vacuo*.

4.6.7 Upcycling of Degradation Products

The activity of several diisocyanates and catalysts was evaluated by charging a two-dram vial equipped with a stir bar with 40 mg of degradation products, 50 mol % (relative to the molar concentration of hydroxyl groups in the degradation products, as measured by ^{1}H NMR) of diisocyanate (4,4'-methylenebis(phenyl isocyanate), tolylene-2,4-diisocyanate, 1,3-bis(1-isocyanato-1-methylethyl)benzene, or hexamethylene diisocyanate), and 20 mol % (relative to the hydroxyl groups of the degradation products) of either 1,4-diazabicyclo[2.2.2]octane (DABCO) or dibutyltin dilaurate (DBTL). The vial was backfilled with nitrogen three times and 0.5 mL anhydrous THF was added. The reaction mixtures were stirred at room temperature for 22 h. Gelation of the mixture indicated the formation of a crosslinked network. Free-standing polymer films were prepared in a similar manner. Degradation products and 50 mol % diisocyanate were dissolved in minimal THF (approximately 100 mg solids per 0.7 mL THF). 20 mol % of the catalyst was added, and the mixture was rapidly transferred to a mold. The mixture was allowed to set at room temperature for 1 h, and then solvent was removed slowly by heating at 50 °C under a steady flow of N_2 for two days.

4.6.8 Materials Characterization

^{1}H and ^{13}C NMR spectra were obtained in chloroform-*d* or dichloromethane-d_2 with a Carver 500 MHz spectrometer provided by the School of Chemical Science NMR laboratory at the University of Illinois at Urbana-Champaign. Raman spectra were obtained with a Horiba LabRAM HR 3D Raman confocal imaging microscope equipped with an 830 nm laser, a 300 groove mm^{-1} grating (blazed at 600 nm), a long working distance 20× objective from Leica, and a Horiba Synapse back-illuminated deep depletion CCD camera provided by the Imaging and Technology Group at the Beckman Institute for Advanced Science and Technology at the University of Illinois at Urbana-Champaign. Analytical size exclusion chromatography (SECC) traces were obtained in THF at 30 °C using a system consisting of a Waters 1515 isocratic HPLC pump, Waters 2707 96-well autosampler, Waters 2414 refractive index detector, and 4 Waters HR Styragel Column (7.8 × 300 mm, HR1, HR3, HR4, and HR5). The GPC system was calibrated using monodisperse polystyrene standards.

Differential scanning calorimetry (DSC) traces were obtained with a Discovery 250 DSC equipped with an RCS 90 cooling system and an autosampler. DSC samples were prepared by grinding the top and bottom surfaces of the frontally polymerized dogbones until the specimens were 500 μm thick on a MetPrep 3 polisher from Allied High Tech Products, Inc. equipped with silicon carbide grinding papers. A small section (approximately 8.0 mg) of the polished dogbone gauge length was cut with a razorblade, weighed on an analytical balance (XPE205, Mettler-Toledo), and transferred to Tzero® aluminum pans. Traces were obtained from -50 to 200 °C at 5 °C min^{-1}. The glass transition temperature was defined as the inflection point in DSC traces.

4.7 Notes and References

4.7.1 Notes

This is a collaborative effort with multiple contributors. E.M.L synthesized and characterized all comonomers and performed the frontal polymerization, DSC, and degradation experiments. Julian Cooper performed NMR and GPC characterization of the degradation products. E.M.L, Douglas Ivanoff, and Julian Cooper contributed to recycling and upcycling efforts. E.M.L authored the text.

4.7.2 References

1. Mishnaevsky, L.; Branner, K.; Petersen, H. N.; Beauson, J.; McGugan, M.; Sørensen, B. F. Materials for Wind Turbine Blades: An Overview. *Materials* **2017**, 10, 1285.
2. Brøndsted, P.; Lilholt, H.; Lystrup, A. Composite Materials for Wind Power Turbine Blades. *Annu. Rev. Mater. Res.* **2005**, 35, 505-538.
3. Abliz, D.; Duan, Y.; Steuernagel, L.; Xie, L.; Li, D.; Ziegmann, G. Curing Methods for Advanced Polymer Composites - A Review. *Polym. Polym. Compos.* **2013**, 21, 341-348.
4. Pickering, S. J. Recycling Technologies for Thermoset Composite Materials-Current Status. *Composites, Part A* **2006**, 37, 1206-1215.
5. Martin, C. Wind Turbine Blades Can't Be Recycled, So They're Piling Up in Landfills; 2020; Retrieved from: https://www.bloomberg.com/news.
6. Red, C. Wind Turbine Blades: Big and Getting Bigger; 2008; Retrieved from: https//www.compositesworld.com/articles.
7. Pojman, J. A. in *Polymer Science: A Comprehensive Reference* Vol. 4 (eds. Matyjaszewski, K. & Möller, M.) Elsevier: Amsterdam, 2012; pp. 957-980.
8. Robertson, I. D.; Yourdkhani, M.; Centellas, P. J.; Aw, J. E.; Ivanoff, D. G.; Goli, E.; Lloyd, E. M.; Dean, L. M.; Sottos, N. R.; Geubelle, P. H.; Moore, J. S.; White, S. R. Rapid Energy-Efficient Manufacturing of Polymers and Composites via Frontal Polymerization. *Nature* **2018**, 557, 223-227.
9. Pojman, J. A. Traveling Fronts of Methacrylic Acid Polymerization. *J. Am. Chem. Soc.* **1991**, 113, 6284-6286.
10. Masere, J.; Stewart, F.; Meehan, T.; Pojman, J. A. Period-Doubling Behavior in Frontal Polymerization of Multifunctional Acrylates. *Chaos* **1999**, 9, 315-322.
11. Nason, C.; Roper, T.; Hoyle, C.; Pojman, J. A. UV-Induced Frontal Polymerization of Multifunctional (Meth)Acrylates. *Macromolecules* **2005**, 38, 5506-5512.
12. Chen, S.; Hu, T.; Tian, Y.; Chen, L.; Pojman, J. A. Facile Synthesis of Poly(Hydroxyethyl Acrylate) by Frontal Free-radical Polymerization. *J. Polym. Sci., Part A: Polym. Chem.* **2007**, 45, 873-881.
13. Morales, A.; Pojman, J. A. A Study of the Effects of Thiols on the Frontal Polymerization and Pot Life of Multifunctional Acrylate Systems with Cumene Hydroperoxide. *J. Polym. Sci., Part A: Polym. Chem.* **2013**, 51, 3850-3855.
14. Holt, J.; Fazende, K.; Jee, E.; Wu. Q.; Pojman, J. A. Cure-on-Demand Wood Adhesive Based on the Frontal Polymerization of Acrylates. *J. Appl. Polym. Sci.* **2016**, 133, 44064.
15. Bansal, K.; Pojman, J. A.; Webster, D.; Quadir, M. Frontal Polymerization of a Thin Film on a Wood Substrate. *ACS Macro Lett.* **2020**, 9, 169-173.
16. White, S. R.; Kim, C. A. Simultaneous Lay-Up and in situ Cure Process for Thick Composites. *J. Reinf. Plast. Comp.* **1993**, 12, 520-535.
17. Chekanov, Y.; Arrington, D.; Brust, G.; Pojman, J. A. Frontal Curing of Epoxy Resins: Comparison of Mechanical and Thermal Properties to Batch-Cured Materials. *J. Appl. Polym. Sci.* **1997**, 66, 1209-1216.

18. Scognamillo, S.; Bounds, C.; Luger, M.; Mariani, A.; Pojman, J. A. Frontal Cationic Curing of Epoxy Resins. *J. Polym. Sci., Part A: Polym. Chem.* **2010**, 48, 2000-2005.
19. Lecompère, M.; Allonas, X.; Maréchal, D.; Criqui, A. Versatility of Pyrylium Salt/Vinyl Ether Initiating System for Epoxide Dual-Cure Polymerization: Kick-Starting Effect of the Coinitiator. *Macromol. Rapid Commun.* **2017**, 38, 1600660.
20. Mariani, A.; Bidali, S.; Fiori, S.; Sangermano, M.; Malucelli, G.; Bongiovanni, R.; Priola, A. UV-ignited Frontal Polymerization of an Epoxy Resin. *J. Polym. Sci., Part A: Polym. Chem.* **2004**, 42, 2066-2072.
21. Mariani, A. Fiori, S.; Chekanov, Y.; Pojman, J. A. Frontal Ring-Opening Metathesis Polymerization of Dicyclopentadiene. *Macromolecules* **2001**, 34, 6539-6541.
22. Robertson, I. D.; Pruitt, E. L.; Moore, J. S. Frontal Ring-Opening Metathesis Polymerization of Exo-Dicyclopentadiene for Low Catalyst Loadings. *ACS Macro Lett.* **2016**, 5, 593-596.
23. Robertson, I. D.; Dean, L. M.; Rudebusch, G. E.; Sottos, N. R.; White, S. R.; Moore, J. S. Alkyl Phosphite Inhibitors for Frontal Ring-Opening Metathesis Polymerization Greatly Increase Pot Life. *ACS Macro Lett.* **2017**, 6, 609-612.
24. Dean, L. M.; Wu, Q.; Alshangiti, O.; Moore, J. S.; Sottos, N. R. Rapid Synthesis of Elastomers and Thermosets with Tunable Thermomechanical Properties. *ACS Macro Lett.* **2020**, 819-824.
25. Dean, L. M.; Ravindra, A.; Guo, A. X.; Yourdkhani, M.; Sottos, N. R. Photothermal Initiation of Frontal Polymerization Using Carbon Nanoparticles. *ACS Appl. Polym. Mater.* **2020**, 2, 4690-4696.
26. Stawiasz, K. J.; Paul, J. E.; Schwarz, K. J.; Sottos, N. R.; Moore, J. S. Photoexcitation of Grubbs' Second-Generation Catalyst Initiates Frontal Ring-Opening Metathesis Polymerization. *ACS Macro Lett.* **2020**, 9, 1563-1568.
27. Moatsou, D.; Nagarkar, A.; Kilbinger, A. F. M.; O'Reilly, R. K. Degradable Precision Polynorbornenes via Ring-Opening Metathesis Polymerization. *J. Polym. Sci., Part A: Polym. Chem.* **2015**, 54, 1236-1242.
28. Shieh, P.; Nguyen, H. V.-T.; Johnson, J. A. Tailored Silyl Ether Monomers Enable Backbone-Degradable Polynorbornene-Based Linear, Bottlebrush and Star Copolymers through ROMP. *Nat. Chem.* **2019**, 11, 1124-1132.
29. Shieh, P.; Zhang, W.; Husted, K. E. L.; Kristufek, S. L.; Xiong, B.; Lundberg, D. J.; Lem, J.; Veysset, D.; Sun, Y.; Nelson, K. A.; Plata, D. L.; Johnson, J. A. Cleavable Comonomers Enable Degradable, Recyclable Thermoset Plastics. *Nature* **2020**, 583, 542-547.
30. Feist, J. D.; Xia, Y. Enol Ethers Are Effective Monomers for Ring-Opening Metathesis Polymerization: Synthesis of Degradable and Depolymerizable Poly(2,3-Dihydrofuran). *J. Am. Chem. Soc.* **2020**, 142, 1186-1189.
31. Njoroge, I.; Kempler, P. A.; Deng, X.; Arnold, S. T.; Jennings, G. K. Surface-Initiated Ring-Opening Metathesis Polymerization of Dicyclopentadiene from the Vapor Phase. *Langmuir* **2017**, 33, 13903-13912.
32. Liu, H.; Wei, H.; Moore, J. S. Frontal Ring-Opening Metathesis Copolymerization: Deviation of Front Velocity from Mixing Rules. *ACS Macro Lett.* **2019**, 8, 846–851.
33. Aldridge, M.; Shankar, C.; Zhen, C.; Sui, L.; Kieffer, J.; Caruso, M.; Moore, J. Combined Experimental and Simulation Study of the Cure Kinetics of DCPD. *J. Compos. Mater.* **2010**, 44, 2605-2618.
34. Schneiderman, D. K.; Hillmyer, M. A. 50th Anniversary Perspective: There Is a Great Future in Sustainable Polymers. *Macromolecules* **2017**, 50, 3733-3749.
35. Al-Shuhaib, Z.; Böckemeier, H.; Coghlan, L.; Dörksen, E.; Jones, I. V.; Murphy, P. J.; Nash, R.; Page, J. M. Intramolecular Palladium Mediated π-Allyl Cyclisation of Bis-Cbz- and Bis-Boc-Protected Guanidines. *Tetrahedron Lett.* **2013**, 54, 6716-6718.
36. Trost, B. M.; Kalnmals, C. A. Stereoselective Synthesis of Exocyclic Tetrasubstituted Vinyl Halides via Ru-Catalyzed Halotropic Cycloisomerization of 1,6-Haloenynes. *Org. Lett.* **2017**, 19, 2346-2349.

Chapter 5: Spontaneous Patterning during Frontal Polymerization

5.1 Introduction

Throughout nature, patterns of various shapes, sizes, and colors adorn biological materials. These multiscale patterns impart organisms with unique characteristics that are critical to their survival. Patterns serve a diverse array of functions, including extraordinary fracture toughness (e.g. the layering of hard and soft domains in glass sea sponge spicules[1] and nacre[2,3]), tactile sensing (e.g. textured surface of a fingertip[4]), intimidation (e.g. the coloration of an emperor angel fish), and camouflage (e.g. the spots on a cheetah) (**Figure 5.1a**). Structural complexity and function in natural systems are derived from initial states of high symmetry and emerge during the growth and development of an organism[5–8]. In great contrast, patterns and structures in synthetic materials are generated by multistep manufacturing processes such as layer-by-layer assembly[9], lithography[10], or molding and casting. In lieu of traditional manufacturing processes, we seek autonomous routes of patterning synthetic structural materials more akin to biological patterning.

Coupled reaction-transport processes are versatile yet underexplored methods for manufacturing as they exhibit unique opportunities to control the spatial properties of materials, achieving order through spontaneous symmetry breaking events[11,12]. Elegant and controllable multiscale patterns and structures have been created in a variety of media with reaction-mass transport processes[13–20]. These initial demonstrations are limited to solutions, gels, or thin membranes as mass transport is prohibitively slow in solid media. Thermally driven reaction-transport networks provide an unexplored yet promising route to the autonomous formation of patterns in structural materials, since thermal transport is orders of magnitude faster than mass transport. In this report, we exploit frontal polymerization as an alternative to traditional reaction-

mass transport networks and demonstrate spontaneous pattern development during the frontal ring-opening metathesis polymerization of strained cyclic olefins.

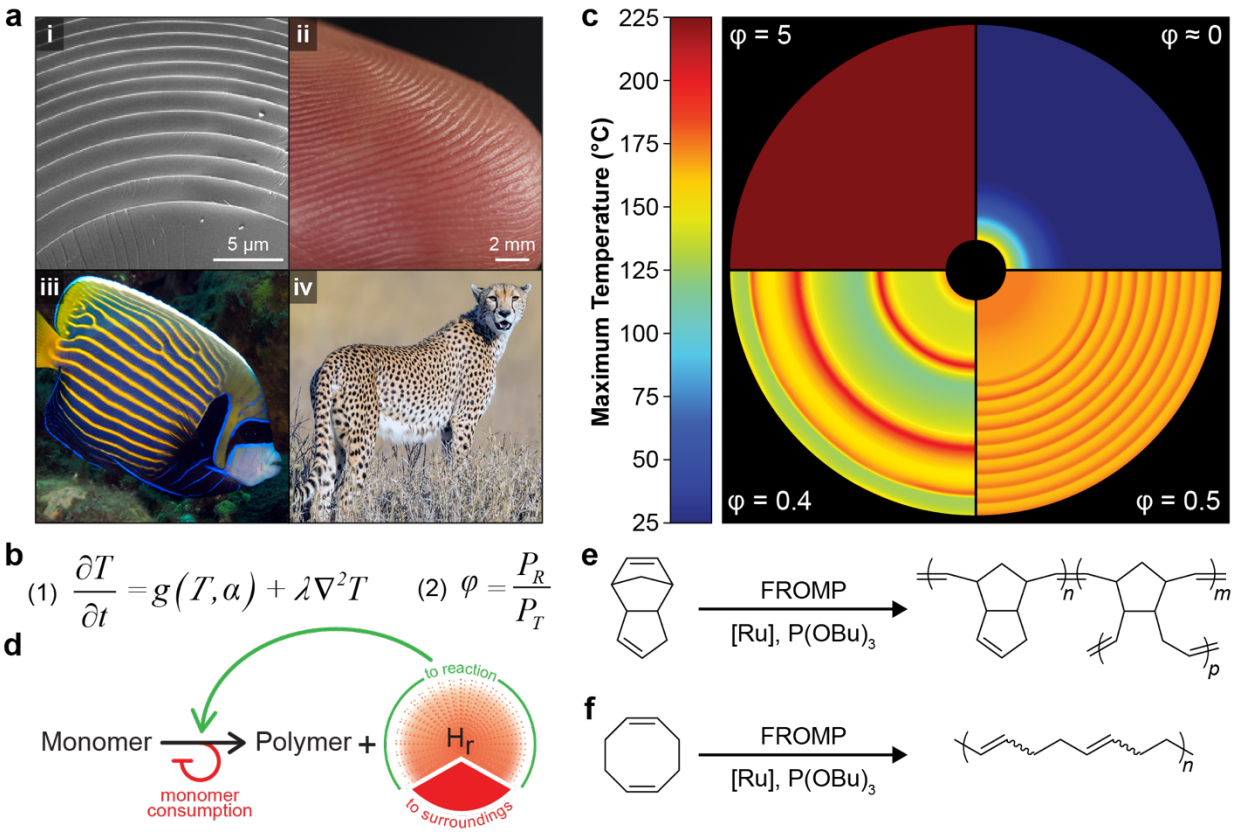

Figure 5.1. Conceptual design of patterning with frontal polymerization. a, Complex patterns in nature that enable functional properties – (i) microstructure of a glass sea sponge spicule (image courtesy of Peter Fratzl, Max Planck Institute of Colloids and Interfaces. From Aizenberg et al.[1]), (ii) textured surface of a fingertip, (iii) adult emperor angel fish (used with permission from Florent Charpin), and (iv) spots of a cheetah (used with permission from Brian Jones). b, Equation (1): coupled reaction and thermal transport (only diffusion considered for simplicity) inherent to frontal polymerization, where T, α, and λ represent the temperature, extent of reaction, and thermal diffusivity of the resin, respectively. Equation (2): ratio of power density generated by reaction (P_R) and spread by thermal transport (P_T) during frontal polymerization. c, Computed thermal profiles of frontal polymerization with different values of φ. The inner and outer radii of the circular area are 0.5 mm and 5 mm, respectively. d, Feedback mechanism for spontaneous patterning during frontal polymerization via competition between thermal transport and chemical reaction. Using the heat generated by the reaction (H_r), thermal transport to the reaction spontaneously heats unreacted monomer, activating the initiator toward polymerization. Once the polymerization reaction consumes the available monomer within the activated zone, the rate of heat release decreases, inhibiting further activation. Competition between reaction and transport generates thermal patterns that are exploited for material property variations. e,f, Frontal ring-opening metathesis polymerization (FROMP) of dicyclopentadiene (e) and 1,5-cyclooctadiene (f) by a thermally activated ruthenium catalyst (Grubbs 2nd generation, GC2) inhibited by tributyl phosphite.

5.2 Breaking Symmetry with Frontal Polymerization

During frontal polymerization (FP), a small energetic input activates a thermally latent initiator, and transport of heat (either through diffusion, convection, or advection) from the highly exothermic polymerization reaction drives the propagation of the polymerization front. In the absence of propagation instabilities, uniform temperature profiles and a homogeneous final state are obtained[21–24]. Unstable frontal propagation, however, spontaneously generates complex thermal instabilities[25–31]. We hypothesize that, when combined with orthogonal chemistries, the undulations in temperature which emerge in the presence of propagation instabilities can be harnessed to pattern material properties.

To guide experimental design, we sought, in collaboration with Philippe Geubelle's group, to numerically determine the key parameters governing propagation stability. Previous models of propagating reaction fronts (e.g. combustion and self-propagating high-temperature synthesis) utilize the Zeldovich number to describe the transition into instability[32–35]. However, the Zeldovich number considers only the initial temperature, maximum front temperature, and activation energy. Our numerical simulations (**Figure 5.1b,c** and **Figure 5.2**) revealed that the spatial and temporal balance of thermal power density (expressed by the ratio φ in Equation 2 in **Figure 5.1b**) generated by the polymerization reaction (P_R, J m^{-3} s^{-1}) and diffused by thermal transport (P_T, J m^{-3} s^{-1}) dictates the development of thermal instabilities during frontal propagation (detailed description of φ in **Figure 5.2**). Under typical conditions, the power generated during polymerization far exceeds that diffused by thermal transport ($\varphi >> 1$), and the polymerization front propagates with constant velocity and temperature (**Figure 5.1c**, $\varphi = 5$). When transport is dominant ($\varphi << 1$), heat diffuses away from the reaction zone faster than it is locally supplied by polymerization, and the front quenches immediately after initiation (**Figure 5.1c**, $\varphi \approx 0$). In either limiting case,

homogeneity is preserved in the system. However, when reaction and transport powers are similar in value ($\varphi \approx 1$), undulations in reaction temperature are observed (**Figure 5.1c**, φ = 0.4 or 0.5), indicating that frontal instabilities result from a competition between reaction and transport.

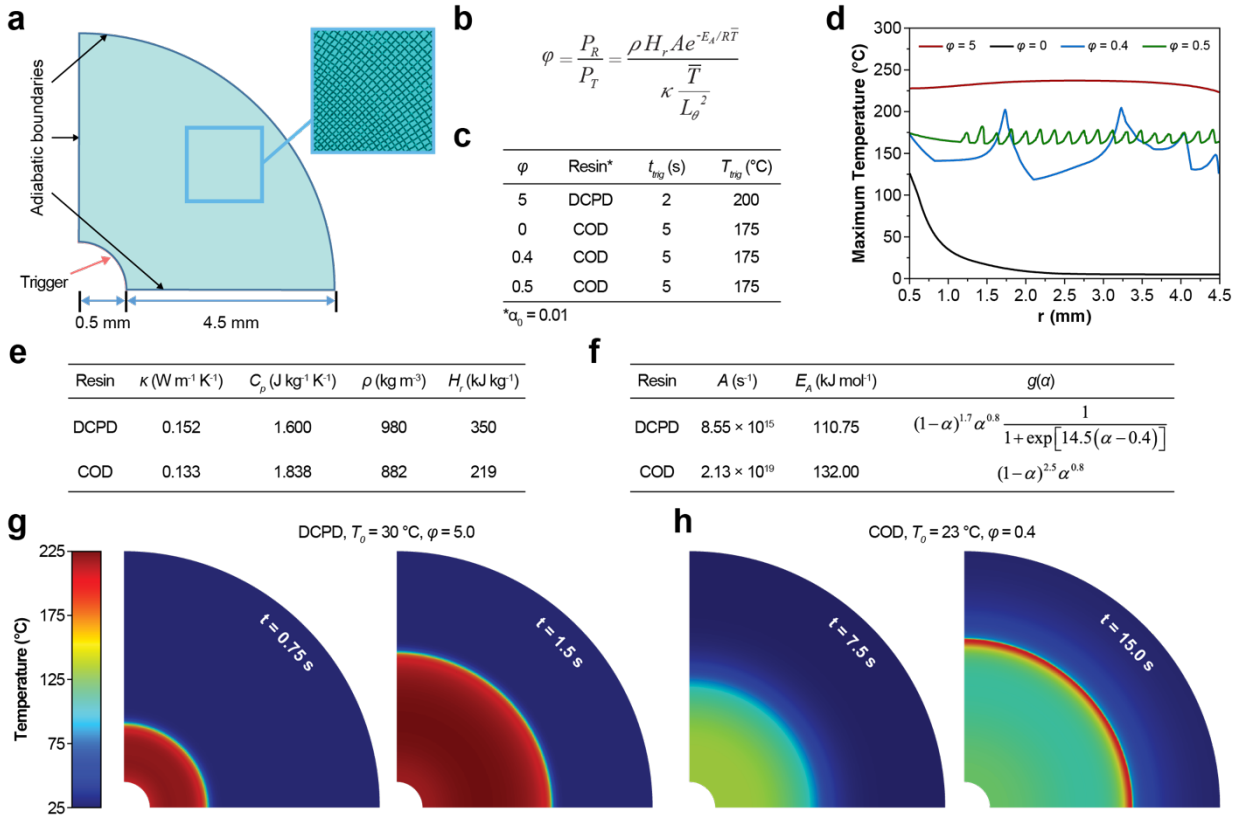

φ	Resin*	t_{trig} (s)	T_{trig} (°C)
5	DCPD	2	200
0	COD	5	175
0.4	COD	5	175
0.5	COD	5	175

*α_0 = 0.01

Resin	κ (W m^{-1} K^{-1})	C_p (J kg^{-1} K^{-1})	ρ (kg m^{-3})	H_r (kJ kg^{-1})
DCPD	0.152	1.600	980	350
COD	0.133	1.838	882	219

Resin	A (s^{-1})	E_A (kJ mol^{-1})	$g(\alpha)$
DCPD	8.55×10^{15}	110.75	$(1-\alpha)^{1.7}\alpha^{0.8}\frac{1}{1+\exp[14.5(\alpha-0.4)]}$
COD	2.13×10^{19}	132.00	$(1-\alpha)^{2.5}\alpha^{0.8}$

Figure 5.2. Numerical simulation of frontal polymerization | a, Schematic representation of the axisymmetric model of frontal polymerization in a quarter fan-shaped domain. Inset represents a schematic of the mesh utilized to discretize the domain. b, Ratio of power density (φ) generated by reaction (P_R) and spread by thermal transport (P_T) during frontal polymerization. ρ, H_r, A, E_A, R, $\bar{T}$, κ, and L_θ represent the density of the resin, heat of reaction, activation energy, universal gas constant, average of the maximum and initial temperature, and the width of the thermal front, respectively. c, Polymerization trigger conditions (expressed in terms of the temperature T_{trig} applied over a duration t_{trig}) used for various values of φ. d, Radial profiles of maximum temperature computed for various values of φ. e, Material properties of dicyclopentadiene and cyclooctadiene used in the computational models. f, Cure kinetic parameters obtained by fitting dynamic DSC traces. g, h, Evolution of the polymerization front in DCPD and COD.

Spontaneous patterning with a reaction-thermal transport process is summarized in **Figure 5.1d**. After an initial energy input, liquid monomer is converted to solid polymer with an accompanying release of energy (H_r, **Figure 5.1d**). The rapid transport (through diffusion, convection, or advection) of the energy supplied by the reaction (H_r) spontaneously heats

unreacted monomer, leading to local activation according to Arrhenius kinetics. Consumption of the activated monomer during polymerization depletes the latent chemical energy, preventing further activation by thermal transport. Following complete consumption of the activated monomer, propagation rates slow, transport becomes dominant again, and the process repeats cyclically to generate the undulations in reaction temperature shown in **Figure 5.1c**. In the absence of competition ($\varphi >> 1$), monomer is consumed before significant local activation occurs due to the greater reaction power and a homogenous final state is obtained. Conversely, as φ approaches zero, the heat from H_r is lost to the surroundings faster than it is supplied to the reaction, inhibiting the polymerization reaction and quenching fronts immediately after initiation.

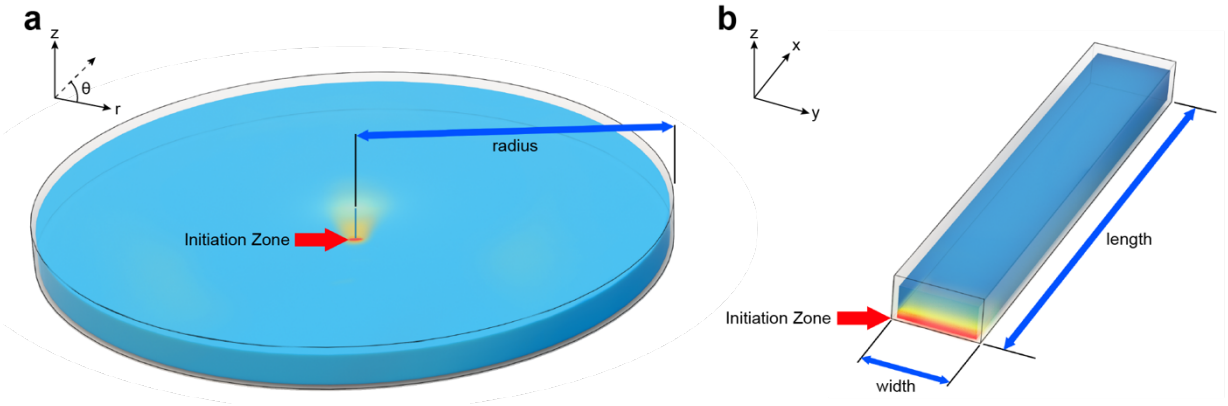

Figure 5.3 Experimental mold geometry | a, b, Schematic representation of cylindrical (a) and channel (b) molds. Initiation was achieved by powering a resistive wire in contact with the molds at the indicated locations.

Experimentally, we leverage the competition between reaction rate and thermal transport during the frontal ring-opening metathesis polymerization (FROMP) of dicyclopentadiene (DCPD) and 1,5-cyclooctadiene (COD) (**Figure 5.1e,f**) to break symmetry and generate emergent patterns. Competition between reaction rate and thermal transport is observed in an open-mold geometry with a free surface (**Figure 5.3**), which allows for increased rates of advective and convective transport[22] in addition to thermal diffusion. Precise control over this competition and the resulting temperature profiles are achieved by tuning the reaction rate through altering the

chemistry or the ambient temperature. Spatial variations in reaction temperature are exploited to drive changes in polymer morphology, chemistry, and mechanical properties.

5.3 Radial Patterning during FROMP of Dicyclopentadiene

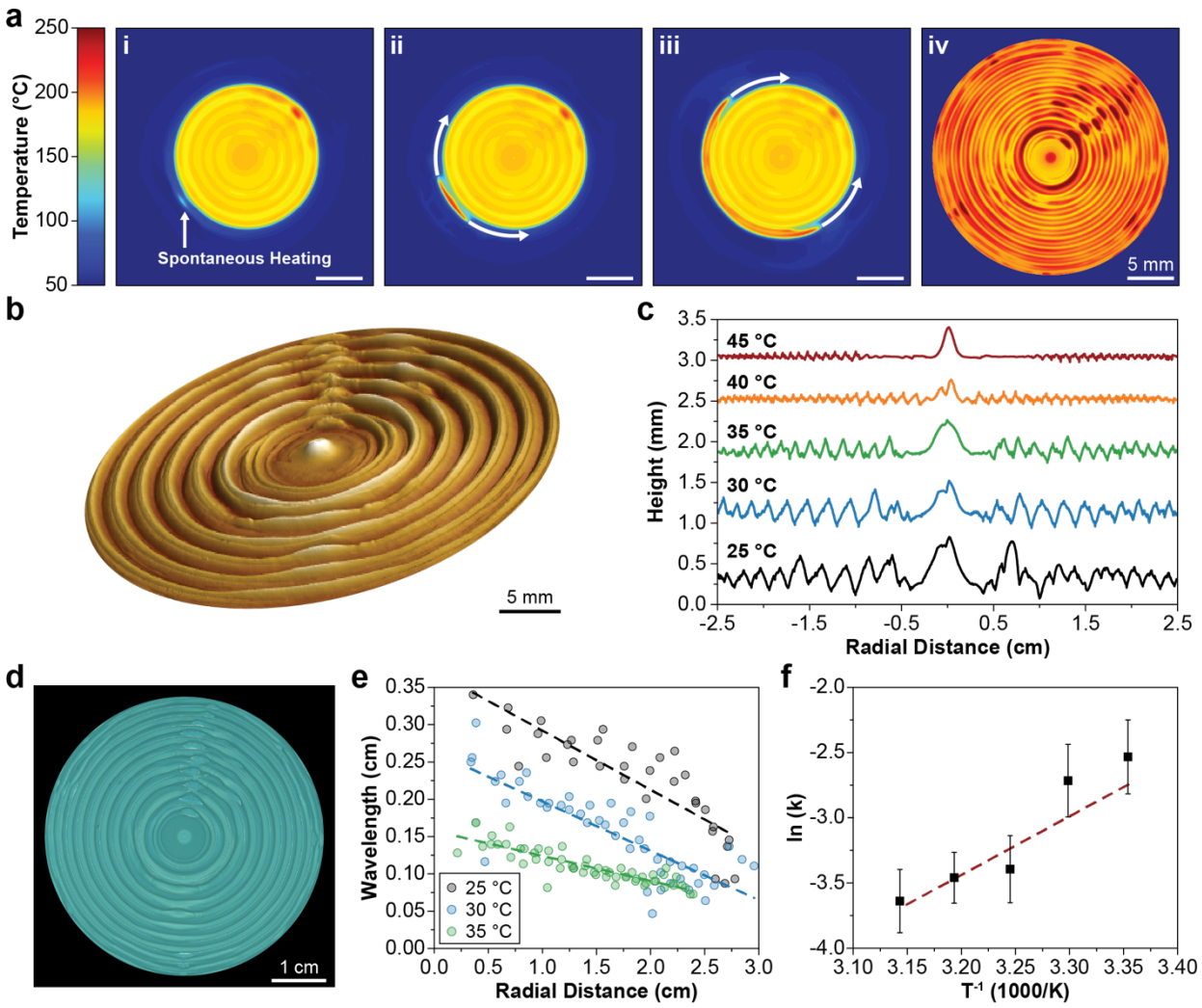

Figure 5.4. Radial patterning during FROMP of dicyclopentadiene | a, Thermal images revealing circumferential propagation in an open circular mold with an initial temperature of 30 °C: (i) spontaneous heating ahead of the polymerization front at t = 15s after initiation; (ii,iii) frontal propagation around the circumference following spontaneous heating; and (iv) maximum local temperature during polymerization. b, Topographic profile of sample shown in a, obtained by optical profilometry; the vertical axis is scaled by 150% for clarity. c, Surface height measurements of samples prepared with varied initial temperature. Profiles are offset for clarity. d, Optical image obtained under UV light (365 nm) of the sample in a; 0.25 wt% of 1,1,2,2-tetraphenylethylene was incorporated into the resin prior to frontal polymerization to enhance the fluorescence of resulting samples. e, Feature wavelength as a function of radial distance from the center of samples prepared with varied initial temperature, determined from optical images of fluorescent samples. f, Temperature dependence of the wavelength decay constant, obtained from the linear fit of wavelength vs. radial distance. Reported values and error bars represent the average and standard deviation, respectively (n = 3).

During free-surface FROMP of DCPD, thermal transport away from the reaction zone spontaneously heats a localized region of monomer ahead of the polymerization front (**Figure 5.4a,i**). Once this preheated region reaches ca. 80 °C, a new front initiates and propagates circumferentially, rapidly consuming the available preheated monomer (**Figure 5.4a,ii-iii**). The onset of initiation is in agreement with the polymerization onset temperature measured during dynamic DSC traces. Peak front temperatures as high as 270 °C and as low as 180 °C are recorded in circular patterns with radial periodicity (**Figure 5.4a,iv**). These undulations in reaction temperature lead to significant differences in thermal expansion of the liquid monomer, which is confined by the polymerization reaction, generating circumferential surface ridges (**Figure 5.4b,d**). Based on thermal expansion alone (assuming a coefficient of thermal expansion of 0.001 $°C^{-1}$,[36] and initial resin depth of 5 mm), a height difference of 450 μm is expected for a 90 °C difference in maximum reaction temperature, in good agreement with the experimentally measured maximum amplitude of 485 μm for an ambient temperature of 30 °C (**Figure 5.4b,c**).

The amplitude and wavelength of the ridges are systematically varied by adjusting the initial temperature of the resin immediately prior to initiation (**Figure 5.4c**). As the initial temperature increases, the undulations in reaction temperature damp (**Figure 5.5a**), leading to decreased differences in thermal expansion and smaller ridge amplitudes (**Figure 5.4c**). When the initial temperature reaches 50 °C, no undulations in reaction temperature were observed (**Figure 5.5a**), suggesting that P_R is greater than P_T. Additionally, the initial wavelength of the ridges, determined by analysis (**Figure 5.5b-e**) of fluorescent images of the samples (**Figure 5.4d**), decreases with increasing initial temperature. Interestingly, the pattern wavelength decays with radial distance (**Figure 5.4e**). Thermal imaging (**Figure 5.5f**) reveals that the unreacted monomer ahead of the front steadily increases in temperature, resulting in the subsequent decay in wavelength. This

temperature rise is likely due to advective motion induced by thermal expansion during polymerization. The zeroth-order wavelength decay constant, k (**Figure 5.4f**), is defined as the negative slope of the linear fits in **Figure 5.4e** and roughly follows Arrhenius behavior.

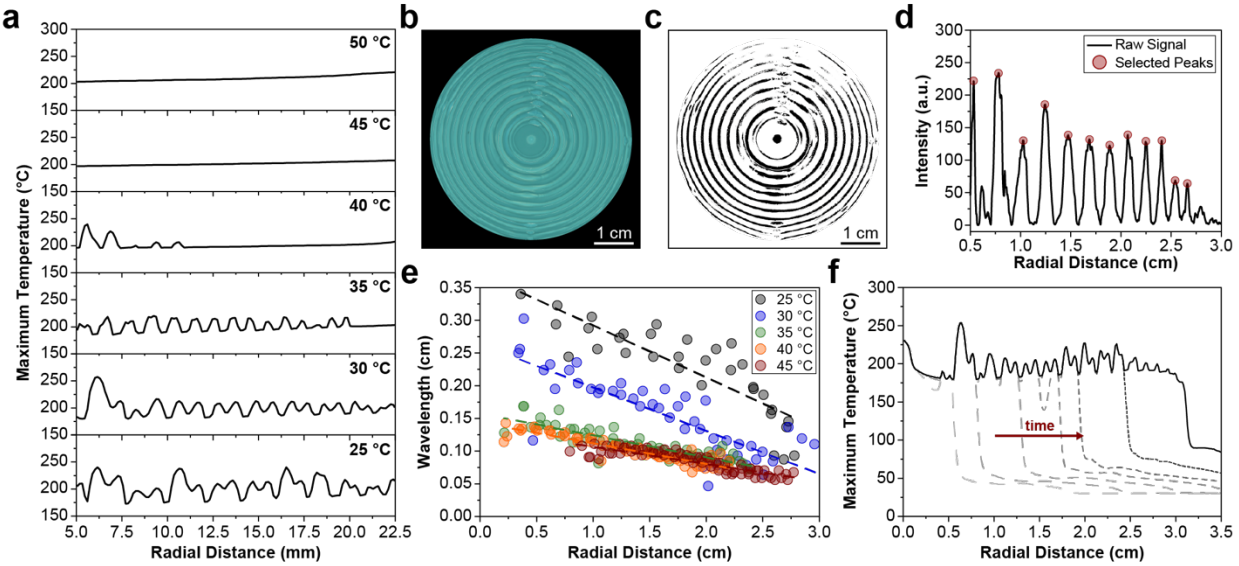

Figure 5.5. Characterization of DCPD circumferential propagation | a, Representative maximum temperature profiles obtained for various initial resin temperatures (T_0). Data represent measurements along a single radial line. b, Representative fluorescent image of a pDCPD sample (T_0 = 30 °C) used for wavelength analysis. c, Result of binary conversion, pixel erosion, and pixel dilation of the image depicted in b. d, Radial intensity profile of the binary image in c with the peaks selected to calculate the feature wavelength depicted in red. e, Feature wavelength as a function of radial distance at various initial temperatures. Both initial wavelength and the wavelength decay constant (defined as the slope of the linear fits) decrease with increasing initial temperature. f, Representative maximum temperature profiles at various time points after initiation. The temperature of the monomer ahead of the polymerization front steadily increases with increasing time, which contributes to the decay in feature wavelength.

5.4 Spontaneous Patterning with Phenylenediamine Thermochromes

To further explore the decay in wavelength and extend the length scale of study, we adopted a rectangular channel geometry (**Figure 5.3b**). Free-surface FROMP of DCPD in a channel results in similar circumferential propagation as in radial geometries. As the wavelength of circumferential propagation tends toward zero, a large zone (~1 cm) of heated monomer accumulates spontaneously ahead of the front (**Figure 5.6a,i**). Analogous to the short-range experiments in radial geometries, this large preheated zone is subsequently consumed in a rapid, high temperature polymerization reaction that exceeds 270 °C (**Figure 5.6a,ii**). Following the

consumption of all of the available preheated monomer, reaction rates slow, and reaction temperatures decrease to around 200 °C. This process repeats cyclically to generate the striped thermal profiles shown in **Figure 5.6a,iii**. The size and the spacing of the features are controlled by varying the initial temperature, again demonstrating the utility of tuning the boundary conditions to generate distinct thermal profiles (**Figure 5.7**).

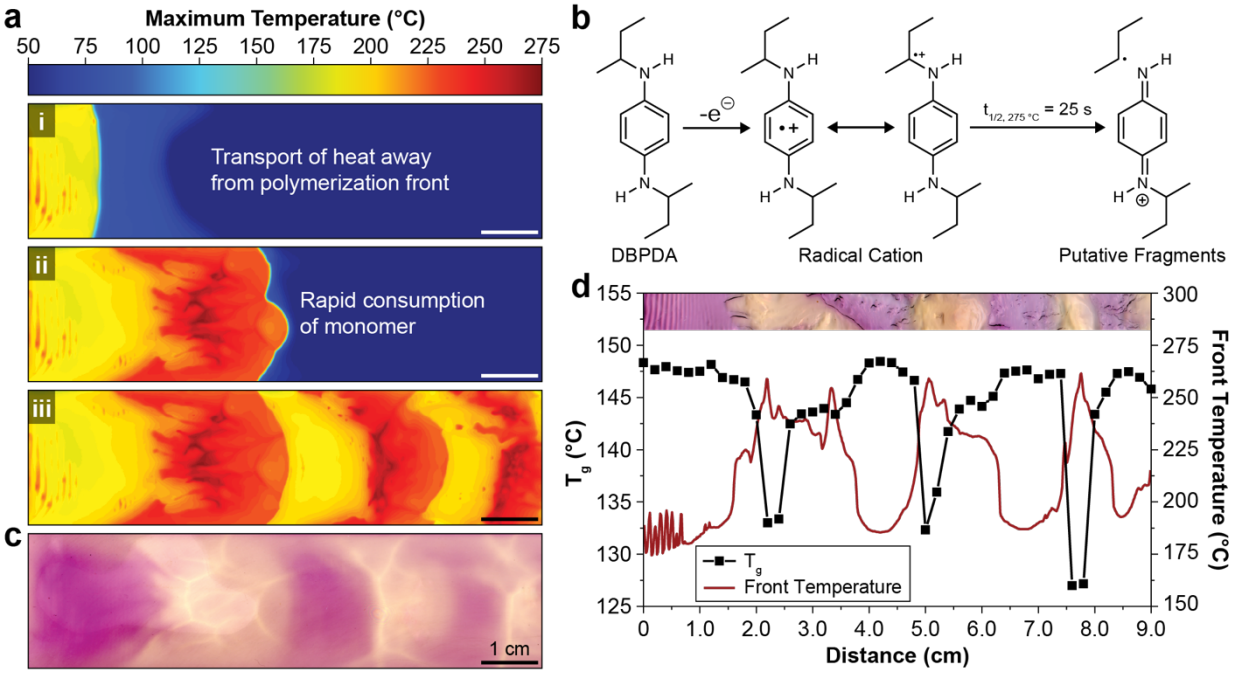

Figure 5.6. Color patterning with a thermochrome | a, Evolution of maximum temperature profiles during FROMP of DCPD in a rectangular channel: (i) a zone of spontaneously heated monomer, (ii) rapid, high temperature polymerization encountered during consumption of the preheated monomer, and (iii) large thermal gradients encountered during unstable propagation. Scale bar = 1cm. b, Putative single electron transfer oxidation of DBPDA to form a highly colored and stable radical cation and subsequent temperature-dependent cleavage of the radical cation to form colorless species. Reported half-life determined during ex situ bleaching at 275 °C (**Figure 5.8**). c, Optical image of the sample after the frontal polymerization in a; 2 wt% DBPDA was incorporated into the resin prior to frontal polymerization (sample was polished to remove surface features and enhance visualization of the DBPDA thermochrome). d, Glass transition temperature (T_g, determined by DSC analysis) and maximum front temperature as a function of distance from the initiation location for a polymerized sample containing 2 wt% DBPDA. Inset is an optical image of the tested sample.

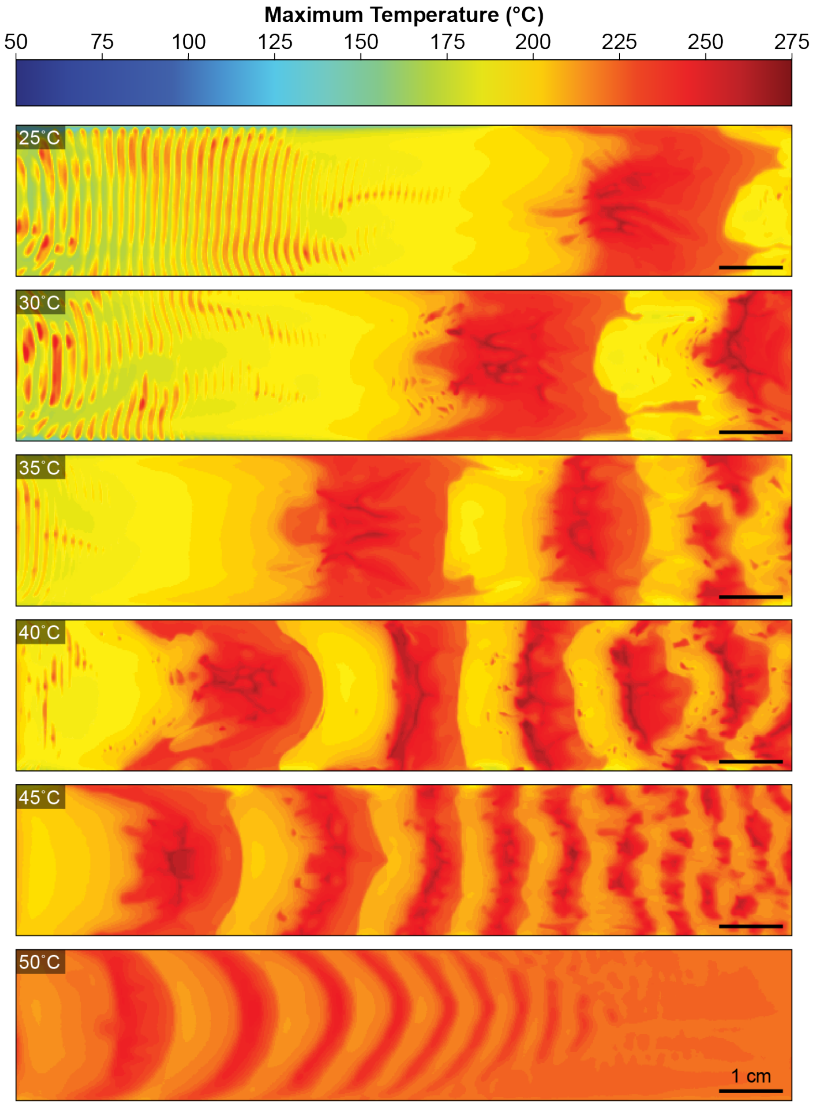

Figure 5.7. Tuning of thermal profiles during free-surface FROMP of DCPD | Maximum temperature profiles obtained with various initial resin temperatures. Feature size and spacing decrease with increasing initial resin temperature.

The presence of large, spatially defined regions of high and low reaction temperatures provides an opportunity to produce permanent patterns by the application of a secondary chemical reaction, the rate of which varies widely over the observed range of peak temperatures. Specifically, the incorporation of a phenylenediamine-based thermochrome enables patterning of the optical and thermomechanical properties of pDCPD. Substituted phenylenediamines, such as *N,N'*-di-*sec*-butyl-*p*-phenylenediamine (DBPDA), readily undergo single electron transfer oxidation ($E_{OX} \approx$

0.2 V vs. SCE[37]) to form stable and highly colored radical cations, known as Wüster's dyes (**Figure 5.6b**).[38] We postulate that while stable at modest temperatures, the radical cations undergo mesolytic cleavage at high temperature to form colorless species. When DBPDA is incorporated into DCPD resins cured at room temperature, we observe a slow transition from faint red to deep purple over the course of several hours, indicating formation of radical cation species in the presence of Grubbs catalyst 2nd generation (GC2) (**Figure 5.8b,c**). The presence of DBPDA (2 wt%) has minimal impact on frontal propagation; resins with DBPDA exhibit nearly identical front velocities to those without DBPDA (**Figure 5.8d**). Importantly, the deep purple color is retained at modest front temperatures, ca. 200 °C. Heating the resulting samples on a hot stage at temperatures in excess of 250 °C results in rapid ($t_{1/2}$ = 25 s at 275 °C), complete, and irreversible bleaching to the innate color of pDCPD, supporting our conjecture that the radical cation dye serves as a permanent thermochrome (**Figure 5.8e,f**).

In addition to *ex situ* bleaching, DBPDA displays highly selective thermochromism *in situ*, enabling a permanent visual indication of the local front temperature (**Figure 5.6c**). Decay of the radical cation results in visible bleaching at front temperatures near 250 °C, and bleaching increases with increasing front temperature, up to ca. 270 °C. The decay of radical cations may generate reaction byproducts, altering the thermomechanical properties of the resulting polymer. Indeed, the bleached regions exhibit a 20 °C decrease in the glass transition temperature (T_g) compared to the unbleached regions (**Figure 5.6d**). The undulations in T_g correlate to trends in both bleaching and front temperature. In the absence of DBPDA, a similar thermal profile is obtained, but only a modest 8 °C change in T_g is observed, indicating that DBPDA reaction products are responsible for the changes in thermomechanical properties.

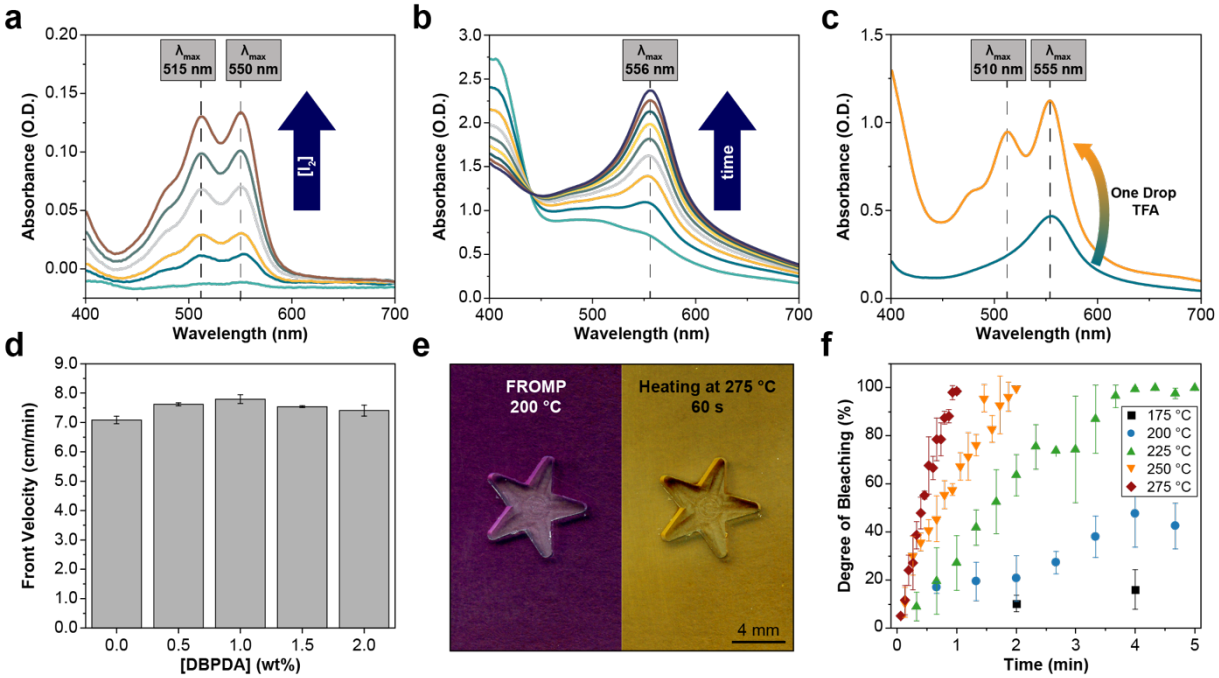

Figure 5.8. Characterization of DBPDA thermochromes | a, UV-Vis absorption spectra of DBPDA treated with increasing amounts of iodine in dichloromethane, showing the characteristic absorption spectrum of the p-phenylenediamine radical cation2,3. b, Evolution of the absorption spectra (obtained at 2 min intervals) of DBPDA treated with 0.075 molar equivalents of Grubbs catalyst 2nd generation (GC2) in dichloromethane. c, Absorption spectrum obtained after treatment of a solution of DBPDA and GC2 in dichloromethane with a single drop of trifluoroacetic acid (TFA), demonstrating clean formation of the DBPDA radical cation. It is believed that GC2 facilitates the formation of a DBPDA radical cation dimer, which is disrupted by the addition of acid. d, Front velocities obtained with various concentrations of DBPDA. The presence of DBPDA has minimal impact on frontal propagation. e, Optical images of a sample loaded with 2 wt% DBPDA after frontal propagation in a mold with a star shaped projection at 200 °C (temperature confirmed with a thermocouple submerged in resin) (left) and after heating on a metal substrate maintained at 275 °C for 60 s. The presence of a deep purple color is indicative of radical cation formation during mild temperature front propagation, while the return to the native yellow color of pDCPD is suggestive of radical cation fragmentation to colorless species. f, Ex situ bleaching of pDCPD samples containing 2 wt% DBPDA after heating on a hot stage at the indicated temperature. Degree of bleaching was determined by analyzing the yellow channel of optical images of the heated samples. Rapid bleaching is observed at temperatures in excess of 250 °C.

5.5 Mechanical Patterning During FROMP of Cyclooctadiene

While the DCPD-DBPDA system exhibits interesting optical and thermomechanical patterning, we sought to apply this concept to other materials. Inspired by the impressive fracture toughness that results from patterning hard and soft domains, which differ in stiffness by several orders of magnitude in biological materials such as glass sea sponges[1]and nacre[3], we targeted material systems that would generate significant differences in material stiffness in response to

front temperature. We recently demonstrated that frontally polymerized 1,5-cyclooctadiene (COD) has a propensity to crystallize due to high *trans* content.[39] We suspected that the *cis/trans* ratio would vary with reaction temperature, resulting in patterned regions of amorphous and crystalline material. During free-surface FROMP of COD, we observe significant thermal transport ahead of the reaction zone, generating a large region of heated monomer, which upon initiation (at ca. 70 °C) is rapidly consumed in a high temperature polymerization reaction. As with the DCPD systems, this process repeats cyclically until all monomer is consumed (**Figure 5.9a**, top image).

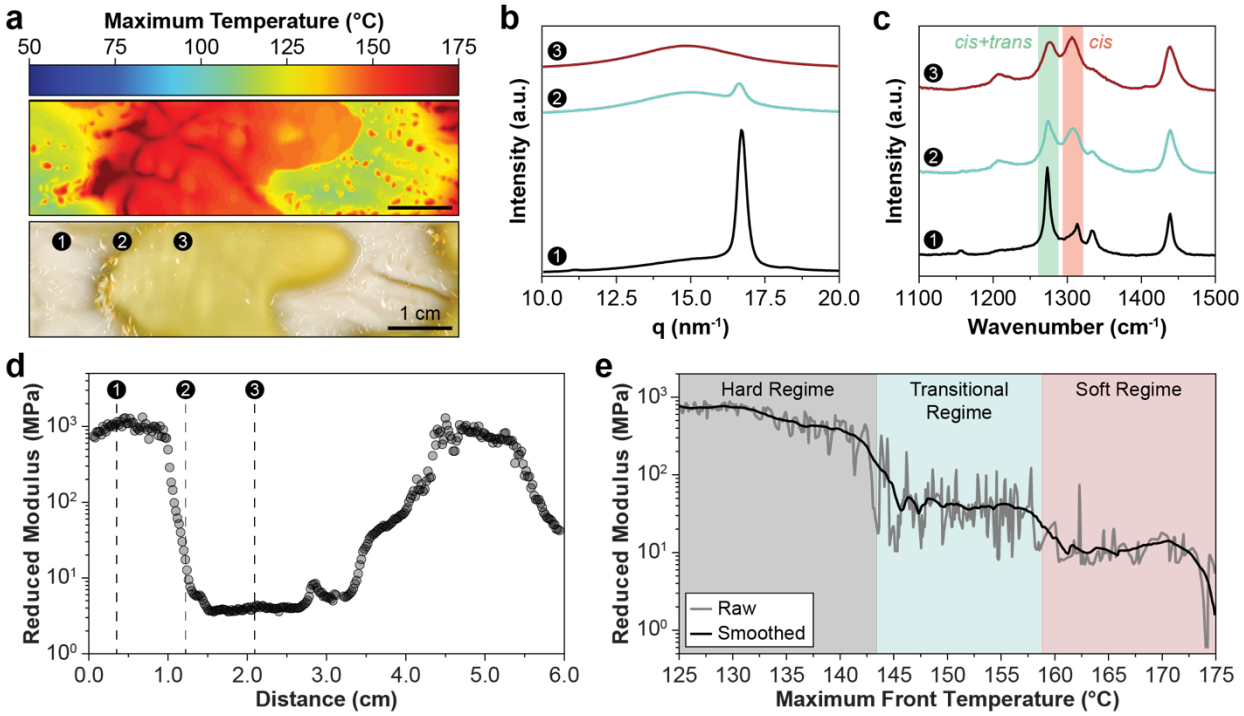

Figure 5.9. Spontaneous patterning with cyclooctadiene | a, Maximum temperature profile during free-surface FROMP of 1,5-cyclooctadiene (top) and optical image (bottom) of the resulting pattern showing crystalline (white) and amorphous (yellow) domains. The numbered markers represent measurement locations in subsequent characterization. b, WAXS profiles obtained at the locations indicated in a. c, Raman spectra obtained at the locations indicated in a. d, Reduced modulus as a function of distance from the initiation point obtained via nanoindentation. The indentation profile follows the same trajectory as the numbered locations in a. e, Reduced modulus as a function of maximum front temperature obtained through spatial correlation of nanoindentation scans and thermal profiles. The smoothed curve (black) was obtained from adjacent averaging 100 points of raw data (grey).

After polymerization, the sample is cooled and held at room temperature for 24 h. During this time, the areas that experienced low front temperatures (ca. 120 °C) crystallize to form a white

opaque material (**Figure 5.9a**, bottom image), while regions with front temperatures greater than 145 °C remain a transparent yellow. Wide-angle X-ray scattering (WAXS) analysis of the white opaque material shows a sharp peak centered at 16.5 nm^{-1} (**Figure 5.9b**, region 1), confirming the presence of crystalline pCOD domains. The intensity of the crystalline peak decreases significantly through the transition region (**Figure 5.9b**, region 2), until only an amorphous halo remains (**Figure 5.9b**, region 3), indicating a fully amorphous phase. Raman spectroscopy of region 1 (**Figure 5.9c**) indicates high *trans* content in the crystalline domains.[40] The high *trans* content suggests that chain transfer is rapid on the timescale of frontal polymerization. In regions with higher peak temperatures, a mixture of *cis* and *trans* pCOD is produced (**Figure 5.9c**, regions 2 and 3), indicating either that *trans*-selectivity of the chain transfer reaction decreases above 145 °C or that polymerization kinetics become competitive with chain transfer at higher temperature. The *trans* content of the crystalline and amorphous domains as measured by ^{1}H NMR is 88% and 76%, respectively. Additionally, we observe that the amorphous domains are only partially soluble, suggesting some degree of crosslinking, possibly a result of radical formation at high temperatures. Together, the higher *cis* content and crosslinking contribute to the formation of an amorphous domain.

The temperature-responsive crystallization of pCOD yields our target result: spontaneously patterned materials with hard and soft domains. The changes in stiffness between the crystalline and amorphous domains are measured by nanoindentation. The reduced modulus varies by several orders of magnitude, reaching a maximum of 1.3 GPa and a minimum of 3 MPa in a representative example (**Figure 5.9d**). The stiffness correlates well with the physical characteristics, spectroscopic properties, and the maximum front temperature, where higher front temperature results in lower stiffness. Correlation between front temperature and stiffness reveal three distinct

stiffness regimes (**Figure 5.9e**): (1) a hard domain with moduli ranging from 200 MPa to 1 GPa, where front temperatures remain less than 143 °C; (2) a transitional domain with moduli near 30 MPa; and (3) a soft domain with moduli of approximately 5 MPa, where front temperatures remain above 160 °C. The relationship between stiffness and front temperature is a key design principle when developing patterns for engineering applications.

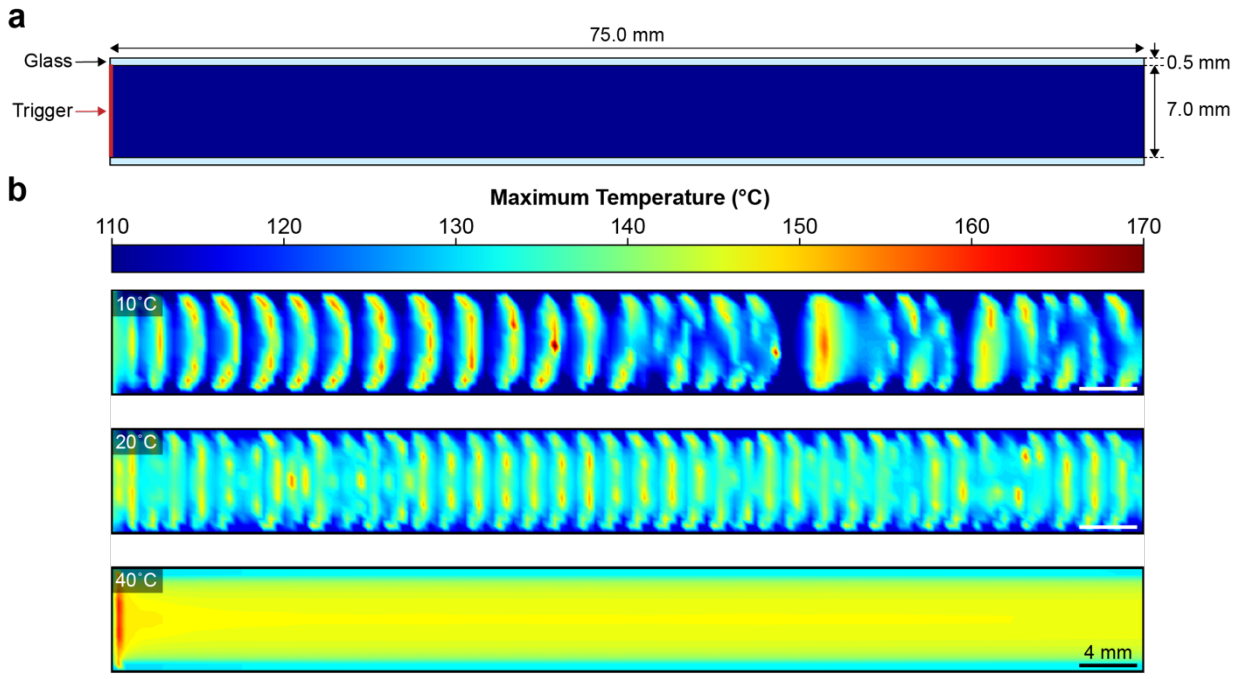

Figure 5.10. Numerical simulation of COD frontal polymerization in a channel geometry | a, Schematic representation of the frontal polymerization in a channel domain with glass boundaries. b, Maximum temperature profiles obtained with various initial resin temperatures. The solution of the reaction-diffusion equations captures the FP-induced thermal instabilities and the resulting pattern complexity that decreases with increasing initial resin temperature.

The low ring-strain of cyclooctadiene limits P_R generated during the ring-opening reaction, leading to a system that displays a weak, transport-dominated imbalance. As a result, pattern control with COD was significantly more challenging than with DCPD. To address this issue, future work will center on measuring the thermal expansion driven advection associated with free-surface FROMP and development of strategies to accurately modulate and predict thermal transport. Further, we anticipate that modification of boundary conditions may enable

spatiotemporal control of the resin temperature and produce more highly controlled patterns such as those predicted in **Figure 5.10**.

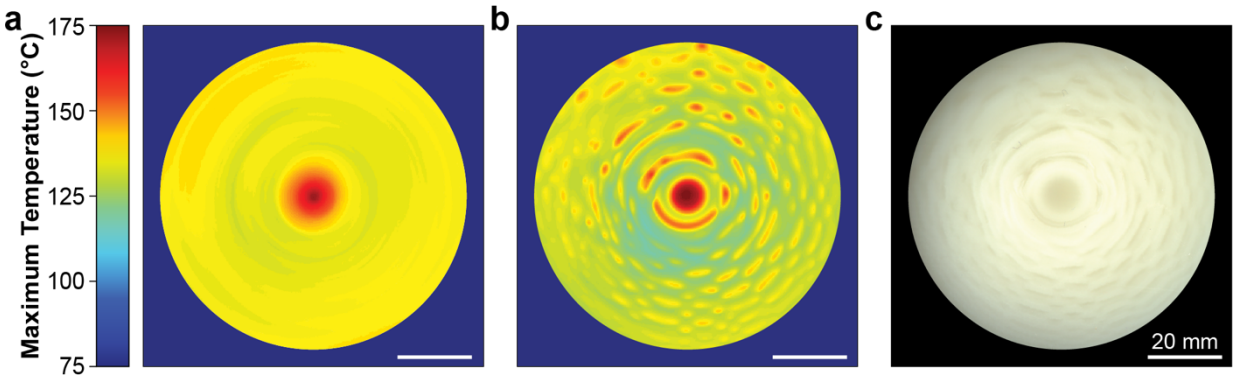

Figure 5.11. Controlling instabilities during free-surface FROMP of COD | a, Maximum temperature profile obtained after adding 5 wt % PBD to COD resins (100 ppm GC2). b, Maximum temperature profile obtained after reducing the catalyst concentration to 50 ppm. The high temperature region at the center of the samples in a and b is a result resistive heating during initiation. c, Optical image acquired after aging the sample depicted in b for 12 h at room temperature. White, opaque regions represent crystalline domains, and the clear, faint yellow regions represent amorphous domains.

A key element of producing more controlled patterns with COD is to control the thermal transport during frontal polymerization. To suppress advective transport during free-surface FROMP (decrease in P_T and increase in φ), the viscosity of COD resins is increased by dissolving commercial *cis*-polybutadiene (PBD) into COD prior to the addition of catalyst and inhibitor. At 2.5 wt% PBD, minimal preheating of the monomer ahead of the polymerization front was observed, suggesting a significant reduction in advective transport. However, unstable fronts which resemble a Rayleigh-Taylor instability[41] are observed. Increasing PBD content to 5 wt% yields stable propagation and a uniform thermal profile (**Figure 5.11a**), indicative of a value of P_R much greater than P_T.

In the absence of advective transport, the competition between reaction and transport which yields patterned thermal profiles is easily tuned by adjusting the reaction kinetics. Propagation instabilities are introduced by reducing reaction rates (reducing P_R) such that $\varphi \approx 1$. Reducing the catalyst concentration from 100 ppm to 50 ppm results in well controlled radial patterns (**Figure**

5.11b) that are similar to those obtained with DCPD (**Figure 5.4**). Unfortunately, the reduced reaction rate generates smaller differences in temperature (ca. 40 °C) on a much smaller size scale than those in **Figure 5.9a**. As a result, the differences between amorphous and crystalline regions are much less pronounced (**Figure 5.11c**). Therefore, future work will need to explore the spatiotemporal dependence of crystallization on temperature. Importantly, the minimum scale at which amorphous domains form within crystalline domains in response to thermal spikes must be investigated to determine if this approach is a viable method to produce the micro- and nano-scale patterning that leads to increased toughness in biological materials[1,3]. Further, other cyclic olefins that are capable of generating crystalline thermoplastics upon polymerization must be developed to expand the library of available material properties.

5.6 Conclusions

We have demonstrated that thermally driven reaction-transport during frontal polymerization produces spontaneous patterns in structural materials. Patterning of surface morphology, color, and T_g was realized in pDCPD resins. Control of boundary conditions such as the initial temperature of the monomer enabled fine-tuning of pattern development and evolution. Application of this patterning technique to frontal polymerization of COD resulted in materials with clearly defined regions varying more than two orders of magnitude in stiffness. The ability to create and control large thermal gradients creates opportunities for new chemical and physical transformations in response to temperature such as liquid crystal mesogens, thermochromes, catalyst inhibition schemes, and crosslinking reactions. Provided that the transformation kinetics are competitive with frontal polymerization, we anticipate that this patterning strategy can be combined with the wide variety of thermally responsive materials and chemistries that have been developed to date.

The reaction-thermal transport processes of frontal polymerization are akin to the reaction-mass transport processes in Turing's model of biological morphogenesis (*5*), and we envision that our results will form the foundation of a synthetic analogue to biological development. These fundamental findings in polymer science are expected to have significant impacts on the design and manufacture of macroscale functional materials, and the creation of developmental materials will be a paradigm shift in polymer manufacturing, enabling the autonomous growth of structures and patterns.

5.7 Experimental Details

5.7.1 Numerical Simulations

Frontal polymerization in a two-dimensional concentric fan-shape domain (**Figure 5.1b**) and in a two-dimensional channel (**Figure 5.10**) was modeled by solving the following partial differential equations:

$$\begin{cases} \kappa\nabla^2 T + \rho H_r \dfrac{\partial \alpha}{\partial t} = \rho C_p \dfrac{\partial T}{\partial t} \\ \dfrac{\partial \alpha}{\partial t} = A\exp\left(-\dfrac{E_A}{RT}\right) g(\alpha) \end{cases}$$

The variables of interest are the temperature T (K) and the degree of cure α (non-dimensional), both evolving with time and position. The first equation describes thermal conservation with the power density transported by diffusion ($\kappa\nabla^2 T$) and the power density generated by polymerization ($\rho H_r \frac{\partial \alpha}{\partial t}$). The associated material properties are the thermal conductivity, κ (W m^{-1} K^{-1}); the specific heat capacity, C_p (J kg^{-1} K^{-1}); the density, ρ (kg m^{-3}); and the heat of reaction, H_r (J kg^{-1}). The second equation models the cure kinetics of the considered material, where the parameters (pre-exponential factor, A (s^{-1}); activation energy E_A (J mol^{-1}); and the evolution of the degree of cure, $g(\alpha)$) are determined by performing nonlinear fitting optimization with the data obtained

from dynamics DSC tests performed on the resins. R (8.314 J mol^{-1} K^{-1}) represents the ideal gas constant.

The initial and boundary conditions used to solve the governing equations in the adiabatic fan-shape domain are:

$$\begin{cases} T(r,\theta,0) = T_0 \\ \alpha(r,\theta,0) = \alpha_0 \\ T(r_0,\theta,t) = T_{trig} \quad 0 < t \le t_{trig} \\ \dfrac{\partial T}{\partial r}(r_0,\theta,t) = 0 \quad t > t_{trig} \end{cases}$$

where T_0, α_0, T_{trig} and r_0 are the initial temperature, initial degree of cure, triggering temperature and the inner radius of the fan-shape domain. **Figure 5.2a** depicts the initial mesh adopted for the finite element analysis. The inner and outer radii of the domain were 0.5 and 5.0 mm, respectively. 11,712 four-node quadrilateral elements uniformly distributed in the angular direction were used to discretize the domain at the beginning of the simulation, and a maximum refinement level of 5 was applied to adapt the mesh and capture the sharp gradients in T and α in the vicinity of the advancing front.

In the channel with glass boundaries (**Figure 5.10a**), the governing equations were solved in two sub-domains. The first sub-domain, where no chemical reaction is considered, consisted of glass with C_p = 840 J kg^{-1} K^{-1}, ρ = 2500 kg m^{-3}, κ = 1.14 W m^{-1} K^{-1}, and H_r = 0 J kg^{-1}. The second sub-domain consisted of cyclooctadiene resin. The initial and boundary conditions are described as follows:

$$\begin{cases} T(x,y,0) = T_0 \\ \alpha(x,y,0) = \alpha_0 \\ T(x_0,y,t) = T_{trig} \quad 0 < t \le t_{trig} \\ \dfrac{\partial T}{\partial x}(x_0,y,t) = 0 \quad t > t_{trig} \end{cases}$$

where $x_0 = 0$ represents the left boundary of the channel where polymerization is triggered. Since there is no chemical reaction in the glass, only thermal diffusion is considered in this subdomain. The domain (**Figure 5.10a**), representing the top view of an adiabatic channel, is 75mm long and 7mm width with additional 0.5mm of glass at top and bottom boundaries. The overall domain is divided into 32,000 four-node quadrilateral elements with a maximum refinement level of 3 near the front vicinity.

The numerical analysis was conducted using the Multiphysics Object-Oriented Simulation Environment (MOOSE)[42], an open source C++ finite element solver that includes robust mesh adaptivity capability. The implicit Euler time stepping scheme and a preconditioned Jacobian-free Newton-Krylov method were adopted to solve the transient, nonlinear equations.[43,44] The ratio of power densities, φ, was computed as follows:

$$\varphi = \frac{P_R}{P_T} = \frac{\rho H_r A e^{-E_A/R\bar{T}}}{\kappa \frac{\bar{T}}{L_\theta{}^2}}$$

where $\bar{T}$ and L_θ represent the average of the initial and maximum temperature and the width of the thermal front, respectively. Parameters for computing the cases discussed in **Figure 5.1b** and **Figure 5.10** are summarized in **Figure 5.2c,e,f**.

Figure 5.2d shows the radial variation of the maximum temperature, T_{max}, predicted by numerical analysis, which is a quantitative description of **Figure 5.1b**. When $\varphi \approx 0$, frontal polymerization is unable to initiate, and T_{max} decreases from T_{trig} to T_0 as r increases. When φ = 0.4, several peaks of T_{max} at different r are obtained, reflecting the unstable propagation of the front. The magnitude and wavelength of the peaks in T_{max} decreases when φ = 0.5, indicating an increase in stability. At φ = 5, no peaks in T_{max} are observed, indicating stable front propagation. **Figure 5.2g,h** demonstrate snapshots of numerical simulation of stable and unstable front

propagation, respectively. **Figure 5.10b** shows the maximum temperature profiles computed for COD when the front propagates in a long glass channel. The symmetry of frontal propagation and the resulting pattern size, spacing, and shape are readily tuned by varying the initial temperature of the resin, T_0. At high initial temperatures, e.g. T_0 = 40 °C, fronts propagate in a steady fashion, and the resulting temperature profile is homogeneous. At reduced initial temperatures, e.g. $T_0 \leq$ 20 °C, propagating fronts display symmetry breaking events, leading to striped patterns that increase in complexity with distance from the initiation point.

5.7.2 Materials

Dicyclopentadiene (DCPD), 5-ethylidene-2-norbornene (ENB), Grubbs catalyst 2nd generation (GC2), tributyl phosphite (TBP), 1,1,2,2-tetraphenylethylene (TPE), and *cis*-polybutadiene (M_w = 200,000 – 300,000 Da) were purchased from Sigma-Aldrich and used without further purification. TBP was stored under inert atmosphere to prevent hydrolysis of the phosphite. 1,5-cyclooctadiene (COD) and *N,N'*-di-*sec*-butyl-*p*-phenylenediamine (DBPDA) were purchased from TCI America. DBPDA was used as received and stored under inert atmosphere. COD was passed through a 1 cm plug of basic alumina to remove the octadecyl 3-(3',5'-di-*tert*-butyl-4'-hydroxylphenyl)propionate stabilizer which was found to interact negatively with GC2, preventing frontal polymerization. RTV630 silicone rubber compound was purchased from Momentive® and used as received. 26-gauge Kanthal wire (D = 0.40 mm, resistivity = 1.4×10^{-4} Ω cm) was used to initiate FROMP. Polyurethane rubber gaskets, laminated glass plates, and aluminum plates were purchased from McMaster-Carr.

5.7.3 Free-Surface Frontal Ring-Opening Metathesis Polymerization

To depress the freezing point of DCPD, 5 wt% ENB was blended with DCPD at 35 °C. The liquid mixture was then degassed overnight at room temperature and 15 kPa with stirring. Unless otherwise noted, all references to DCPD refer to the 95:5 DCPD:ENB mixture. To enhance the fluorescence and aid in visualization of radial samples, 0.25 wt% TPE was dissolved in DCPD and degassed for an additional 12 h at room temperature and 15 kPa. In a typical experiment, 30 mg GC2 (0.0353 mmol) was weighed out in a vial. In a separate container, TBP (9.6 μL, 0.0353 mmol) was added to DCPD (46.6 g, 10,000 molar equivalents to GC2) or COD (38.4 g, 10,000 molar equivalents to GC2). The monomer/inhibitor solution was then added to the vial containing GC2, and the resulting mixture was sonicated for 10 min to ensure complete dissolution of GC2. The solution was then filtered through a 0.22 μm PVDF membrane to remove any particulates. Filtered solutions were added to either a radial or channel mold to give a resin depth of 5 mm and incubated until the desired initial monomer temperature was achieved. Frontal polymerization was then initiated by local heating with a resistive wire. Polymerized samples were stored under a continuous flow of nitrogen gas to prevent surface oxidation.

Radial (D = 100 mm) and channel (150 mm × 25 mm) molds were fabricated by compressing an 8 mm thick polyurethane rubber gasket, cut into the desired geometry by waterjet, between a 1 mm thick laminated glass plate and a 3 mm thick aluminum plate. The top aluminum plate was machined to match the geometry of the rubber gasket and coated with Krylon ultra-flat black spray paint prior to assembly to simulate a black body during thermal imaging. Initiation was achieved by heating a portion of the mold surface at 200 °C for 5 s with a resistive heater. Radial molds were heated in the center ($D_{initiation}$ = 3.0 mm), and channel molds were heated along one 25 mm edge. Schematics of the molds and initiation schemes employed for individual experiments are

summarized in Error! Reference source not found.. Front temperatures were monitored from o verhead with a FLIR T1020 thermal infrared camera focused at the liquid surface. The initial resin temperature and the ambient temperature were maintained in a custom-built environmental chamber equipped with an AC-162 Peltier module, TC-720 temperature controller, and PS-24-25 power supply from TE Technology, Inc. Resin temperature was monitored with a thermocouple and the overhead infrared camera.

5.7.4 Materials Characterization

3D surface profiles as shown in **Figure 5.4b** were obtained with a Keyence VK-X1000 3D Laser Scanning Confocal Microscope equipped with a 5× objective and 405 nm laser. Due to the fluorescence of polymerized samples, inverse molds of the circumferential ridges were generated by casting degassed silicone resin onto the sample surface and curing for 24 h at room temperature and 1 h at 100 °C. Surface profiles of the silicone molds were then inverted to quantify the pDCPD surface.

Differential scanning calorimetry (DSC) traces were obtained with a Discovery 250 DSC equipped with an RCS 90 cooling system and an autosampler. Disks (D = 1.5 mm) were punched from the samples at 2 mm intervals, weighed on an analytical balance (XPE205, Mettler-Toledo), and transferred to Tzero® aluminum pans. Traces were obtained between 25 °C and 250 °C at 10 °C min^{-1}. Glass transition temperatures were defined as the inflection point in DSC traces. Dynamic curing traces were obtained for 2-3 mg samples of freshly prepared resin sealed in Tzero® aluminum pans with hermetic lids. Traces were obtained between -50 °C and 250 °C at various ramp rates.

Nanoindentation was performed with a Hysitron TI-950 TriboIndenter equipped with a Hysitron 3D Omniprobe™ high load transducer and Berkovich tip from Bruker. Samples were

loaded at 3 mN s^{-1} up to a maximum load of 15 mN, which was held for 2 s, and subsequently unloaded at 3 mN s^{-1}. Reduced moduli were extracted from the unloading curves utilizing the Oliver-Pharr method[45]. Prior to indentation, samples were ground and polished to ensure a uniform surface on a MetPrep 3 polisher from Allied High Tech Products, Inc, equipped with a series of silicon carbide grinding papers (with a minimum grit of 1200) from Buehler.

Raman spectra were obtained with a Horiba LabRAM HR 3D Raman confocal imaging microscope equipped with an 830 nm laser, a 300 groove mm^{-1} grating (blazed at 600 nm), a long working distance 20× objective from Leica, and a Horiba Synapse back-illuminated deep depletion CCD camera. ^{1}H NMR spectra were obtained in chloroform-*d* with a Carver 500 MHz spectrometer provided by the School of Chemical Sciences NMR laboratory at the University of Illinois at Urbana-Champaign. UV-Vis spectra were obtained with a Shimadzu UV-2401PC spectrometer and quartz cuvettes purchased from Starna Cells.

Transmission wide-angle X-ray scattering was conducted with a Xenocs GeniX3D Cu Kα X-ray source (1.54 Å) and a Pilatus 2D detector. A rod beam stop placed in front of the detector was used to attenuate the primary beam, and the sample-to-detector distance was calibrated with silver behenate powder. Scattering patterns were collected with a 10-minute exposure time under ambient conditions. The 2D diffraction data were radially averaged using FIT2D software and the intensity was plotted as a function of scattering vector q.

Ex situ bleaching of DBPDA was evaluated in pDCPD panels containing 2 wt% DBPDA. The panels were prepared by pouring DCPD resin containing 2 wt% DBPDA into cell casting molds (t = 1.0 mm) and allowing the samples to cure for three days at room temperature. Disks (D = 5.0 mm) were punched from the panels and placed on a Linkam THMS600 heating stage which was preheated to the desired temperature. The disks were then imaged optically, and the intensity of

the yellow channel was averaged over the sample area. The degree of bleaching was calculated according to the following relation:

$$\text{Degree of Bleaching (\%)} = \frac{I_0 - I_t}{I_0} \times 100\%$$

where I_0 and I_t represent the average intensity of the yellow channel prior to and after thermal treatment, respectively.

5.7.5 Image Analysis

All image analysis was performed using FIJI (ImageJ 1.49v). The wave features of radial (D = 100 mm) pDCPD samples were analyzed by converting full color optical image to binary using the default color threshold function. Noise was removed by 2-3 pixel erosion steps, followed by an equal number of pixel dilation steps. After denoising, a radial profile function was run, centered at the sample initiation point, to provide a 2-D plot of feature intensity as a function of radial distance. Peak picking afforded the radii at maximum feature intensity, which was then used to calculate the feature wavelength.

5.8 Notes and References

5.8.1 Notes

This is a collaborative effort with multiple contributors from the Moore, Sottos, and Geubelle groups. E.M.L performed the experiments, characterized all materials, and authored the text. Elizabeth Feinberg performed image analysis, collected UV-Vis data, and contributed to ideation. Yuan Gao and Julie Hemmer performed the numerical simulations. Julie Hemmer also contributed to the development of the power ratio. Bhaskar Soman collected and analyzed the WAXS data. Suzanne Peterson performed the bleaching experiments. Leon Dean and Qiong Wu developed FROMP of cyclooctadiene which was utilized in this work.

5.8.2 References

1. Aizenberg, J.; Weaver, J. C.; Thanawala, M. S.; Sundar, V. C.; Morse, D. E.; Fratzl, P. Skeleton of *Euplectella* Sp.: Structural Hierarchy from the Nanoscale to the Microscale. *Science* **2005**, 209, 275-278.
2. Deville, S.; Saiz, E.; Nalla, R. K.; Tomsia, A. P. Freezing as a Path to Build Complex Composites. *Science* **2006**, 311, 515-518.
3. Huang, W.; Restrepo, D.; Jung, J.-Y.; Su, F. Y.; Liu, Z.; Ritchie, R. O.; McKittrick, J.; Zavattieri, P.; Kisailus, D. Multiscale Toughening Mechanisms in Biological Materials and Bioinspired Designs. *Adv. Mater.* **2019**, 31, 1901561.
4. Prevost, A.; Scheibert, J.; Debrégeas, G. Effect of Fingerprints Orientation on Skin Vibrations during Tactile Exploration of Textured Surfaces. *Commun. Integr. Biol.* **2014**, 2, 422424.
5. Turing, A. M. The Chemical Basis of Morphogenesis. *Philos. Trans. R. Soc. London, Ser. B* **1952**, 237, 37-72.
6. Gierer, A.; Meinhardt, H. A Theory of Biological Pattern Formation. *Kybernetik* **1972**, 12, 30-39.
7. Meinhardt, H. *Models of Biological Pattern Formation*; Academic Press: London, 1982.
8. Murray, J. D. *Mathematical Biology, I: An Introduction* Third Edition; Springer: New York, 2002.
9. Richardson, J. J.; Cui, J.; Björnmalm, M.; Braunger, J. A.; Ejima, H.; Caruso, F. Innovation in Layer-by-Layer Assembly. *Chem. Rev.* **2016**, 116, 14828-14867.
10. Thompson, L. F. in *An Introduction to Lithography* (eds. Thompson, L. F.; Willson, C. G.; Bowden, M. J.) American Chemical Society: Washington D. C., 1983; pp. 1-13.
11. Scrimin, P.; Prins, L. J. Sensing through Signal Amplification. *Chem. Soc. Rev.* **2011**, 40, 4488-4505.
12. Bissette, A. J.; Fletcher, S. P. Mechanisms of Autocatalysis. *Angew. Chem. Int. Ed.* **2013**, 52, 12800-12826.
13. Zaikin, A. N.; Zhabotinsky, A. M. Concentration Wave Propagation in Two-Dimensional Liquid-Phase Self-Oscillating System. *Nature* **1970**, 225, 535-537.
14. Noszticzius, Z.; Horsthemke, W.; McCormic, W. D.; Swinney, H. L.; Tam, W. Y. Sustained Chemical Waves in an Annular Gel Reactor: A Chemical Pinwheel. *Nature* **1987**, 329, 619-620.
15. Ouyang, Q.; Swinney, H. L. Transition from a Uniform State to Hexagonal and Striped Turing Patterns. *Nature* **1991**, 352, 610-612.
16. Lengyel, I.; Epstein, I. R. A Chemical Approach to Designing Turing Patterns in Reaction-Diffusion Systems. *Proc. Natl. Acad. Sci. USA* **1992**, 89, 3977-3979.
17. Campbell, C. J.; Fialkowski, M.; Klajn, R.; Bensemann, I. T.; Grzybowski, B. A. Color Micro- and Nanopatterning with Counter-Propagating Reaction–Diffusion Fronts. *Adv. Mater.* **2004**, 16, 1912-1917.
18. Campbell, C. J.; Klajn, R.; Fialkowski, M.; Grzybowski, B. A. One-Step Multilevel Microfabrication by Reaction−Diffusion. *Langmuir* **2005**, 21, 418-423.
19. Tan, Z.; Chen, S.; Peng, X.; Zhang, L.; Gao, C. Polyamide Membranes with Nanoscale Turing Structures for Water Purification. *Science* **2018**, 360, 518-521.
20. Karig, D.; Martini, K. M.; Lu, T.; DeLateur, N. A.; Goldenfeld, N.; Weiss, R. Stochastic Turing Patterns in a Synthetic Bacterial Population. *Proc. Natl. Acad. Sci. USA* **2018**, 115, 6572-6577.
21. Mariani, A.; Fiori, S.; Chekanov, Y.; Pojman, J. A. Frontal Ring-Opening Metathesis Polymerization of Dicyclopentadiene. *Macromolecules* **2001**, 34, 6539-6541.
22. Pojman, J. A. in *Polymer Science: A Comprehensive Reference* Vol. 4 (eds. Matyjaszewski, K. & Möller, M.) Elsevier: Amsterdam, 2012; pp. 957-980.
23. Goli, E.; Robertson, I. D.; Geubelle, P. H.; Moore, J. S. Frontal Polymerization of Dicyclopentadiene: A Numerical Study. *J. Phys. Chem. B* **2018**, 122, 4583-4591.
24. Robertson, I. D.; Yourdkhani, M; Centellas, P. J.; En Aw, J.; Ivanoff, D. G.; Goli, E.; Lloyd, E. M.; Dean, L. M.; Sottos, N. R.; Geubelle, P. H.; Moore, J. S.; White, S. R. Rapid Energy-Efficient Manufacturing of Polymers and Composites via Frontal Polymerization. *Nature* **2018**, 557, 223-227.
25. Pojman, J. A.; Ilyashenko, V. M.; Khan, A. M. Spin Mode Instabilities in Propagating Fronts of Polymerization. *Phys. D Nonlinear Phenom.* **1995**, 84, 260-268.
26. Masere, J.; Pojman, J. A. Free Radical-Scavenging Dyes as Indicators of Frontal Polymerization Dynamics. *J. Chem. Soc., Faraday Trans.* **1998**, 94, 919-922.
27. Masere, J.; Stewart, F.; Meehan, T.; Pojman, J. A. Period-Doubling Behavior in Frontal Polymerization of Multifunctional Acrylates. *Chaos* **1999**, 9, 315-322.
28. Ilyashenko, V. M.; Pojman, J. A. Single-Head Spin Modes in Frontal Polymerization. *Chaos* **1998**,8 , 285-289.
29. Pojman, J. A.; Masere, J.; Petretto, E.; Rustici, M.; Do-Sung, H.; Kim, M. S.; Volpert, V. The Effect of Reactor Geometry on Frontal Polymerization Spin Modes. *Chaos* **2002**, 12, 56–65.

30. Huh, D. S.; Kim, H. S. Bistability of Propagating Front with Spin-mode in a Frontal Polymerization of Trimethylopropane Triacrylate. *Polym. Int.* **2003**, 52, 1900-1904.
31. Inamdar, S. R.; Pujari, N. S.; Karimi, I. A.; Ponrathnam, S.; Tayal, R. K.; Kulkarni, B. D. Spinning Wave Motion in Frontal Polymerization. *Chem. Eng. Sci.* **2007**, 62, 1448-1455.
32. Aldushin, A. P.; Malomed, B. A.; Zeldovich, Ya. B. Phenomenological Theory of Spin Combustion. *Combust. Flame* **2003**, 42, 1-6.
33. Strunin, D. V.; Strunina, A. G.; Rumanov, E. N.; Merzhanov, A. G. Chaotic Reaction Waves with Fast Diffusion of Activator. *Phys. Lett. A* **1994**, 192, 361-363.
34. Solovyov, S. E.; Ilyashenko, V. M.; Pojman, J. A. Numerical Modeling of Self-Propagating Polymerization Fronts: The Role of Kinetics on Front Stability. *Chaos* **1997**, 7, 331-340.
35. Pojman, J. A. Mathematical Modeling of Frontal Polymerization. *Math. Model. Nat. Phenom.* **2019**, 14, 604.
36. Smith, W. T.; Greenbaum, S.; Rutledge, G. P. Correlation of Critical Temperatures with Thermal Expansion Coefficients of Organic Liquids. *J. Phys. Chem.* **1954**, 58, 443-447.
37. Chung, Y.-C.; Su, Y. O. Effects of Phenyl- and Methyl-Substituents on *p*-Phenylenediamine, an Electrochemical and Spectral Study. *J. Chin. Chem. Soc.* **2009**, 56, 493-503.
38. Michaelis, L.; Schubert, M. P.; Granick, S. The Free Radicals of the Type of Wurster's Salts. *J. Am. Chem. Soc.* **1939**, 61, 1981–1992.
39. Dean, L. M.; Wu, Q.; Alshangiti, O.; Moore, J. S.; Sottos, N. R. Rapid Synthesis of Elastomers and Thermosets with Tunable Thermomechanical Properties. *ACS Macro Lett.* **2020**, 9, 819-824.
40. Cornell, S. W.; Koenig, J. L. The Raman Spectra of Polybutadiene Rubbers. *Macromolecules* **1969**, 2, 540-545.
41. Read, K. I. Experimental Investigation of Turbulent Mixing by Rayleigh-Taylor Instability. *Phys. D Nonlinear Phenom.* **1984**, 12, 45-58.
42. Gaston, D.; Newman, C.; Hansen, G.; Lebrun-Grandié, D. MOOSE: A Parallel Computational Framework for Coupled Systems of Nonlinear Equations. *Nucl. Eng. Des.* **2009**, 239, 1768-1778.
43. Pernice, M.;Walker, H. F. NITSOL: A Newton Iterative Solver for Nonlinear Systems. *SIAM J. Sci. Comput.* **1998**, 19, 302-318.
44. Knoll, D. A.; Keyes, D. E. Jacobian-Free Newton-Krylov Methods: A Survey of Approaches and Applications. *J. Comput. Phys.* **2004**, 193, 357-397.
45. Oliver, W. C.; Pharr, G. M. An Improved Technique for Determining the Hardness and Elastic Modulus Using Load and Displacement Sensing Indentation Experiments. *J. Mater. Res.* **1992**, 7, 1564-158.

Chapter 6: Materials Concepts for Developmental Manufacturing

6.1 Introduction

Prized for their light weight, ease of manufacture, and vast array of properties, polymeric materials have become integral to virtually every aspect of daily life. Global plastic production has exceeded 300 million metric tons annually and is expected to double by 2050[1]. Reaching these massive production volumes has required highly deterministic – or carefully planned, engineered, and orchestrated – manufacturing approaches which ensure a high fidelity of form. Unfortunately, traditional manufacturing approaches such as injection molding, thermoforming, and autoclave curing are limited in the complexity of structures, patterns, and functions that can be generated. Additional post-processing steps such as lithography[2] or high-temperature vascularization[3,4] are required to impart patterns or complex structures, severely limiting access to multifunctional materials. Subsequently, the majority of polymeric materials remain passive and monofunctional throughout their lifecycles.

Natural systems, in great contrast, evolved sophisticated mechanisms to impart organisms with multiscale structures and patterns, enabling a variety of multifunctional processes. These functional attributes are possible even though pattern formation is a non-deterministic process which relies on spontaneous symmetry breaking events[5–9]. Impressively, these non-deterministic processes achieve both high fidelity of form and function throughout nature. Further, living systems come to be via biochemical processes that take place in the wild, rather than a pristine manufacturing plant. Living organisms, therefore, interact with and adapt to their environments as they grow and develop. While significant progress has been made in understanding the fundamental processes governing biological development and enabling functional responses in nature, the translation of these findings to synthetic systems is still in its infancy.

Recent efforts by the Autonomous Materials Systems (AMS) group at the University of Illinois at Urbana-Champaign and our colleagues in the field of multifunctionality materials have centered on mimicking biological structures[10,11] and functions such as healing[12–14] and remodeling[15–18] in synthetic materials. Once fully passive, polymeric materials are beginning to interact with and respond productively to environmental cues. However, manufacturing techniques remain highly deterministic, and synthetic systems still fail to fully encompass the complexity and sophistication of biological materials. Drawing inspiration from nature, we believe non-deterministic manufacturing approaches are needed for the design of next generation materials. In this chapter, we provide a brief overview of several key processes in biological morphogenesis. We then draw an analogy between morphogenesis and an emerging materials manufacturing technique, frontal polymerization. Finally, we discuss several principles that we believe are integral to the sustainable design of synthetic materials.

6.2 Biological Development

During biological development, a number of evolutionary processes give rise to form and function in natural systems. The most transformational of all mechanisms in biological development is morphogenesis. Through morphogenesis, periodic patterns and complex, multifunctional structures emerge from initial states of high symmetry during a series of symmetry-breaking events[6]. Remarkably, the patterns and structures that emerge through morphogenesis are replicated throughout nature with unprecedented fidelity. No two patterns or structures are perfectly identical, but they have the same characteristic features and perform the same functions within the species. Aside from the rare defects or mutations, we are born with four limbs, ten digits, ten toes, two eyes, two ears, one mouth, and one nose. We may not have identical fingerprints, but the ridges and furrows are arranged into characteristic whorls, loops, and arches[19].

The ridges and furrows also serve the same purpose: improving our tactile sensing[20]. Within developmental biology, a number of theoretical models for morphogenesis have been proposed, including Turing's reaction-diffusion model, Wolpert's concept of positional information, and mechanochemical coupling. For a more comprehensive discussion of theories of developmental biology, we direct the readers to several texts by J. D. Murray, P. K. Maini, and H. G. Othmer.[21–24]

In 1952, Alan Turing postulated that patterns emerge through precise feedback-driven promotion and inhibition of chemical species, known as morphogens[6,25]. These morphogens, one an activator and the other an inhibitor, react chemically and diffuse throughout space. Given the random nature of diffusion, systems experience fluctuations and deviations from their initially symmetric states.[25] In a system at equilibrium, these chance fluctuations average out and symmetry is retained. However, for a system far from thermodynamic equilibrium, small perturbations are amplified, and spontaneous symmetry breaking events can occur[25]. Turing provided the analogy of a marble on a dome[6] to describe how small fluctuations can drive a break from equilibrium. With this concept of coupled reaction and diffusion and relatively simple mathematics, Turing predicted patterns, by hand, that bore a striking resemblance to natural patterns[6].

Turing's revolutionary ideas were met with skepticism and largely ignored for nearly two decades[26]. From the physicist's perspective, diffusion was believed to disrupt patterns[26] by favoring disorder and maximizing entropy. Further, the dependence of Turing's model on random fluctuations and sensitivity to initial conditions did not agree with the robust nature of biological pattern formation[27]. However, twenty years after Turing's seminal paper, Grier and Meinhardt created a resurgence of interest in reaction-diffusion processes by formalizing the conditions required to generate patterns from the coupled reaction and diffusion of chemical species[7]. First,

the two chemical species, as Turing suggested, are an activator and an inhibitor. Second, the activator must display autocatalysis such that chance fluctuations are amplified, and the inhibitor suppresses the autocatalysis of the activator. Finally, Grier and Meinhardt recognized that the diffusion of the two species must be different. To prevent uncontrolled growth of the activator, the inhibitor must diffuse faster than the activator. Turing's idea of coupled reaction and diffusion, with over thirteen thousand citations, has formed the framework of a number of theoretical and experimental depictions of biological pattern formation.[5,8,28–38]

Where Turing sought to answer the question of how patterns could emerge from symmetry, Lewis Wolpert sought to address how asymmetries could drive the emergence of more complicated patterns[26], publishing his ideas on positional information in 1969[39]. Wolpert proposed that when subject to a spatial gradient in morphogen concentration, cells would sense the local concentration and differentiate into whatever fate was appropriate.[39–42] One of the key aspects of Wolpert's hypothesis was the presence of this interpretation step.[26,43] In Turing's model, cell fate was tied directly to morphogen concentration. However, with positional information, a continuous concentration gradient could generate any arbitrary pattern, and importantly, concentration gradients could be interpreted differently among species[26]. Additionally, the concept of positional information is independent of size. The solution to Wolpert's French flag problem remains the same regardless of the size of the flag, and a French flag can be obtained regardless of the number or size of parts that are removed.[39] Wolpert recognized that this feature corresponded well with experimental observations in biological systems: the original pattern of an organism can be regenerated even if small or large pieces are removed.[39] Positional information was further supported when *Drosophila* segments were found to develop in response to gradients in gap genes.[44,45]

Together, Turing's reaction-diffusion processes and Wolpert's positional information represent the foundational chemical concepts which govern biological morphogenesis. However, it is also believed that mechanochemical coupling is critical to creating form and function.[46–51] The Murray–Oster continuum mechanochemical model is rooted in experimental observations that cells generate large traction forces during motion which are capable of deforming elastic substrates and creating anisotropies in the local environment[52–54]. Fibroblasts were found to align collagen fibers within the extracellular matrix (ECM) into linear tracts that were more than two orders of magnitude greater than the cell diameter.[54] The alignment of collagen fibers locally increases the density of cell adhesion sites, leading to directed cellular motion by haptotaxis and contact guidance.[46,49] Murray and coworkers observed that the interactions between cells and the ECM provides a feedback loop for cellular motion: mobile cells significantly deform the ECM and deformations in the ECM direct motion.[46] The coupling of traction forces and cell motility leads to the spontaneous patterning of cellular aggregates.[46,47] The mechanochemical model for morphogenesis has successfully been applied to number of systems including the formation of vasculature from mesenchymal stem cells[51], condensation of chondrocytes[46], and hydra regeneration[55].

While each of these processes were discovered and described independently, it is believed that biological development relies on their synergy. Reaction-diffusion processes are strongly dependent on initial and boundary conditions and are unlikely to produce the same patterns and structures in different environments. However, mechanical signaling provides an additional level of feedback[55], ensuring the correct final form is reached in a plethora of conditions. Braun and Keren elegantly stated that the closed loop dynamics of mechanical and biochemical signaling

ensures fidelity of form and function across multiple length scales.[55] Similarly, developmental manufacturing of synthetic materials will require a multifaceted approach.

6.3 Frontal Polymerization: A Molecular Toolkit for Developmental Manufacturing

Since Leo Hendrik Baekeland first introduced Bakelite in the early 1900s[56,57], the global plastics industry has grown exponentially as polymeric materials are easily manufactured at large scale and low cost. However, in all cases, synthetic polymer manufacturing is deterministic. Precision-machined molds and dies, accurately controlled ovens and autoclaves, and teams of engineers and technicians are all required to produce components with a wide range of shapes and sizes. In contrast, natural systems rely on non-deterministic symmetry breaking events to bring about form and function. Impressively, non-deterministic manufacturing imparts biological materials with levels of complexity which are well beyond the scope of the molds, ovens, and printers of synthetic manufacturing. We believe that there must be a paradigm shift in manufacturing to create the next generation of polymeric materials, and frontal polymerization provides one promising route.

Our interests and explorations into frontal polymerization (FP) began in the early 1990s when our late colleague and dear friend, Scott R. White, pioneered a novel fiber-reinforced composite manufacturing technique[58–60]. S.R.W sought to reduce the manufacture time and potential for deleterious thermal spikes in thick composite lamina by stacking prepreg layers as a reaction front propagated through the thickness. To avoid thermal spikes and ensure adequate interlaminar strength, a delicate balance between the material feed rate and the reaction rate was required. If the reaction front propagated faster than the material was supplied, the matrix would cure prior to the formation of any interlaminar bonding. Conversely, if the material supply rate greatly exceeded the reaction rate, the advantages of the simultaneous process were negated. S.R.W. may not have

recognized it at the time, but this pioneering work set the stage for a revolution in the AMS group. Nearly thirty years after his initial publication, the focus of our group has shifted heavily towards frontal polymerization.

The concept of frontal polymerization was first explored in the 1970s[61–67] and has a rich history of innovation rooted in combustion theory and dynamics. During frontal polymerization, a thermally latent catalyst is activated by a localized thermal stimulus to participate in a highly exothermic reaction.[68] The heat of polymerization drives further reaction, generating a propagating wave of polymerization which rapidly converts monomer into polymer. Work led by Prof. John Pojman at Louisiana State University has greatly advanced the field providing a number of fundamental studies into the dynamics of FP[69–75] and expanding the library of FP resins[76–85]. His excitement for the application of FP in art displays and household construction[86] serves as a continuous inspiration to explore the limits and applications of science.

Nearly 20 years after S.R.W. published his paper on simultaneous lay-up and epoxy curing, our interest in frontal polymerization was renewed when Ian Robertson and coworkers utilized an acrylate resin to create a microfluidic endoskeleton which would globally stiffen in response to a local thermal stimulus[87]. Soon after, the Illinois team began pursuing FP to manufacture fiber-reinforced composites and was strongly encouraged to investigate more mechanically robust FP systems for composite manufacturing, such as the frontal ring-opening metathesis polymerization (FROMP) of dicyclopentadiene (DCPD) pioneered by Alberto Mariani and coworkers[80,88,89]. To translate FROMP of DCPD to composite manufacturing, the latency, which was limited from seconds to several minutes, required significant improvement. The discovery of alkyl phosphite inhibitors for FROMP of DCPD[90] provided unprecedented pot lives and culminated in the energy-efficient manufacture of high-performance composite materials[91]. Alkyl phosphites have become

a staple in all AMS laboratories at Illinois and have enabled us to creatively explore the bounds of polymer manufacturing.

While we were finishing our initial work with composite manufacturing through FP, S.R.W., Jeffrey S. Moore, Nancy R. Sottos, and Philippe H. Geubelle, were also inspired by the similarities of the reaction-transport systems in FP and Turing's model for morphogenesis. They approached E.M.L. with an annotated copy of Philip Ball's commentary[25] on Alan Turing's 1952 paper 'The Chemical Basis of Morphogenesis'[6] and asked E.M.L. if he was up for the challenge of generating a formal analogy and finding routes to patterns with FP. It is important to note that we are not the first to recognize the analogy between propagating reaction waves and Turing's model for morphogenesis. A. G. Merzhanov and coworkers recognized this analogy[92] at a time when S.R.W. was first exploring FP.

$$(1)\ \frac{\partial T}{\partial t} = g(\alpha, T) + \lambda \nabla^2 T$$

$$(2)\ \frac{\partial c_J}{\partial t} = f(c_A, c_I) + D_J \nabla^2 c_J$$

A close look at the reaction-transport equations of FP (Equation 1) and Turing's framework for morphogenesis (Equation 2) demonstrates the parallel between the two. The temperature of the polymerization front, T, is analogous to the morphogen concentration, c_J, and the monomer thermal diffusivity, λ, mirrors morphogen mass diffusivity, D_J. Further, a key feature of both systems is the presence of autocatalysis.[6,68] During morphogenesis, autocatalysis enables the local growth of an activator following a small perturbation from the initial state, rather than a return to equilibrium. Similarly, in FP, the transport of heat from the highly exothermic polymerization reaction drives the propagation of the polymerization front following a small energetic input. Where these two systems differ is the final output. The reaction-diffusion processes of

morphogenesis generate well defined and periodic patterns. Conversely, under typical experimental conditions, polymerization fronts propagate uniformly, transforming liquid monomer into solid polymer with a uniform temperature profile.

When studying gasless combustion, Merzhanov and coworkers observed that propagation instabilities, which lead to undulations in propagation velocity, developed under conditions of rapid thermal diffusion.[92] This observation highlighted a fundamental difference between the reaction-diffusion processes of biological patterning and frontal propagation. A key aspect of Turing's model was rapid diffusion of the inhibitor to prevent uncontrolled growth of the activator. During combustion, instabilities require rapid diffusion of heat, the activator. Our theoretical studies of FP in high-volume fraction carbon fiber-reinforced composites, led by P.H.G., supported Merzhanov's claims.[93] A reduction in reaction rate and an increase in thermal transport due to the high thermal conductivity of carbon fibers led to propagation instabilities. Similar instabilities have been reported widely throughout combustion and FP literature and are known to generate large undulations in reaction temperature.[68–70,72,73,92,94–99] We believe that controlling and harnessing these undulations in reaction temperature are the key to patterning during frontal polymerization.

In 1938, Yakov Zeldovich introduced a dimensionless parameter to describe the boundary between modes of frontal propagation.[95,100] Widely known as the Zeldovich number, it considers the role of the effective activation energy and the initial and maximum temperature of the reagents. John Pojman and coworkers have demonstrated facile methods of controlling propagation dynamics in acrylate FP resins by tuning the Zeldovich number.[73] By changing the effective activation energy, they observed a period doubling behavior of the spin modes encountered during unstable FP. E.M.L. and coworkers recently proposed a new dimensionless parameter, φ (Equation 3), which compares the power densities of both reaction (P_R) and thermal transport (P_T), as a

phenomenological descriptor of front stability (ρ, H_r, A, E_A, R, $\bar{T}$, κ, and L_θ respectively represent the resin density, enthalpy of reaction, pre-exponential factor, universal gas constant, average of the initial and maximum temperature, thermal conductivity, and the width of the thermal front). We observed that, when the power density of thermal transport was slightly greater than that of the reaction, propagation instabilities appeared, and the thermal profiles were readily controlled by tuning the ratio of reaction and transport powers. This work again highlighted the importance of rapid transport of the activator in creating patterns with FP.

$$(3)\ \varphi = \frac{P_R}{P_T} = \frac{\rho H_r A e^{-E_A/R\bar{T}}}{\kappa \frac{\bar{T}}{{L_\theta}^2}}$$

The large ΔT generated by propagation instabilities provides opportunities to apply thermally responsive chemistries to permanently pattern the material properties in response to the thermal history. John Pojman utilized free radical scavenging dyes which changed color in response to the increased decomposition of peroxide initiators at locations of high front temperature.[71] E.M.L. and coworkers employed thermochromic radical cations which locally bleached when polymerization temperatures exceed 250 °C. They also explored the temperature dependent *cis*/*trans* isomerization of poly(cyclooctadiene) to locally control the crystallinity and stiffness of frontally polymerized materials. We envision that the vast body of work in stimuli-responsive materials will find a home in FP, provided that the transformation kinetics are compatible with the polymerization kinetics during unstable propagation. We direct the readers to several review articles in the areas of self-assembly[101–105], liquid crystals[106–109], and transient materials[110–113] for additional inspiration.

The similarities between biological development and frontal polymerization are not limited to Turing's theory of morphogenesis. Alberto Mariani and coworkers has elegantly shown that the pre-patterning of resins enables the synthesis of functionally graded materials[114], providing an

analogy to Wolpert's theory of positional information. We anticipate that this analogy would be easily extended by also pre-patterning the thermal profile of an FP resin to amplify propagation instabilities and create larger differences in material properties. Further, we recently incorporated mechanical feedback into frontal polymerization. By applying an oscillatory load to an elastic gel undergoing FP, highly regular and readily tuned surface undulations were created. Combining each of these FP concepts – propagation instabilities, pre-patterning, and mechanochemical coupling – provides a wholistic approach to developmental manufacturing and will enable the spontaneous growth of functional materials.

6.4 Incorporating Lifecycle Control

As we embark on the journey towards the next generation of synthetic materials, we must consider the entire lifecycle of a material, not just the intended application. Polymeric materials were manufactured at million-ton scales and integrated into nearly every aspect of our everyday lives with excitement over their ease of manufacture and little thought applied to their inevitable end of life. Subsequently, plastic pollution is now a global crisis that will plague society for years to come. To reduce our footprint and work towards a better tomorrow, we require materials which mitigate their global impact at each stage: birth, life, and death. Currently, synthetic material design is inferior to natural systems in all three stages.

As discussed in previous sections, the deterministic manufacturing of polymeric materials fails to recapitulate the complexity and multifunctional nature of biological tissues. We believe that pursuing non-deterministic manufacturing approaches, such as frontal polymerization, will not only provide access to patterns, structures, and functions which are beyond our current technologies but also reduce the energetic requirements of polymeric materials. Further, improving

the multifunctionality of synthetic materials will greatly improve the next two stages of the material lifecycle.

Unlike biological systems, synthetic materials fail to interact with and adapt to their environments, resulting in a steady accumulation of damage and decay throughout their lifetime. Biological tissues achieve both interactions and adaptations through a process known as signal transduction, which transforms an extracellular or intracellular event into a series of reactions. Eventually this reaction cascade generates a global change in the organism. Environmental stimuli range from anywhere from concentration gradients to applied mechanical force. Over the past several decades there have been tremendous advancements in recapitulating signal transduction in synthetic materials. S.R.W., J.S.M., N.R.S., and P.H.G. entered into this field in the early 2000s, creating a microcapsule design for self-healing materials[12]. Since this early contribution, we have developed new healing strategies[3,4,14,115–118] and damage sensing materials[119–122] and discovered new uses for vasculature in synthetic materials[123–125]. Several of our comrades in the field of multifunctional materials have joined us in creating additional healing chemistries[13,126,127], novel mechanophores[128–132], and strategies toward adaptation[16–18,133,134]. For a more detailed discussion of multifunctional materials, we direct the readers to a recent review article[135] by Jason Patrick and coworkers.

Work in self-healing and adaptive materials has truly pushed the boundaries of materials design into unprecedented areas. However, the emphasis has been placed on extending the material lifespan and not on engineering for the inevitable death of a material. This brings a very important question to the surface: will a material that heals or adapts be more difficult to dispose of when it is removed from service? In light of this question, we argue that continued efforts to improve the longevity of materials, without considering the end of life for a material, are irresponsible.

For synthetic materials, the end of life is reached after a single use or after many years of service, during which time damage steadily accumulates. However, removal from service is not really the end of a polymeric material. The high strength covalent networks of polymeric materials ensure continued existence, albeit as waste, for an unknown amount of time. Some materials, such as thermoplastics, are recycled and reborn as new products, but, in most cases, that history of damage remains. Recycled plastics are continuously downgraded with each successive cycle until they can no longer fulfill a purpose and are discarded.[136] For natural systems, the end of life is very different. Everything from a single macromolecule to an entire organism is broken down into building blocks for future use. This perfectly circular economy is the true embodiment of sustainability.

Over the past decade there has been an amazing outpouring of research into polymers with end-of-life strategies.[137] We and several of our colleagues, such as Prof. Scott Philipps at Boise State University and Prof. Elizabeth Gillies at Western University, have emphasized research into low ceiling temperature (T_c) polymers as a route to a circular plastics economy.[138–141] Low T_c polymers, which readily revert to monomer under relatively mild conditions, emulate nature's modular design for macromolecules and enable closed-loop utilization of resources. Others, such as Prof. Jeremiah Johnson at the Massachusetts Institute of Technology, have explored the installation of cleavable units into commodity thermoset networks through copolymerization.[142] When random copolymers are formed, the cleavable comonomers can be incorporated at relatively low loadings with no impact on the manufacturing methods and minimal changes to the final mechanical properties. Prof. Johnson's work with cleavable cyclic olefins has encouraged us to explore recyclable and multifunctional monomers for frontal polymerization.

6.5 Systems-Level Engineering

Our recent emphasis on degradable materials has inspired us to begin thinking about systems-level engineering. In our recent demonstrations and those of our comrades, material disintegration hinges on surface degradation or swelling in a degradation solution. While this is acceptable for small, laboratory-scale pieces, how would you efficiently degrade the thermoset matrix of a 50 m long wind turbine blade? It would not be practical to drop the blade into container filled with the required degradation reagents. Instead, degradation should be triggered from internal vasculature, which brings about another major question. How do we create a vascular network which ensures complete deconstruction prior to the failure of the channels? The answer lies in digital design and optimization.

Digital design and optimization have already found a home in the AMS labs. P.H.G. led efforts to optimize cooling performance and blockage tolerance in vascular polymers and composites.[123,124] Computational predictions were coupled to high-speed fabrication techniques to validate the designs. Similar approaches have been successfully implemented by Prof. Martin Dunn's group at the University of Colorado Denver.[143] They sought to disrupt the traditional computer-aided design and computer-aided manufacturing workflows common in product development by creating a new design workflow for additive manufacturing. His workflow was formed on three pillars: design autonomation based on multiscale topology optimization, computational geometry algorithms with spatially-variable multimaterial microstructures, and digital fabrication through voxel-based additive manufacturing. With this new workflow, Dunn's group was able to create highly optimized structures for a variety of applications, all with unmatched performance. We believe that digital design and optimization approaches like these examples will be instrumental in developmental manufacturing. Through these workflows,

material performance will be optimized for a variety of functions, ranging anywhere from healing to programmed degradation.

6.6 Conclusions

This chapter has highlighted the similarities between biological morphogenesis, specifically Turing's reaction-diffusion model, and frontal polymerization. FP represents an avenue toward developmental manufacturing that is akin to the non-deterministic developmental processes which ensure high fidelity of form and function in natural systems. The nearly fifty years of research into FP has generated a large library of FP resins, making this concept applicable to a wide range of product sectors. We also provide our perspective on two key concepts, life cycle control and systems-level engineering, which must be considered as we embark on the journey towards next generation polymeric materials. We hope that the ideas and insights in this chapter will inspire researchers in multifunctional materials to continue pursuing nature's great example of development.

6.7 References

1. Lebreton, L.; Andrady, A. Future Scenarios of Global Plastic Waste Generation and Disposal. *Palgrave Commun.* **2019**, 5, 6.
2. Thompson, L. F. in *An Introduction to Lithography* (eds. Thompson, L. F.; Willson, C. G.; Bowden, M. J.) American Chemical Society: Washington D. C., 1983; pp. 1-13.
3. Esser-Kahn, A. P.; Thakre, P. R.; Dong, H.; Patrick, J. F.; Vlasko-Vlasov, V. K.; Sottos, N. R.; Moore, J. S.; White, S. R. Three-Dimensional Microvascular Fiber-Reinforced Composites. *Adv. Mater.* **2011**, 23, 3654-3658.
4. Gergely, R. C. R.; Pety, S. J.; Krull, B. P.; Patrick, J. F.; Doan, T. Q.; Coppola, A. M.; Thakre, P. R.; Sottos, N. R.; Moore, J. S.; White, S. R. Multidimensional Vascularized Polymers Using Degradable Sacrificial Templates. *Adv. Func. Mater.* **2014**, 25, 1043-1052.
5. Ishihara, K.; Tanaka, E. M. Spontaneous Symmetry Breaking and Pattern Formation of Organoids. *Curr. Opin. Syst. Biol.* **2018**, 1, 14.
6. Turing, A. M. The Chemical Basis of Morphogenesis. *Philos. Trans. R. Soc., B* **1952**, 237, 37-72.
7. Grier, A.; Meinhardt, H. A Theory of Biological Pattern Formation. *Kybernetik* **1972**, 12, 30-39.
8. Meinhardt, H. *Models of Biological Pattern Formation*; Academic Press: London, 1982.
9. Meinhardt, H.; Gierer A. Pattern Formation by Local Self-Activation and Lateral Inhibition. *BioEssays* **2000**, 22, 753-760.
10. Deville, S.; Saiz, E.; Nalla, R. K.; Tomsia, A. P. Freezing as a Path to Build Complex Composites. *Science* **2006**, 311, 515-518.
11. Yang, Y.; Li, X.; Zheng, X.; Chen, Z.; Zhou, Q.; Chen, Y.; 3D-Printed Biomimetic Super-Hydrophobic Structure for Microdroplet Manipulation and Oil/Water Separation. *Adv. Mater.* **2018**, 30, 1704912.
12. White, S. R.; Sottos, N. R.; Geubelle, P. H.; Moore, J. S.; Kessler, M. R.; Sriram, S. R.; Brown, E. N.; Viswanathan, S. Autonomic Healing of Polymer Composites. *Nature* **2001**, 409, 794-797.

13. Chen, X.; Dam, M. A.; Ono, K.; Mal, A.; Shen, H.; Nutt, S. R.; Sheran, K.; Wudl, F. A Thermally Re-Mendable Cross-Linked Polymeric Material. *Science* **2002**, 295, 1698-1702.
14. White, S. R.; Moore, J. S.; Sottos, N. R.; Krull, B. P.; Cruz, W. A. S.; Gergely, R. C. R. Restoration of Large Damage Volumes in Polymers. *Science* **2014**, 344, 620-623.
15. Diesendruck, C. E.; Peterson, G. I.; Kulik, H. J.; Kaitz, J. A.; Mar, B. D.; May, P. A.; White, S. R.; Martínez, T. J.; Boydston, A. J.; Moore, J. S. Mechanically Triggered Heterolytic Unzipping of a Low-Ceiling-Temperature Polymer. *Nat. Chem.* **2014**, 6, 623-628.
16. Brubaker, K. S.; Kleiman, M.; Hernandez, L.; Bhattacharjee, A.; Esser-Kahn, A. P. Structural Remodeling of Polymeric Material via Diffusion Controlled Polymerization and Chain Scission. *Chem. Mater.* **2018**, 30, 8126-8133.
17. Kleiman, M.; Brubaker, K. S.; Nguyen, D. T.; Esser-Kahn, A. P. Bio-Inspired Morphogenesis Using Microvascular Networks and Reaction–Diffusion. *Chem. Mater.* **2015**, 27, 4871-4876.
18. Wang, J.; Piskun, I.; Craig, S. L. Mechanochemical Strengthening of a Multi-Mechanophore Benzocyclobutene Polymer. *ACS Macro Lett.* **2015**, 4, 834-837.
19. Kücken, M.; Newell, A. C. Fingerprint Formation. *J. Theor. Biol.* **2005**, 235, 71-83.
20. Prevost, A.; Scheibert, J.; Debrégeas, G. Effect of Fingerprints Orientation on Skin Vibrations during Tactile Exploration of Textured Surfaces. *Commun. Integr. Biol.* **2014**, 2, 422-424.
21. Murray, J. D. *Mathematical Biology, I: An Introduction* Third Edition; Springer: New York, 2002.
22. Maini, P. K.; Othmer, H. G. *Mathematical Models for Biological Pattern Formation*; Springer: New York, 2001.
23. Othmer, H. G.; Maini, P. K.; Murray, J. D. *Experimental and Theoretical Advances in Biological Pattern Formation*; Springer: New York, 1993.
24. Murray, J. D. *Mathematical Biology, II: Spatial Models and Biomedical Applications*; Springer: New York, 2006.
25. Ball, P. Forging Patterns and Making Waves from Biology to Geology: A Commentary on Turing (1952) "The Chemical Basis of Morphogenesis." *Philos. Trans. R. Soc., B* **2015**, 370, 20140218.
26. Green, J. B. A.; Sharpe, J. Positional Information and Reaction-Diffusion: Two Big Ideas in Developmental Biology Combine. *Development* **2015**, 142, 1203-1211
27. Bard, J.; Lauder, I. How Well Does Turing's Theory of Morphogenesis Work? *J. Theor. Biol.* **1974**, 34, 501-531.
28. Segel, L. A.; Jackson, J. L. Dissipative Structure: An Explanation and an Ecological Example. *J. Theor. Biol.* **1972**, 37, 545-559.
29. Kondo, S.; Asai, R. A Reaction-Diffusion Wave on the Skin of the Marine Angelfish Pomacanthus. *Nature* **1995**, 376, 765-768.
30. Scoones, J. C.; Hiscock, T. W. A Dot-Stripe Turing Model of Joint Patterning in the Tetrapod Limb. *Development* **2020**, 147, dev183699.
31. Raspopovic, J.; Marcon, L.; Russo, L.; Sharpe, J. Digit Patterning Is Controlled by a Bmp-Sox9-Wnt Turing Network Modulated by Morphogen Gradients. *Science* **2014**, 345, 566-570.
32. Sheth, R.; Marcon, L.; Bastida, M. F.; Junco, M.; Quintana, L.; Dahn, R.; Kmita, M.; Sharpe, J.; Ros, M. A. Hox Genes Regulate Digit Patterning by Controlling the Wavelength of a Turing-Type Mechanism. *Science* **2012**, 338, 1476-1480.
33. Economou, A. D.; Ohazama, A.; Porntaveetus, T.; Sharpe, P. T.; Kondo, S.; Basson, M. A.; Gritli-Linde, A.; Cobourne, M. T.; Green, J. B. A. Periodic Stripe Formation by a Turing Mechanism Operating at Growth Zones in the Mammalian Palate. *Nat. Genet.* **2012**, 44, 348-351.
34. Kondo, S.; Miura, T. Reaction-Diffusion Model as a Framework for Understanding Biological Pattern Formation. *Science* **2010**, 329, 1616-1620.
35. Painter, K. J.; Maini, P. K.; Othmer, H. G. Stripe Formation in Juvenile Pomacanthus Explained by a Generalized Turing Mechanism with Chemotaxis. *Proc. Natl. Acad. Sci. USA* **1999**, 96, 5549-5554.
36. Onimaru, K.; Marcon, L.; Musy, M.; Tanaka, M.; Sharpe, J. The Fin-to-Limb Transition as the Re-Organization of a Turing Pattern. *Nat. Commun*. **2016**, 7, 11582.
37. Newman, S. A. The Turing Mechanism in Vertebrate Limb Patterning. *Nat. Rev. Mol. Cell Biol.* **2007**, 8, 1.
38. Hata, S.; Nakao, H.; Mikhailov, A. S. Dispersal-Induced Destabilization of Metapopulations and Oscillatory Turing Patterns in Ecological Networks. *Sci. Rep.* **2014**, 4, 3585.
39. Wolpert, L Positional Information and the Spatial Pattern of Cellular Differentiation. *J. Theor. Biol.* **1969**, 25, 1-47.
40. Wolpert, L. in *Current Topics in Developmental Biology* Vol. 6 (eds. Moscona, A. A. & Monroy, A.) Academic Press: London, 1971.
41. Wolpert, L. Positional Information Revisited. *Development* **1989**, 107, 3-12.
42. Wolpert, L. Positional Information and Patterning Revisited. *J. Theor. Biol.* **2011**, 269, 359-365.

43. Sharpe, J. Wolpert's French Flag: What's the Problem? *Development* **2019**, 146, dev185967.
44. Akam, M. The Molecular Basis for Metameric Pattern in the Drosophila Embryo. *Development* **1987**, 101, 1-22.
45. Akam, M. Making Stripes Inelegantly. *Nature* **1989**, 341, 282-283.
46. Murray, J. D.; Oster, G. F.; Harris, A. K. A Mechanical Model for Mesenchymal Morphogenesis. *J. Math. Biol.* **1983**, 17, 125-129.
47. Murray, J. D.; Oster, G. F. Cell Traction Models for Generating Pattern and Form in Morphogenesis. *J. Math. Biol.* **1984**, 19, 265-279.
48. Murray, J. D.; Oster, G. F. Generation of Biological Pattern and Form. *Math. Med. Biol.* **1984**, 1, 51-75.
49. Oster, G. F.; Murray, J. D.; Harris, A. K. Mechanical Aspects of Mesenchymal Morphogenesis. *J. Embryol. Exp. Morphol.* **1983**, 78, 83-125.
50. Murray, J. D.; Maini, P. K.; Tranquillo, R. T. Mechanochemical Models for Generating Biological Pattern and Form in Development. *Phys. Rep.* **1988**, 171, 59-84.
51. Murray, J. D. On the Mechanochemical Theory of Biological Pattern Formation with Application to Vasculogenesis. *C. R. Biol.* **2003**, 326, 239-252.
52. Harris, A.; Wild, P.; Stopak, D. Silicone Rubber Substrata: A New Wrinkle in the Study of Cell Locomotion. *Science* **1980**, 208, 177-179.
53. Harris, A. K.; Stopak, D.; Wild, P. Fibroblast Traction as a Mechanism for Collagen Morphogenesis. *Nature* **1981**, 290, 249-251.
54. Stopak, D.; Harris, A. K. Connective Tissue Morphogenesis by Fibroblast Traction I. Tissue Culture Observations. *Dev. Biol.* **1982**, *90* (2), 383-398.
55. Braun, E.; Keren, K. Hydra Regeneration: Closing the Loop with Mechanical Processes in Morphogenesis. *BioEssays* **2018**, 40, 1700204.
56. Baekeland, L. H. Bakelite, a Condensation Product of Phenols and Formaldehyde, and Its Uses. *J. Franklin Inst.* **1910**, 169, 55-60.
57. Baekeland, L. H. The Synthesis, Constitution, and Uses of Bakelite. *J. Ind. Eng. Chem.* **1909**, 1, 149-161.
58. White, S. R.; Kim, C. A Simultaneous Lay-Up and in situ Cure Process for Thick Composites. *J. Reinf. Plast. Compos.* **1993**, 12, 520-535.
59. Kim, C.; Teng, H.; Tucker, C. L.; White, S. R. The Continuous Cuing Process for Thermoset Polymer Composites. Part 1: Modeling and Demonstration. *J. Compos. Mater.* **1995**, 29, 1222-1253.
60. Kim, C.; White, S. R. The Continuous Curing Process for Thermoset Polymer Composites. Part 2: Experimental Results for a Graphite/Epoxy Laminate. *J. Compos. Mater.* **1996**, 30, 627-647.
61. Chechilo, N. M.; Khvilivitsky, R. Y.; Enikolopyan, N. S. The Phenomenon of Propagation of the Polymerization Reaction. *Dokl. Akad. Nauk SSR* **1972**, 204, 1180-1181.
62. Khanukaev, B. B.; Kozhushner, M. A.; Enikolopyan, N. S. Theory of Polymerization-Front Propagation. *Combust. Explos. Shock Waves* **1974**, 10, 562–568.
63. Chechilo, N. M.; Enikolopyan, N. S. Structure of the Polymerization Wave Front and Propagation Mechanism of the Polymerization Reaction. *Dokl. Phys. Chem.* **1974**, 214,174-176.
64. Chechilo, N. M.; Enikolopyan, N. S. Effect of the Concentration and Nature of Initiators on the Propagation Process in Polymerization. *Dokl. Phys. Chem.* **1975**, 221, 392-394.
65. Aleksanyan, G. G.; Arutyunyan, Kh. A.; Bodneva, V. L.; Davtyan, S. P.; Prut, E. V.; Rozenberg, B. A.; Shkadinskii, K. G.; Yenikolopyan, N. S. Some Rules Governing the Extension of the Front of Radical Polymerization of Vinyl Monomers. *Polym. Sci. USSR* **1975**, 17, 1052-1059.
66. Chechilo, N. M.; Enikolopyan, N. S. Effect of Pressure and Initial Temperature on the Reaction Mixture during Propagation of a Polymerization Reaction. *Dokl. Phys. Chem.* **1976**, 230, 840-843.
67. Arutiunian, K. A.; Davtyan, S. P.; Rozenberg, B. A.; Enikolopyan, N. S. Curing of Epoxy Resins of Bis-Phenol A by Amines under Conditions of Reaction Front Propagation. *Dokl. Akad. Nauk SSSR* **1975**, 223,657-660.
68. Pojman, J. A. in *Polymer Science: A Comprehensive Reference* Vol. 4 (eds. Matyjaszewski, K. & Möller, M.) Elsevier: Amsterdam, 2012; pp. 957-980.
69. Pojman, J. A.; Ilyashenko, V. M.; Khan, A. M. Spin Mode Instabilities in Propagating Fronts of Polymerization. *Phys. D* **2003**, 84, 260-268.
70. Volpert, Vit. A.; Volpert, Vl. A.; Pojman, J. A.; Solovyov, S. E. Hydrodynamic Stability of a Polymerization Front. *Eur. J. Appl. Math.* **2001**, *7* (3), 303-320.
71. Masere, J.; Pojman, J. A. Free Radical-Scavenging Dyes as Indicators of Frontal Polymerization Dynamics. *J. Chem Soc., Faraday Trans.* **1998**, 94, 919-922.
72. Ilyashenko, V. M.; Pojman, J. A. Single-Head Spin Modes in Frontal Polymerization. *Chaos* **1998**, 8, 285-289.

73. Masere, J.; Stewart, F.; Meehan, T.; Pojman, J. A. Period-Doubling Behavior in Frontal Polymerization of Multifunctional Acrylates. *Chaos* **1999**, 9, 315-322.
74. Pojman, J. A.; Masere, J.; Petretto, E.; Rustici, M.; Huh, D.-S.; Kim, M. S.; Volpert, V. The Effect of Reactor Geometry on Frontal Polymerization Spin Modes. *Chaos* **2002**, 12, 56-65.
75. Bansal, K.; Pojman, J. A.; Webster, D.; Quadir, M. Frontal Polymerization of a Thin Film on a Wood Substrate. *ACS Macro Lett.* **2020**, 9, 169-173.
76. Pojman, J. A. Traveling Fronts of Methacrylic Acid Polymerization. *J. Am. Chem. Soc.* **1991**, 113, 6284-6286.
77. Nagy, I. P.; Sike, L.; Pojman, J. A. Thermochromic Composites and Propagating Polymerization Fronts. *Adv. Mater.* **1995**, 7, 1038-1040.
78. Nagy, I. P.; Sike, L.; Pojman, J. A. Thermochromic Composite Prepared via a Propagating Polymerization Front. *J. Am. Chem. Soc.* **1995**, 117, 3611-3612.
79. Chekanov, Y.; Arrington, D.; Brust, G.; Pojman, J. A. Frontal Curing of Epoxy Resins: Comparison of Mechanical and Thermal Properties to Batch-Cured Materials. *J. Appl. Polym. Sci.* **1997**, 66, 1209-1216.
80. Mariani, A.; Fiori, S.; Chekanov, Y.; Pojman, J. A. Frontal Ring-Opening Metathesis Polymerization of Dicyclopentadiene. *Macromolecules* **2001**, 34, 6539-6541.
81. Nason, C.; Roper, T.; Hoyle, C.; Pojman, J. A. UV-Induced Frontal Polymerization of Multifunctional (Meth)Acrylates. *Macromolecules* **2005**, 38, 5506-5512.
82. Chen, S.; Hu, T.; Tian, Y.; Chen, L.; Pojman, J. A. Facile Synthesis of Poly(Hydroxyethyl Acrylate) by Frontal Free-Radical Polymerization. *J. Polym. Sci., Part A: Polym. Chem.* **2007**, 45, 873-881.
83. Scognamillo, S.; Bounds, C.; Luger, M.; Mariani, A.; Pojman, J. A. Frontal Cationic Curing of Epoxy Resins. *J. Polym. Sci., Part A: Polym. Chem.* **2010**, 48, 2000-2005.
84. Fazende, K. F.; Phachansitthi, M.; Mota-Morales, J. D.; Pojman, J. A. Frontal Polymerization of Deep Eutectic Solvents Composed of Acrylic and Methacrylic Acids. *J. Polym. Sci., Part A: Polym. Chem.* **2017**, 55, 4046-4050.
85. Gary, D. P.; Bynum, S.; Thompson, B. D.; Groce, B. R.; Sagona, A.; Hoffman, I. M.; Morejon-Garcia, C.; Weber, C.; Pojman, J. A. Thermal Transport and Chemical Effects of Fillers on Free-radical Frontal Polymerization. *J. Polym. Sci.* **2020**, 58, 2267-2277.
86. Holt, T.; Fazende, K.; Jee, E.; Wu, Q.; Pojman, J. A. Cure-on-Demand Wood Adhesive Based on the Frontal Polymerization of Acrylates. *J. Appl. Polym. Sci.* **2016**, 133, 44064.
87. Robertson, I. D.; Lopez Hernandez, H.; White, S. R.; Moore, J. S. Rapid Stiffening of a Microfluidic Endoskeleton via Frontal Polymerization. *ACS Appl. Mater. Inter.* **2014**, 6, 18469-18474.
88. Ruiu, A.; Sanna, D.; Alzari, V.; Nuvoli, D.; Mariani, A. Advances in the Frontal Ring Opening Metathesis Polymerization of Dicyclopentadiene. *J. Polym. Sci., Part A: Polym. Chem.* **2014**, 52, 2776-2780.
89. Alzari, V.; Nuvoli, D.; Sanna, D.; Ruiu, A.; Mariani, A. Effect of Limonene on the Frontal Ring Opening Metathesis Polymerization of Dicyclopentadiene. *J. Polym. Sci., Part A: Polym. Chem.* **2015**, 54, 63-68.
90. Robertson, I. D.; Dean, L. M.; Rudebusch, G. E.; Sottos, N. R.; White, S. R.; Moore, J. S. Alkyl Phosphite Inhibitors for Frontal Ring-Opening Metathesis Polymerization Greatly Increase Pot Life. *ACS Macro Lett.* **2017**, 6, 609-612.
91. Robertson, I. D.; Yourdkhani, M.; Centellas, P. J.; Aw, J. E.; Ivanoff, D. G.; Goli, E.; Lloyd, E. M.; Dean, L. M.; Sottos, N. R.; Geubelle, P. H.; Moore, J. S.; White, S. R. Rapid Energy-Efficient Manufacturing of Polymers and Composites via Frontal Polymerization. *Nature* **2018**, 557, 223-227.
92. Strunin, D. V.; Strunina, A. G.; Rumanov, E. N.; Merzhanov, A. G. Chaotic Reaction Waves with Fast Diffusion of Activator. *Phys. Lett. A* **1994**, 192, 361-363.
93. Goli, E.; Peterson, S. R.; Geubelle, P. H. Instabilities Driven by Frontal Polymerization in Thermosetting Polymers and Composites. *Composites, Part B* **2020**, 199, 108306.
94. Shkiro, V. M.; Nersisyan, G. A. Structure of Fluctuations Occurring in the Burning of Tantalum-Carbon Mixtures. *Combust. Explos. Shock Waves* **1978**, 14, 121-122.
95. Aldushin, A. P.; Malomed, B. A.; Zeldovich, Ya. B. Phenomenological Theory of Spin Combustion. *Combust. Flame* **2003**, 42, 1-6.
96. Bayliss, A.; Matkowsky, B. J. Two Routes to Chaos in Condensed Phase Combustion. *SIAM J. Appl. Math.* **1990**, 50, 437-459.
97. Novozhilov, B. V. Non-Linear SHS Phenomena: Experiment, Theory, Numerical Modeling. *Pure Appl. Chem.* **1992**, 64, 955-964.
98. Margolis, S. B. The Asymptotic Theory of Gasless Combustion Synthesis. *Metall. Trans.* **1992**, 23, 15-22.
99. Solovyov, S. E.; Ilyashenko, V. M.; Pojman, J. A. Numerical Modeling of Self-Propagating Polymerization Fronts: The Role of Kinetics on Front Stability. *Chaos* **1997**, 7, 331-340.

100. Zeldowitsch, J. B.; Frank-Kamenetzki, D. A. *Acta. Physicochim. URSS* **1938**, 9, 341-350.
101. Whitesides, G. M.; Grzybowski, B. Self-Assembly at All Scales. *Science* **2002**, 295, 2418-2421.
102. Lehn, J.-M. From Supramolecular Chemistry towards Constitutional Dynamic Chemistry and Adaptive Chemistry. *Chem. Soc. Rev.* **2006**, 36, 151-160.
103. Lehn, J.-M. Towards Complex Matter: Supramolecular Chemistry and Self-Organization*. *Eur. Rev.* **2009**, 17, 263-280.
104. Webber, M. J. Engineering Responsive Supramolecular Biomaterials: Toward Smart Therapeutics. *Bioeng. Transl. Med.* **2016**, 1, 252-266.
105. Shigemitsu, H.; Hamachi, I. Design Strategies of Stimuli-Responsive Supramolecular Hydrogels Relying on Structural Analyses and Cell-Mimicking Approaches. *Acc. Chem. Res.* **2017**, 50, 740-750.
106. Xie, P.; Zhang, R. Liquid Crystal Elastomers, Networks and Gels: Advanced Smart Materials. *J. Mater. Chem.* **2005**, 15, 2529-2550.
107. Fleischmann, E.; Zentel, R. Liquid-Crystalline Ordering as a Concept in Materials Science: From Semiconductors to Stimuli-Responsive Devices. *Angew. Chem., Int. Ed.* **2013**, 52, 8810-8827.
108. Bukusoglu, E.; Pantoja, M. B.; Mushenheim, P. C.; Wang, X.; Abbott, N. L. Design of Responsive and Active (Soft) Materials Using Liquid Crystals. *Annu. Rev. Chem. Biomol. Eng.* **2014**, 7, 1-34.
109. Boothby, J. M.; Kim, H.; Ware, T. H. Shape Changes in Chemoresponsive Liquid Crystal Elastomers. *Sens. Actuators, B* **2017**, 240, 511-518.
110. Kaitz, J. A.; Lee, O. P.; Moore, J. S. Depolymerizable Polymers: Preparation, Applications, and Future Outlook. *MRS Commun.* **2015**, 5, 191-204.
111. Fu, K.; Wang, Z.; Dai, J.; Carter, M.; Hu, L. Transient Electronics: Materials and Devices. *Chem. Mater.* **2016**, 28, 3527-3539.
112. Wang, F.; Diesendruck, C. E. Polyphthalaldehyde: Synthesis, Derivatives, and Applications. *Macromol. Rapid Commun.* **2017**, 39, 1700519.
113. Yardley, R. E.; Kenaree, A. R.; Gillies, E. R. Triggering Depolymerization: Progress and Opportunities for Self-Immolative Polymers. *Macromolecules* **2019**, 52, 6342-6360.
114. Nuvoli, D.; Alzari, V.; Pojman, J. A.; Sanna, V.; Ruiu, A.; Sanna, D.; Malucelli, G.; Mariani, A. Synthesis and Characterization of Functionally Gradient Materials Obtained by Frontal Polymerization. *ACS Appl. Mater. Inter.* **2015**, 7, 3600-3606.
115. Patrick, J. F.; Hart, K. R.; Krull, B. P.; Diesendruck, C. E.; Moore, J. S.; White, S. R.; Sottos, N. R. Continuous Self-Healing Life Cycle in Vascularized Structural Composites. *Adv. Mater.* **2014**, 26, 4302-4308.
116. Krull, B. P.; Gergely, R. C. R.; Cruz, W. A. S.; Fedonina, Y. I.; Patrick, J. F.; White, S. R.; Sottos, N. R. Strategies for Volumetric Recovery of Large Scale Damage in Polymers. *Adv. Funct. Mater.* **2016**, 26, 4561-4569.
117. Dean, L. M.; Krull, B. P.; Li, K. R.; Fedonina, Y. I.; White, S. R.; Sottos, N. R. Enhanced Mixing of Microvascular Self-Healing Reagents Using Segmented Gas–Liquid Flow. *ACS Appl. Mater. Inter.* **2018**, 10, 32659-32667.
118. Toohey, K. S.; Sottos, N. R.; Lewis, J. A.; Moore, J. S.; White, S. R. Self-Healing Materials with Microvascular Networks. *Nat. Mater.* **2007**, 6, 581-585.
119. Robb, M. J.; Li, W.; Gergely, R. C. R.; Matthews, C. C.; White, S. R.; Sottos, N. R.; Moore, J. S. A Robust Damage-Reporting Strategy for Polymeric Materials Enabled by Aggregation-Induced Emission. *ACS Cent. Sci.* **2016**, 2, 598-603.
120. Davis, D. A.; Hamilton, A.; Yang, J.; Cremar, L. D.; Gough, D. V.; Potisek, S. L.; Ong, M. T.; Braun, P. V.; Martínez, T. J.; White, S. R.; Moore, J. S.; Sottos, N. R. Force-Induced Activation of Covalent Bonds in Mechanoresponsive Polymeric Materials. *Nature* **2009**, 459, 68-72.
121. Kim, T. A.; Lamuta, C.; Kim, H.; Leal, C.; Sottos, N. R. Interfacial Force-Focusing Effect in Mechanophore-Linked Nanocomposites. *Adv. Sci.* **2020**, 7, 1903464.
122. Sulkanen, A. R.; Sung, J.; Robb, M. J.; Moore, J. S.; Sottos, N. R.; Liu, G. Spatially Selective and Density-Controlled Activation of Interfacial Mechanophores. *J. Am. Chem. Soc.* **2019**, 141, 4080-4085.
123. Pety, S. J.; Tan, M. H. Y.; Najafi, A. R.; Barnett, P. R.; Geubelle, P. H.; White, S. R. Carbon Fiber Composites with 2D Microvascular Networks for Battery Cooling. *Int. J. Heat Mass Transfer* **2017**, 115, 513-522.
124. Pety, S. J.; Tan, M. H. Y.; Najafi, A. R.; Gendusa, A. C.; Barnett, P. R.; Geubelle, P. H.; White, S. R. Design of Redundant Microvascular Cooling Networks for Blockage Tolerance. *Appl. Therm. Eng.* **2018**, 131, 965-976.
125. Pety, S. J.; Aw, J. E.; Gendusa, A. C.; Barnett, P. R.; Calvert, Q. A.; Sottos, N. R.; White, S. R. Effect of Microchannels on the Crashworthiness of Fiber-Reinforced Composites. *Compos. Struct.* **2018**, 184, 428-436.
126. Ying, H.; Zhang, Y.; Cheng, J. Dynamic Urea Bond for the Design of Reversible and Self-Healing Polymers. *Nat. Commun.* **2014**, 5, 3218.

127. Zavada, S. R.; McHardy, N. R.; Gordon, K. L.; Scott, T. F. Rapid, Puncture-Initiated Healing via Oxygen-Mediated Polymerization. *ACS Macro Lett.* **2015**, 4, 819-824.
128. Piermattei, A.; Karthikeyan, S.; Sijbesma, R. P. Activating Catalysts with Mechanical Force. *Nat. Chem.* **2009**, 1, 133-137.
129. Jakobs, R. T. M.; Sijbesma, R. P. Mechanical Activation of a Latent Olefin Metathesis Catalyst and Persistence of Its Active Species in ROMP. *Organometallics* **2012**, 31, 2476-2481.
130. Lin, Y.; Kouznetsova, T. B.; Craig, S. L. A Latent Mechanoacid for Time-Stamped Mechanochromism and Chemical Signaling in Polymeric Materials. *J. Am. Chem. Soc.* **2019**, 142, 99-103.
131. Bowser, B. H.; Ho, C.-H.; Craig, S. L. High Mechanophore Content, Stress-Relieving Copolymers Synthesized via RAFT Polymerization. *Macromolecules* **2019**, 52, 9032-9038.
132. Lin, Y.; Kouznetsova, T. B.; Craig, S. L. Mechanically Gated Degradable Polymers. *J. Am. Chem. Soc.* **2020**, 142, 2105-2109.
133. Kean, Z. S.; Craig, S. L. Mechanochemical Remodeling of Synthetic Polymers. *Polymer* **2012**, 53, 1035-1048.
134. Ramirez, A. L. B.; Kean, Z. S.; Orlicki, J. A.; Champhekar, M.; Elsakr, S. M.; Krause, W. E.; Craig, S. L. Mechanochemical Strengthening of a Synthetic Polymer in Response to Typically Destructive Shear Forces. *Nat. Chem.* **2013**, 5, 757-761.
135. Patrick, J. F.; Robb, M. J.; Sottos, N. R.; Moore, J. S.; White, S. R. Polymers with Autonomous Life-Cycle Control. *Nature* **2016**, 540, 363-370.
136. Hong, M.; Chen, E. Y.-X. Chemically Recyclable Polymers: A Circular Economy Approach to Sustainability. *Green Chem.* **2017**, 19, 3692-3706.
137. Schneiderman, D. K.; Hillmyer, M. A. 50th Anniversary Perspective: There Is a Great Future in Sustainable Polymers. *Macromolecules* **2017**, 50, 3733-3749.
138. Baker, M. S.; Kim, H.; Olah, M. G.; Lewis, G. G.; Phillips, S. T. Depolymerizable Poly(Benzyl Ether)-Based Materials for Selective Room Temperature Recycling. *Green Chem.* **2015**, 17, 4541-4545.
139. Fan, B.; Trant, J. F.; Yardley, R. E.; Pickering, A. J.; Lagugné-Labarthet, F.; Gillies, E. R. Photocontrolled Degradation of Stimuli-Responsive Poly(Ethyl Glyoxylate): Differentiating Features and Traceless Ambient Depolymerization. *Macromolecules* **2016**, 49, 7196-7203.
140. Zhu, J.-B.; Watson, E. M.; Tang, J.; Chen, E. Y.-X. A Synthetic Polymer System with Repeatable Chemical Recyclability. *Science* **2018**, 360, 398-403.
141. Lloyd, E. M.; Hernandez, H. L.; Feinberg, A. M.; Yourdkhani, M.; Zen, E. K.; Mejia, E. B.; Sottos, N. R.; Moore, J. S.; White, S. R. Fully Recyclable Metastable Polymers and Composites. *Chem. Mater.* **2018**, 31, 398-406.
142. Shieh, P.; Zhang, W.; Husted, K. E. L.; Kristufek, S. L.; Xiong, B.; Lundberg, D. J.; Lem, J.; Veysset, D.; Sun, Y.; Nelson, K. A.; Plata, D. L.; Johnson, J. A. Cleavable Comonomers Enable Degradable, Recyclable Thermoset Plastics. *Nature* **2020**, 583, 542-547.
143. Boddeti, N.; Ding, Z.; Kaijima, S.; Maute, K.; Dunn, M. L. Simultaneous Digital Design and Additive Manufacture of Structures and Materials. *Sci. Rep.* **2018**, 8, 15560.